# Grasping Contact Analysis of Viscoelastic Materials for Design and Development of an Endoscopic Tactile Sensor

Ali Bonakdar

A Ph.D. Thesis

in

Department

of

Mechanical and Industrial Engineering

Presented in Partial Fulfillment of the Requirements
for the Degree of Doctor of Philosophy at
Concordia University
Montreal, Quebec, Canada

September 2007

*Your file Votre référence*
*ISBN: 978-0-494-31147-9*
*Our file Notre référence*
*ISBN: 978-0-494-31147-9*

# ABSTRACT

Grasping Contact Analysis of Viscoelastic Materials for Design and Development of an Endoscopic Tactile Sensor

Ali Bonakdar, Ph.D.
Concordia University, 2007

In this study, analytical and Finite Element Method (FEM) are employed to determine the contact pressure on the surface of a tissue being grasped by an endoscopic grasper, in Minimally Invasive Surgery (MIS). Normally, an endoscopic grasper has corrugated teeth in order to maintain a firm grip on slippery tissues. Because it is very important to avoid damage while grasping and manipulating tissue during endoscopic surgery, it is essential to determine the exact contact pressure on the surface of the tissue. To this end, a comprehensive closed form analysis is undertaken followed by the finite element and experimental analyses of the grasping contact pressure on viscoelastic materials which have similar properties as that of biological tissues. The behavior of a grasper with wedge and semi-cylindrical teeth is examined when pressed into a linear viscoelastic material. Initially, a single tooth penetrating into a solid is studied and then is extended to the multi teeth grasper. The elastic wedge and semi-cylinder penetration is the basis of the closed form analysis. Also the effects of time are included in the equations by considering the corresponding integral operator from viscoelastic stress-stain relations. In addition, a finite element analysis is carried out. Finally, the experimental results will be presented to validate both analytical and FEM analysis. The results of this study provide a closed form expression for grasping contact pressure, force and contact area along with the variations of stress in tissue obtained through FEM

analysis. The variation of contact pressure and the rate of growth of the contact area with time are also presented. In order to determine the properties of the biological tissues during MIS, we present the design, analysis, fabrication and assembly of four-tooth annular micro-fabricated tactile sensors incorporated to the upper and lower jaws of an endoscopic surgical grasper tool. Two viscoelastic models, namely, Kelvin-Voight and Kelvin are employed for tissue characterization. The relationship between the force ratio, compliance and the equivalent viscous damping of the tissue are studied. The designed sensor uses a Polyvinylidene Fluoride (PVDF) film as its sensing element. The sensor consists of arrays of rigid and compliant elements which are mounted on the tip of an endoscopic surgical grasper tool. The relative force between adjacent parts of the contact object is used to measure the viscoelastic properties.

**This Thesis is dedicated to**
**my mother Pary and my**
**father Mahmoud.**

# ACKNOWLEDGMENT

This thesis is the result of three and half years of work whereby I have been encouraged and supported by many people. It is the most pleasant task where I have the opportunity to express my gratitude to all of them.

I am deeply indebted to my supervisors, Professor Rama Bhat and Professor Javad Dargahi for their invaluable support. I would never have finished my Ph.D. without their common sense, knowledge and perceptiveness.

I would like to thank my best friends at Concordia, Marjan Molavi and Nagarajan Narayanan Babu and Reza Ramezanifard for their assistance and friendly support during the length of my research work. Also, I acknowledge with thanks to Dr. Packirisamy for letting me to use his lab facilitates for micromachining of my devices.

Finally, I would like to express my sincerest gratitude to my parents and my family for their continuous motivation and emotional support. I would like to thank my mother Mrs. Barazandehpay and my father Mr. Bonakdar who taught me the value of patience, hard work and commitment without which I could not have completed my Ph.D. In addition, I am thankful to my sister Nafiseh, my brother Hamed, my brother-in-law Ramin, Mr. Majid Rafieyan and Mrs. Nezhat Babanoury for their kind help during my education.

# TABLE OF CONTENTS

# List of Figures

# List of Tables

# List of Symbols and Acronyms

| | |
|---|---|
| $°C$ | Degree Celsius |
| *1-D, 2-D* | One Dimensional, Two Dimensional |
| $a$ | Contact area |
| $a$ | Pyroelectric coefficient |
| $A_a$ | Area of the rigid cylinder |
| $A_b$ | Area of the compliant cylinder |
| $a_{ij}$ | Second rank thermal coefficient tensor |
| $B(t)$ | relaxation modulus in dilatation |
| $C$ | Capacitance |
| $C, c$ | Viscous Damping coefficient |
| $D$ | Del operator |
| $D$ | Diameter of rigid cylinder |
| $d_{31}, d_{32}, d_{33}$ | Piezoelectric conistant |
| $D_i$ | First rank electrical displacement |
| $d_{ijk}$ | Third rank piezoelectric coefficient tensor |
| $e$ | Piezoelectric Coefficient ($C/m^2$) |
| $E$ | Young's modulus |
| $E_1$ | Young's modulus of grasped object |
| $E_2$ | Young's modulus of compliant cylinder |
| $E_k$ | First rank electric field tensor |

| | |
|---|---|
| $F_1$ | Force carried by the rigid cylinder |
| $F_2$ | Force carried by the compliant cylinder |
| $G$ | Shear Modulus |
| $g$ | Spring modulus |
| $h$ | Contact depth |
| $Hz$ | Hertz |
| $Ib$ | Pound force |
| $I_\varepsilon$ | First invariant of strain |
| $I_\sigma$ | First invariant of stress |
| $J_1$ | Creep Compliance |
| $J_2$ | Volumetric compliance |
| $k_{ij}$ | Second rank permitivity tensor |
| $M$ | Moment |
| $MPa$ | Mega Pascal |
| $n$ | Normal to surface |
| $N$ | Newton |
| $P$ | Pressure |
| $p(x)$ | Normal pressure |
| $pC$ | Picocoulumb |
| $p_i$ | First rank pyroelectric coefficients tensor |
| $Q$ | Charge |
| $q(x)$ | Tangential traction |

| | |
|---|---|
| $R$ | Reaction force |
| $R_i$ | Radius of rigid Cylinder |
| $R$ | Radius of semi-cylinder tooth |
| $R_1$ | Inner Radius of Compliant cylinder |
| $R_2$ | Outer Radius of Compliant Cylinder |
| $s_0$ | step change of deviator stress |
| $s_{ij}$ | deviator stress |
| $S_{ijkl}$ | Forth rank elasticity tensor |
| $t$ | time |
| $T$ | Time constant |
| $T_1$ | Thickness of sensed object |
| $T_2$ | Rigid and compliant cylinder height |
| $u_x$, $u_z$ | Displacements |
| $V$ | Voltage |
| $V_1$ | Voltage output of PVDF under Inner cylinder |
| $V_2$ | Voltage output of PVDF under the outer cylinder |
| $W$ | Width of Piezoelectric crystal |
| $X1$ | Deformation of sensed object over rigid cylinder |
| $X2$ | Deformation of the compliant cylinder |
| $Y$ | Yield stress |
| $\alpha$ | Semi-angle of wedge |

| | |
|---|---|
| $\delta$ | Contact depth |
| $\delta_{ij}$ | Kronecker delta |
| $\Delta T$ | Zero rank temperature tensor |
| $\varepsilon_{ij}$ | Second rank strain tensor |
| $\eta$ | Dashpot of viscosity |
| $\mu$ | Coefficient of friction |
| $\mu m$ | Micrometer |
| $v$ | Poisson ratio |
| $\sigma$ | Normal stress |
| $\sigma_{ij}$ | Second rank stress tensor |
| $\tau$ | Shear stress |
| $\Omega$ | Ohms |

## Acronyms

| | |
|---|---|
| *A/D* | Analog to digital |
| DAQ | Data Acquisition system |
| DC | Direct current |
| FEA | Finite Element Analysis |
| FEM | Finite Element Method |
| LSR | Liquid Silicon Rubber |
| Mat | Material |
| MIS | Minimally Invasive Surgery |
| PR | Photo resist |

| | |
|---|---|
| PR | Photoresist |
| PVDF | Polyvinylidene Fluoride |
| PVDF-1 | PVDF under the inner rigid cylinder |
| PVDF-2 | PVDF under the outer soft cylinder |
| PZT | Lead Zirconate Titanate |
| SNR | Signal to noise ratio |
| UV | Ultraviolet |
| VLSI | Very Large Scale Integration |

# CHAPTER 1

# INTRODUCTION AND LITERATURE REVIEW

## 1.1 Minimally Invasive Surgery

Minimally Invasive Surgery (MIS) was being introduced just about two decades ago. Today, MIS has become a standard surgical procedure, often replacing traditional open surgery and has also become widely accepted. Traditional surgery requires an incision large enough for the surgeon to see directly and place his or her fingers and instruments directly into the target-operating site. Most often, the damage done to skin, muscle, connective tissue, and bone to reach the region of interest causes much greater injury than the curative procedure itself. This results in more pain to the patient, longer recovery time, and complications due to surgical ordeal. The current trend is accelerating toward minimally invasive surgery (MIS), in which unnecessary trauma encountered in conventional surgical procedures is limited by reducing the size of incisions to less than about 1 cm or by using catheters or endoscopes threaded through vessels, the gastrointestinal tract, or other tubular structures. In addition, they can even extend the surgeon's capability over great distances, via telesurgery.

The first endoscopic cholecystectomy which is the removal of the gallbladder was done in 1987. Gallbladder removals, along with appendectomies, are some of the most common minimally invasive procedures in practice. Keyhole approaches are used in a number of other fields - cardiology, urology, neurology, gastroenterology, gynecology, and many others. Companies have designed a number of endoscopes for specific operations. For instance, the laparoscope is used for surgery in the abdomen. Heart

surgeons use a thoracoscope to examine the interior of the chest. MIS is a procedure carried out by a surgeon through a small incision using specialized equipment and endoscopic or other visualization techniques not requiring direct access. Traditional surgical approaches have utilized incisions designed to provide the maximum exposure of the operative site. Minimally invasive surgical approaches, on the other hand, utilize small incisions through which cameras and instruments are passed to accomplish the operation from within a body cavity. The minimally invasive surgical approach offers several advantages over traditional open surgery. Surgeons skilled in minimally invasive surgical procedures regularly perform them as rapidly as they perform the equivalent open operations. Furthermore, the reduction in inpatient hospital stays results in an actual lowering of total hospital costs for many of the procedures performed. Figure (1-1) shows some of the minimally invasive surgical tools being currently used.

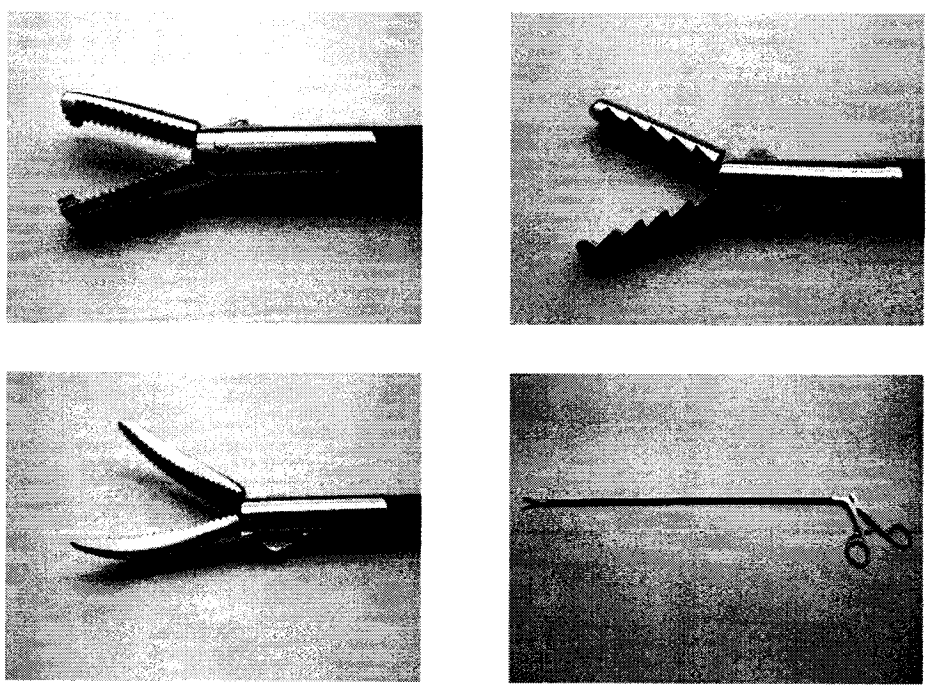

**Figure (1-1).** Typical endoscopic tools and graspers.

Some of the benefits of minimally invasive surgery are enumerated below [1].

### 1.1.1 Minimally Invasive Surgery Benefits

- Smaller incisions
- Less blood loss, less scarring
- Less pain during recovery
- Some procedures performed on an outpatient basis
- Faster recovery
- Quicker return to everyday activities
- Shorter hospital stays
- Better clinical outcomes
- Fewer complications due to infection

With MIS we can do the following operations, which are done by traditional surgeries, in a more effective way.

### 1.1.2 More Surgical Options

- General Surgery
- Gynecology
- Orthopedics
- Plastic Surgery
- Thoracic Surgery
- Vascular Surgery

However, from the surgeon's point of view, MIS suffers from the lack of tactile feedback that the surgeons use to apprise the tissues, bones, organs within the operative site. As a result of this loss, the surgeons will not be able to manipulate important properties of the tissues such as the softness, compliance, surface texture at the site of the operation.

Surgeons have been known to insert their fingers through the access openings during MIS simply to perform direct tactile exploration [2]. Dario's short but far-sighted review [3] cites medical applications in which the softness of tissues is detected through palpation. However, Bicchi et al [4], have discussed capacitive tactile sensors and associated tactile display units for use in MIS. By correlating force against deformation, the system was able to identity five objects of different elastic properties.

A series of designs for endoscopic and laparoscopic tools are discussed by Cohn et al., [5], who propose incorporating their tactile telepresence apparatus. An interesting idea raised here is the possibility of using the capacitive tactile sensor, not to measure applied force, but to detect the varying dielectric permittivity of different tissues. Cohn et al suggest that water, fat, blood vessels, and cancerous tissue might all be discriminated by this means.

An experiment with a sensor for laparoscopic attachment has been described by Fischer et al [5]. A 64 point sensor of area 1 $cm^2$ was connected to a fingertip vibrotaction display.

Dizaji et al [7] developed a new cancer diagnostic approach by ultrasonic imaging of tissues in which the tissue elasticity is measured and compared with the elasticity of normal tissues. The results of displacement estimation of normal and abnormal breast tissues under external stress are calculated using image registration technique. The work

estimates not only the translation, but also the rotation and scaling parameters. The Young's modulus calculated from displacement values was then used to identify tissue characterization. The work also showed that the above-mentioned procedure can successfully detect abnormal tissues. The latest developments in minimally invasive haptic surgery were described by Picinbono et al [8], where a new deformable model based on non-linear elasticity and the finite element method was proposed. This model is valid for large displacements, invariant with respect to rotations and therefore improves the realism of the deformations and solves the problems related to the shortcomings of linear elasticity that is valid only for small displacements. Problems associated with anisotropic behavior and volume variations were also addressed. Gladilin et al [9] used a physical model based approach, where in a finite element based modeling scheme was implemented for static soft tissue prediction and muscle simulation.

In their work, Tritto et al. [10] used vascular fractal geometries to describe the coupling between elastic network deformation and vascular branching pattern modification under simulated controlled skin expansion. The work also tested the role of elastic organization of the skin, the interrelation between skin tension, line orientation, pedicle axis and the apparently random proliferation of the branching vascular pattern.

### 1.2 Contact Analysis

Minimally Invasive Surgery is used as the preferred choice for many operations. Despite some advantages of MIS compared to the traditional surgery, the surgeon has almost complete lack of sense of touch that may cause damage to the tissue and this is a major drawback of this technology. In order to prevent any damage to the organ and tissues, determining the contact pressure and force between grasper and organ being grasped is

considered to be very important. In addition, MIS severely reduces the surgeon's sensory perception during manipulation. Surgery is essentially a visual and tactile experience and any limitation on the surgeon's sensory abilities are most undesirable. Comprehensive theoretical, finite element and experimental analysis as well are employed to determine the contact pressure and force on tissues.

The most important quantities involved in grasping are the contact pressure $P$, contact area $A$ or alternatively, the relationship between indentation pressure $P$ and contact depth $h$, during loading and unloading. These quantities can then be used to determine the constitutive properties of the material by taking advantage of results from earlier theoretical and experimental analyses by Tabore [11], Johnson [12] and Doerner and Nix [13].

Johnson [12] suggested that the outcome of wedge contact on an elastic plastic material would fall into one of three levels depending on the material properties and type of indenter. The three levels can be characterized as follows: In level one, very little plastic deformation occurs during penetration and all global properties can be derived from an elastic analysis. In case of Hertzian problem such as spherical or cylindrical tooth, Spence [14], Sackfield and Hills [15] and Barber [16] presented some solutions to obtain the contact pressure. Nowell [17] verified the contact of elastic cylinders under normal and tangential loading. Further investigations were mostly based on stress analysis of elastic solid under penetration by non-Hertzian indentations [18,19,20 ]. They presented a method to obtain the contact pressure in the case of normal and tangential loading on the object. Greenwood [21,22] and Johnson [23,24,25,26] have verified the effects of friction

and adhesion on the contact surfaces mostly in elastic regions. However, they could not give an exact solution for the effects of friction on the total amount of contact pressure.

In level two, an increasing amount of plastic deformation is presented and both the elastic and plastic properties of the material will influence the outcome of the contact pressure. Johnson [12] suggested, based on the fact that in such a situation the stress field just beneath the indenter is almost hydrostatic, that the process was very similar to the case of expansion of a spherical cavity in a large solid due to an internal pressure and presented the formula (for sharp cone tooth) as:

$$P = \frac{2}{3} Y[1 + \ln(\frac{E \tan \beta}{3(1-\upsilon^2)Y})] \tag{1-1}$$

where $P$, $Y$, $E$, $\nu$ and $\beta$ are contact pressure, Yield stress, Young's Modulus, Poisson's ratio and cone semi-angle, respectively. There are many studies concerning the elastoplastic contact analysis mostly in case of smooth and rough surfaces [27,28,29,30,31,32,33], but for the sharp teeth, Johnson model still gives the best solution.

For the sphere contacts Vu et al [34] and Liu, Liu and Wange [35] presented some models for the normal force-displacement in plastic region.

Finally, in level three, plastic deformation is present all over the contact area and elasticity no longer influences the contact pressure. This is also the region pertinent to most standard engineering materials, such as steel, aluminum and copper just to mention a few. By analyzing the results from a number of experiments, Tabor [11] concluded that contact pressure in level three could be derived from the simple formula

$$P = CY \tag{1-2}$$

where $P$ is mean contact pressure, $Y$ is yield stress and $C$ is a constant whose value is about 3 and only depends on the geometry of the teeth. This relation can still be used for metal strain-hardening, even though there is no definite yield stress, by taking $Y = Y_r$ to be the stress in a simple compression test measured at representative strain $\varepsilon_r$, which is determined by the geometry of indenter. In this context, it should also be mentioned that the representative stress used by Johnson equation (1-1) is essentially defined in the same way as proposed by Tabor [11]. In short, Johnson and Tabor equations (1-1) and (1-2) have been used extensively in order to determine the contact pressure with sufficient accuracy. However, with development of modern computers and new numerical methods, it has been possible to investigate the region of validity for the above-mentioned formula in some more detail by computational simulations of indentation of materials with tailored constitutive properties. In doing so, Giannakopoulos [36] and Larson [37] analyzed Vickers and Berkovich penetration of elastic plastic materials by using finite element methods and found that high accuracy could only be achieved, when using an equation with the same form, as equation (1-1), by describing the contact pressure with two parameters. Bhattacharya and Nix [38,39] and Laursen [40] have also performed numerical investigations of cone-tooth indenter, but these studies have not addressed the issue of the accuracy of equations (1-1) and (1-2) except for the case of elastic perfectly plastic material.

Further verifications on contact mechanics of wedge indenter in plastic region presented by Truman [41], Storakers and Larsson [42], Klabring [43], Larsson [44] and Bonakdar [45] comprised the effects of wedge angle on the mean pressure.

Grasping contact analysis is mainly affected by material behavior, shape of the indenter and friction between the grasper and the object. Since most tissues behave like viscoelastic materials, we extend our analysis to the contacts on viscoelastic models. The theoretical studies of linear viscoelastic bodies in contact, became active since 1950s by the work of Read [46] Lee [47], Radok [48], Lee and Radok [49], Hunter [50], Graham [51,52] and Ting [53,54]. In recent years, a number of studies have extended the early work to the analysis of indentation measurements in viscoelastic solids using either conical or spherical indenters [55,56,57,58,59,60,]. Bonakdar et al [61,62,63,64] recently studied the grasping contact pressure for both elastic and viscoelastic materials analytically. In the present thesis, we investigate teeth-like contact grasping in linear viscoelastic materials using analytical and finite element methods. Finally, experimental tests will be carried out to validate our analysis.

### 1.3 Tissue Characterization

Tactile sensing is defined as continuous sensing of variable contact forces. The tactile sensation may be defined as sensing ability of human finger (contact pressure, force, compliance, temperature, and roughness). Surgery is perhaps the most exciting and rapidly developing area where tactile sensing is actually of central importance. The reason that tactile sensing is so important in surgery is that, soft tissue can only be properly examined and identified by assessing its softness, viscosity and elasticity properties. The palpation of tissues and organs is an essential procedure that surgeons value highly.

To perform the MIS more effectively, the surgeon should be able to feel the tissue, sense the pressure of blood vessels and ducts during the procedure. This ability is of great use during the manipulation tasks, such as, the grasping of the internal organs, gentle load transfer during lifting, suturing and removing tissues [65]. The need to feel the tissue and its softness is particularly important during operation. In MIS surgery, stereoscope vision and tactile information about tissue consistency are no longer available to the surgeon. To compensate for these sensory deficits, various tissues can be characterized with an electromechanical sensor that records their properties. In future, these sensors will be integrated into surgical instruments, providing the surgeon with information about tactile properties of tissue [66]. Advancement in this regard in developing a process, which can restore the tactile feedback to the surgeon, will be of great benefit.

In laparoscopy, long slender tools are inserted through small puncture openings in the abdominal wall and the surgeon uses a range of tip mounted instruments guided by video feedback images. As the instruments are rigid rods and effectively have fixed pivots at the entry points, the available degrees of freedom are restricted and therefore demand extra operator expertise. It is clear that tactile sensing is greatly needed in this area.

Surface texture and roughness perception of various tissues are also important for inspecting the texture of tissue by endoscopic grasper during MIS surgery. Texture perception is different from roughness. To find out the surface texture perception, the tactile sensor must be capable of measuring the roughness, compliance and viscoelastic behavior. Since tissue is viscoelastic and behaves non-linearly, sensor must be capable of measuring compliance as a function of time so that the viscoelastic properties of the tissue can be ascertained [67]. Untill now very little work has been done in the field of

viscous behavior of tissue. A lot of work has been done for tactile perception of the tissue during minimal invasive surgery and perception of their elastic behavior.

The range of precision necessary for tactile sensing in minimally invasive surgery range from microns to few millimeters. The present day tactile sensors to be employed in a MIS must have small size, high sensitivity, low manufacturing cost, and ease of disposal after a surgery. The need of integrating all these aspects led to the utilization of microfabrication and MEMS in the field of tactile sensing and MIS.

The ultrasonic tactile method is entirely non-destructive in its use as a sensor. A microrobot was designed for colonoscopy using a pneumatic inchworm propulsion method described by Dario et al [68]. The difficulties of adopting totally autonomous robotic systems in surgery are discussed by Howe et al [69] and an approach is developed where the surgeon maintains supervision and control but is constrained from driving the cutting tools outside force limited regions.

Josivaldo et al [70] developed the strain gauge type tactile sensor for measuring finger force. It was constructed using metallic strain gauges. It is rugged, has linear response, good repeatability, resolution of 0.3 N, low hysteresis and sensitivity of 0.12 V/N.

Shinoda et al [71] designed the acoustic cell ultrasonic sensing matrix which are placed face to face. They used this sensor for mounting on the robots finger with 5-D deformation. Sensor measured 10μm displacement by 18.5 mm cell height and 0.001 rad change in surface inclination. This sensor could measure contact force as well as slip of the grasped object.

Dargahi et al, [72] developed the prototype for tactile sensing system with only three sensing element "PVDF". The magnitude and position of force is obtained by using

triangulation approach combined with membrane stress. The lack of agreement between the theoretical and experimental results could be attributed both to the experimental errors and the assumption in the theoretical analysis. Ohka et al [73] developed the optical tactile sensor equipped with an optical wave guide plate mounted on a robot manipulator. The experimental results confirmed that the tactile sensor is capable of detecting the distribution of three axis force and that the calculated and experimental results agree well. This tactile sensor comprised a CCD camera, light source, an acrylic board and a silicon rubber sheet that are assembled into a casing. Providing light source with endoscope is a new problem to overcome.

Obana et al [74] designed a semiconductor strain gauge tactile transducer. It was designed with the goal of measuring finger force without affecting the hand dexterity. Semiconductor strain gage was used due to its small size, and high sensitivity, but it has high temperature sensitivity. The transducer has both dynamic and static responses, negligible hysteresis and good linearity. Force sensitivity was 0.05 V/N. This sensor is ideal for measuring the force applied on the tissue. But the problem is to find out the softness of the tissue and to avoid tissue damage. Howe et al [75] also designed capacitive tactile array sensor which is based on an earlier design of Fearing [76]. This device measures the pressure distribution at the contact between the robot hand and the grasped object. Experiments confirm the system's ability to convey significant contact information.

Faraz et al, [77] designed haptic interface for endosurgery. The design consists of tunable spring based on the haptic and surgical requirements. Simulation and experimental results demonstrated the practicality of such design concept.

Petter et al [78] developed a new tactile measurement system, which is capable of differentiating the hardness of various soft materials such as living tissues. The system measures the mechanical frequency response of the tissue. It is intended to integrate this "vibrotactile sensor" inside the top of a tactile rod for endoscopic surgery, in order to provide the surgeon a substitute for the missing tactile feeling. Locating arteries hidden beneath superficial tissue is a difficult task in MIS. Ryan et al [79] developed a system, that can find the paths of arteries using tactile sensing in MIS. The surgeon begins by using the surgical robot to place the tactile sensor instrument on a known artery location. Signal processing algorithms locate the artery from its pulsatile pressure variation. The problems with compliance in the system result in occasional loss of the artery path. To perform MIS effectively, surgeons should be familiar with the quantitative assessment of the biomedical properties of soft tissues. Many different layouts were proposed and designed for examining the tissue behavior while performing minimal invasive surgery. Yongping et al [80] developed an ultrasound indentation system with a pen-size hand held probe that is used to obtain the indentation responses of lower limb soft tissues. A linear elastic indentation solution was used to extract the effective Young's modulus that ranged from 10.4 to 89.2 kPa for soft tissues. The Young's modulus determined was demonstrated to be significantly dependent on site, posture, subject and gender. No significant correlation was established between the effective Young's modulus and the thickness of entire soft tissue layers.

Bonakdar et al [81, 82] could recently measure both force and compliance of Kelvin-Voight model of tissues by a specially designed sensor.

## 1.4 Objectives

This thesis presents a novel method to determine the contact pressure on the surface of objects grasped by a grasper as well as the tissue properties with applications in Minimally Invasive Surgery (MIS). The contact stresses between the tissue and endoscopic grasper is analyzed. The present endoscopic grasper is corrugated (tooth-like) in order to grasp slippery tissues. The aim is to prevent any damage on tissue when grasped by an endoscopic grasper. It is highly important to avoid tissue damage during grasping and tissue manipulation by endoscopes. The study is done using analytical, finite element and experimental methods. In addition, in tactile sensing, the sensing elements are located at some distance beneath the surface of the tactile sensor. Therefore, it is essential to determine the exact contact pressure on the surface of the tissue and tactile sensor. The relationship between the measured quantity and the exact contact pressure has to be carefully evaluated.

In order to determine the properties and particularly the compliance (which is used to identify the sense of touch) of the biological tissues during MIS, we carry out analysis, design and fabrication of a four tooth microfabricated tactile sensor integrated on the upper and lower jaws of an endoscopic surgical grasper tool. Actually, one of the major problems in MIS is lack of the sense of touch and we try to compensate this problem. As a result, the main objectives of this PhD thesis is to determine the contact stresses as well as tissue properties when a surgical endoscopic device is grasping the biological tissue during surgery.

## 1.5 Thesis Overview

Chapter 1 gives an overview of minimally invasive surgery, contact analysis and tissue characterization. It enumerates the various contributions by different people in the field of minimally invasive surgery, grasping contact analysis and tactile sensing over the past decades.

Chapter 2 has an overview to the contact analysis theories and a specific view to the non-continuous shapes of contact such as wedges.

In chapter 3, the theory of viscoelasticity is described. The definition of viscoelasticity and the related equations are defined. Three standard modes which are used in this thesis are introduced.

In chapter 4, analytical and finite element methods are employed to determine the contact pressure on the surface of a tissue being grasped by an endoscopic grasper, in minimally invasive surgery. A comprehensive closed form solution along with finite element and experimental analysis of grasping contact pressure on viscoelastic materials, which have similar properties as, that of biological tissues are carried out. The behavior of a grasper with wedge-like and semi-cylindrical teeth, when pressed into a linear viscoelastic material is examined. In addition, a finite element analysis is carried out in Ansys- 10 software. Finally, the experimental results are presented to validate both analytical and FEM results. The results of this study provide a closed form expression for grasping contact pressure and contact area along with the variations of stress in tissue obtained through FEM analysis.

In chapter 5, we present the design, analysis, fabrication and assembly of four tooth microfabricated tactile sensors integrated with the upper and lower jaws of an endoscopic

surgical grasper tool, in order to determine the properties and particularly the compliance of the biological tissues during minimally invasive surgery. Two viscoelastic Kelvin-Voight and Kelvin models are employed for tissue characterization. A comprehensive closed form and finite element analysis have been carried out to express the relationship between the force ratio, compliance and the equivalent viscous damping of the tissue. The designed sensor uses a PVDF film as its sensing element. The sensor consists of arrays of rigid and compliant elements which are mounted on the tip of an endoscopic surgical grasper tool. Relative force between adjacent parts of the contact object is used to measure the viscoelastic properties.

In Chapter 6, the conclusions and summary of the theoretical and experimental work are presented.

At the end of thesis, three appendices are provided for covering the details of the related work. Appendix I explain the effect of friction on elastic contact pressure. Appendix II discusses about the properties and behavior of the PVDF materials that are presented in this section. Finally, Appendix III refers to the flow chart of the Ansys analysis.

# CHAPTER 2

# INTRODUCTION TO CONTACT ANALYSIS

## 2.1 Introduction to Elastic Contact Analysis

In general, a contact surface transmits tangential tractions due to friction in addition to normal pressure. An elastic half-space loaded over the strip by a normal pressure *p(x)* and tangential traction *q(x)* distributed in any arbitrary manner is shown in figure (2-1). We wish to find the stress components due to *p(x)* and *q(x)* at any point A in the body of the solid and the displacement of any point C on the surface of the solid. Stress field in a general loading can be written as follows [83]:

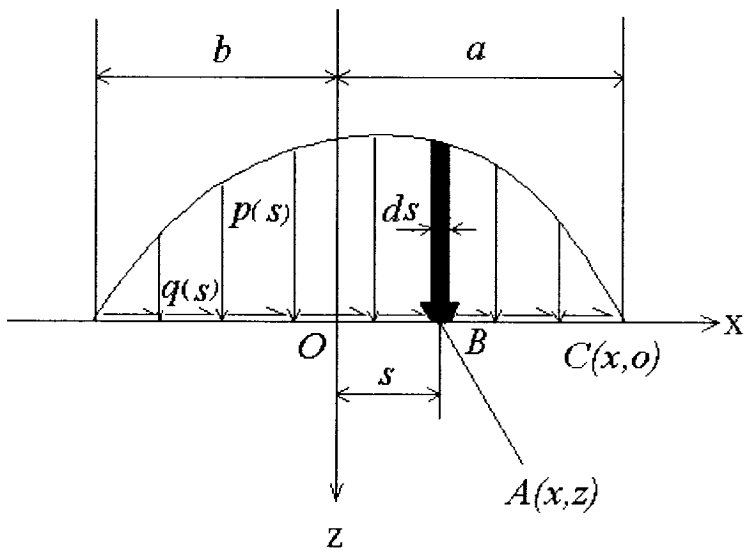


**Figure (2-1).** Distributed strip load over a solid.

$$\sigma_x = \frac{-2z}{\pi}\int_b^a \frac{p(s)(x-s)^2\,ds}{\{(x-s)^2+z^2\}^2} - \frac{2}{\pi}\int_b^a \frac{q(s)(x-s)^3\,ds}{\{(x-s)^2+z^2\}^2} \qquad (2\text{-}1)$$

$$\sigma_z = \frac{-2z^3}{\pi}\int_b^a \frac{p(s)ds}{\{(x-s)^2+z^2\}^2} - \frac{2z^2}{\pi}\int_b^a \frac{q(s)(x-s)ds}{\{(x-s)^2+z^2\}^2} \tag{2-2}$$

$$\tau_{xz} = \frac{-2z^2}{\pi}\int_b^a \frac{p(s)(x-s)ds}{\{(x-s)^2+z^2\}^2} - \frac{2}{\pi}\int_b^a \frac{q(s)(x-s)^2 ds}{\{(x-s)^2+z^2\}^2} \tag{2-3}$$

where $\sigma_x$, $\sigma_z$ and $\tau_{xz}$ are, respectively, normal stresses in x and z directions and shear stress. Denoting the tangential and normal displacement of point $C$ due to the combined action $p(x)$ and $q(x)$ by $u_x$ and $u_z$ respectively, these displacements are given as [83]:

$$u_x = -\frac{(1-2\nu)(1+\nu)}{2E}\{\int_b^x p(s)ds - \int_x^a p(s)ds\} - \frac{2(1-\nu^2)}{\pi E}\int_b^a q(s)\ln|x-s|ds + C_1 \tag{2-4}$$

$$u_z = \frac{(1-2\nu)(1+\nu)}{2E}\{\int_b^x q(s)ds - \int_x^a q(s)ds\} - \frac{2(1-\nu^2)}{\pi E}\int_b^a p(s)\ln|x-s|ds + C_2 \tag{2-5}$$

where $\nu$ is Poisson's ratio, $E$ is Young's modulus, $C_1$ and $C_2$ are constant values. We can easily obtain the gradient of the displacements by taking derivatives of displacements as:

$$\frac{\partial u_x}{\partial x} = -\frac{(1-2\nu)(1+\nu)}{E}p(x) - \frac{2(1-\nu^2)}{\pi E}\int_b^a \frac{q(s)}{(x-s)}ds \tag{2-6}$$

$$\frac{\partial u_z}{\partial x} = \frac{(1-2\nu)(1+\nu)}{E}q(x) - \frac{2(1-\nu^2)}{\pi E}\int_b^a \frac{p(s)}{(x-s)}ds \tag{2-7}$$

Having obtained *p(x)* and *q (x),* we can obtain stress, displacement and strain field.

To formulate the problem in a two dimensional elastic half space conveniently, we rewrite the equations (2-6) and (2-7) as follows:

$$\int_{-b}^{a} \frac{q(s)}{x-s} ds = -\frac{\pi(1-2\nu)}{2(1-\nu)} p(x) - \frac{\pi E}{2(1-\nu^2)} u_x'(x) \tag{2-8}$$

$$\int_{-b}^{a} \frac{p(s)}{x-s} ds = \frac{\pi(1-2\nu)}{2(1-\nu)} q(x) - \frac{\pi E}{2(1-\nu^2)} u_z'(x) \tag{2-9}$$

where, the derivative (prime) denotes $\partial / \partial x$.

We will use the above-mentioned equations to solve the elastic contact problems.

### 2.2 Wedge-like Tooth Contact Analysis

In this section, the influence of a sharp discontinuity in the slope of profile within the contact area with reference to the contact of a wedge with plane surface is examined. In order for the deformation to be sufficiently small to lie within the scope of the linear theory of elasticity, the angle $2\alpha$ of the wedge or cone must be an obtuse angle. If we take a two-dimensional wedge indenting a flat surface such that the width of the contact strip is small in comparison with the size of the two solids then we can use the elastic solution for a solid for both wedge and plane surfaces. In order to satisfy the above linearity conditions, the semi-angle α of the wedge must be close to 90.

Figure (2-2) shows a wedge penetrating into a solid. Since the profile of the wedge is given, we can write:

$$u_z = \delta - \cot\alpha |x| \qquad -a < x < a \tag{2-10}$$

In addition, taking the derivative, we have,

$$\frac{\partial u_z}{\partial x} = u_z' = -(sign(x))\cot\alpha \tag{2-11}$$

where $\delta$ is contact depth and,

$$sign(x) = \begin{matrix} +1 if, x > 0 \\ -1 if, x < 0 \end{matrix} \tag{2-12}$$

Since we have assumed that there is no friction between wedge and solid (lubricated surfaces), *q(x)* is zero. From equation (2-8), we can write:

$$u_z' = -\frac{2(1-\nu^2)}{\pi E}\int_b^a \frac{p(s)}{x-s}ds \tag{2-13}$$

Substituting equation (2-13) in equation (2-11) gives:

$$(sign(x))\cot\alpha = \frac{2(1-\nu^2)}{E}\int_b^a \frac{p(s)}{x-s}ds \tag{2-14}$$

To obtain *p(x)* we have to solve above singular integral. Applying Sohngen's method [84], we will finally obtain *p(x)* as,

$$p(x) = \frac{E\cot\alpha}{2\pi(1-\nu^2)}\ln[\frac{a+(a^2-x^2)^{1/2}}{a-(a^2-x^2)^{1/2}}] = \frac{E\cot\alpha}{\pi(1-\nu^2)}\cosh^{-1}(\frac{a}{x}) \tag{2-15}$$

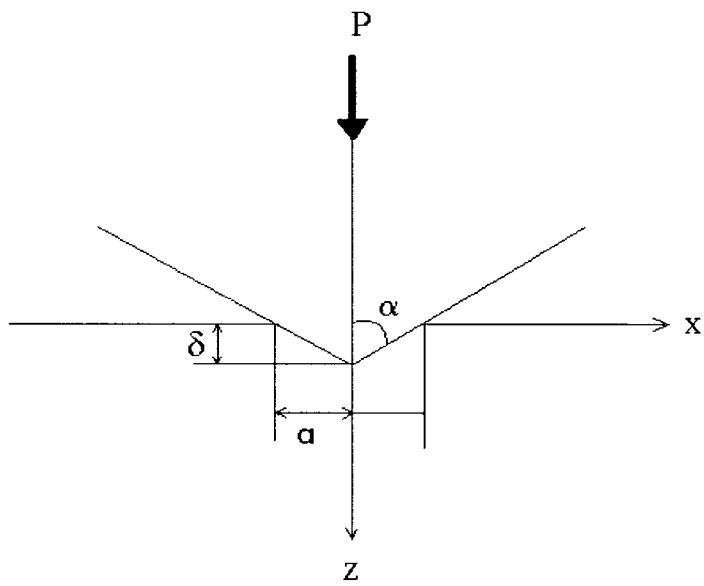


**Figure (2-2).** A rigid wedge indents to an elastic solid.

Figure (2-3) shows *p(x)* distribution in the solid. Pressure rises to an infinite value at the apex of the wedge. It would appear that the discontinuity in slope of the profiles within the contact region leads to a logarithmic singularity in pressure. Although the pressure is infinite at the apex of wedge the principal shear stress in x-z plane is not so.

It must be pointed out that the above-mentioned equations would be valid if the semi-wedge angle could be more than 90. This is because in case of small wedge angle, the displacements cannot be infinitesimal and our analysis that was based on elasticity theory may not be used.

We can find the mean pressure by integrating *p(x)* as follows:

$$\overline{p} = \frac{\int_{-a}^{a} p(x)\,dx}{2a} = \frac{E \cdot Cot\ \alpha}{2(1-\nu^2)} = \frac{G\,.Cot\ \alpha}{1-\nu} \qquad (2\text{-}16)$$

It means that the mean pressure only depends on $G$ (Shear modulus), Poisson ratio and wedge angle.

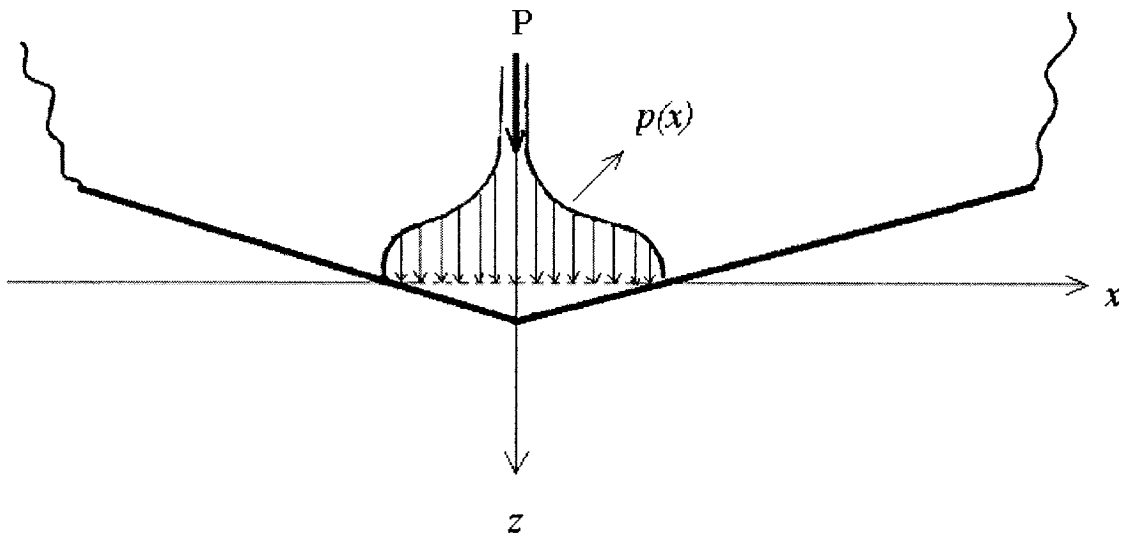


**Figure (2-3).** Contact pressure distribution over an elastic solid.

Contact analysis of an elastic wedge with an elastic solid considering friction is explained in appendix I.

# CHAPTER 3

# INTRODUCTION TO VISCOELASTICITY

Many materials, notably biological materials, biomaterials and polymers, exhibit time dependent behavior in their relationship between stress and strain, which is described as viscoelastic. The common features of viscoelastic behavior are illustrated in figure (3-1), which shows the variation of strain $\varepsilon(t)$ in a specimen of material under the action of constant stress $\sigma_0$ applied for a period $t_1$. The strain shows an initial elastic response $OA$ to the applied stress; a further delayed elastic strain $AB$ is acquired in time. If the material is capable of flow or creep it will also acquire a steadily increasing creep strain $BC$. When the stress is removed there is an immediate elastic response $CD$ $(= -OA)$ and delayed elastic response $DE$. The specimen is left with a permanent strain at $E$, which it acquired through the action of creep.

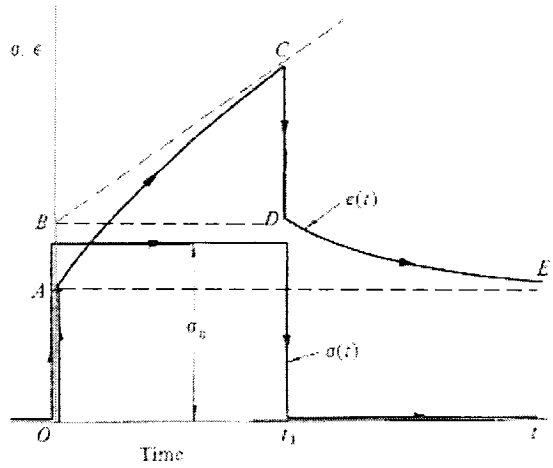


**Figure (3-1).** The variation of strain $\varepsilon(t)$ in a specimen of material under the action of constant stress $\sigma_0$ applied for a period $t_1$ [83].

This material behavior can be incorporated into a rigorous theory of contact stresses provided that the viscoelastic stress-strain relationships of the material can be taken to be linear. For this requirement to be met the strains must remain small (as in the linear theory of elasticity) and the principle of super position must apply. Thus, for linearity, an increase in the stress in figure (3-1) by a constant factor must produce an increase in the strain response by the same factor; further, the strain response to different stress histories must be identical to sum of responses to the stress histories applied separately. The stress-strain relations for a linear viscoelastic material can be expressed in various ways, but the most common is to make use of the creep compliance function which expresses the strain response to a step change in stress or, alternatively, the relaxation function, which expresses the stress response to a step change in strain. An isotropic material in a state of complex stress requires two independent functions to express its response to shear and volumetric deformation, respectively. These functions correspond to the shear modulus and bulk modulus of purely elastic solids. For simplicity, in what follows, we shall restrict our discussion to an incompressible material so that its stress-strain relations can be expressed in terms of a single function describing its behavior in shear. The approximation is a reasonable one for biological materials, tissues and polymers, whose Poisson's ratio usually exceed 0.4. It is convenient to write the stress-strain relationship in terms of the deviator stress components $s = (\sigma - \bar{\sigma})$ and the deviator strains $e = (\varepsilon - \bar{\varepsilon})$ where $\bar{\sigma} = \frac{1}{3}(\sigma_1 + \sigma_2 + \sigma_3)$ and $\bar{\varepsilon} = \frac{1}{3}(\varepsilon_1 + \varepsilon_2 + \varepsilon_3)$. For an incompressible elastic solid $\bar{\varepsilon} = 0$ so that $s = 2Ge = 2G\varepsilon$, where $G$ is the shear modulus.

The most common expression of stress-strain relations for a linear viscoelastic material makes use of the creep compliance function which gives the strain response to a step

change in stress or, alternatively, the relaxation function, which gives the stress response to a step change in strain [83]. An isotropic material in a state of complex stress requires two independent functions to express its response to shear and volumetric deformation. These functions correspond to the shear modulus and bulk modulus of purely elastic solids. Therefore, a viscoelastic solid can be described by the following constitutive relationships [83,85] between deviator stress and strain, $s_{ij}$ and $e_{ij}$,

$$s_{ij}(t) = 2\int_0 G(t-t')\frac{\partial e_{ij}(t')}{\partial t'}dt' \tag{3-1}$$

$$2e_{ij}(t) = \int_0 J_1(t-t')\frac{\partial s_{ij}(t')}{\partial t'}dt' \tag{3-2}$$

The function *G(t)* is the shear relaxation function or time dependent shear modulus, which specifies the stress response to a unit step change of strain; the function $J_1(t)$ is the creep compliance, which specifies the strain response to a unit change in stress. In the theory of elasticity $J_1$ is defined as $1/G$, where $G$ is shear modulus. Equation (3-1) expressed in terms of the relaxation function *G(t)*, can be regarded as the superposition of the stress responses to a sequence of small changes of strain $de(t')$ at times $(t')$. Similarly, equation (3-2) expresses the total strain response to a sequence of step changes in stress. Deviator stress and strain can be expressed in terms of,

$$s_{ij} = (\sigma_{ij} - \delta_{ij}\mathrm{I}_\sigma / 3) \tag{3-3}$$

$$e_{ij} = (\varepsilon_{ij} - \delta_{ij}\mathrm{I}_\varepsilon / 3) \tag{3-4}$$

where $\sigma_{ij}$ and $\varepsilon_{ij}$ are stress and strain. In addition, $\mathrm{I}_\sigma$ and $\mathrm{I}_\varepsilon$ are the first stress and strain invariants, respectively, which can be expressed as sum of principal stresses and strains as follows, $\mathrm{I}_\sigma = (\sigma_1 + \sigma_2 + \sigma_3)$ and $\mathrm{I}_\varepsilon = (\varepsilon_1 + \varepsilon_2 + \varepsilon_3)$

Alternatively, the dilatation stress-strain relation is expressed as [83,85],

$$\sigma_{ii}(t) = 3\int_0 B(t-t')\frac{\partial \varepsilon_{ii}(t')}{\partial t'}dt' \tag{3-5}$$

$$3\varepsilon_{ii}(t) = \int_0 J_2(t-t')\frac{\partial \sigma_{ii}(t')}{\partial t'}dt' \tag{3-6}$$

where $B(t)$ is the relaxation modulus in dilatation or time dependent bulk modulus and $J_2(t)$ is the volumetric compliance [85].

The constitutive principle can also be written as [86],

$$\sigma_{ij}(t) = \int_0 [2G(t-t')\frac{\partial \varepsilon_{ij}(t')}{\partial t'} + \delta_{ij}\lambda(t-t')\frac{\partial \varepsilon_{kk}}{\partial t'}]dt \tag{3-7}$$

where $\lambda(t) = (3B(t) - 2G(t))/3$.

The time dependant Young's modulus and Poisson's ratio, respectively, are given by,

$$E(t) = [9G(t)B(t)]/[3B(t) + G(t)]\ ,\quad \upsilon(t) = [E(t)/2G(t)] - 1 \tag{3-8}$$

In fact, the relationship between the relaxation and creep functions $G(t)$ and $J_1(t)$, as well as $B(t)$ and $J_2(t)$, are expressed in simple forms after transforming them using Laplace transformation [85,87],

$$\int_0 J_1(t-t')G(t')dt' = \int_0 J_1(t')G(t-t')dt' = t \tag{3-9}$$

$$\int_0 J_2(t-t')B(t')dt' = \int_0 J_2(t')B(t-t')dt' = t \tag{3-10}$$

For particular materials, equation (3-1) and (3-2) may be deducted to appropriate spring and dashpot models. Equation (3-1) expressed in terms of the relaxation function *G(t)*, can be regarded as the superposition of the stress responses to a sequence of small

changes of strain $de(t')$ at times $(t')$. Similarly, Equation (3-2) expresses the total strain response to a sequence of step changes in stress.

In chapter 4, we will make use of two idealized viscoelastic materials, which demonstrate separately the effects of delayed elasticity and steady creep. The first model includes a spring of modulus $g_2$ parallel to a dashpot of viscosity $\eta$, which are in series with another spring with modulus $g_1$. For this material, the creep response to a step change in stress $s_0$ is given by [83,85],

$$e(t) = 0.5J_1(t)s_0 = \{\frac{1}{g_1} + \frac{1}{g_2}[1 - \exp(-t/T_1)]\}s_0 \tag{3-11}$$

where $T_1 = \eta/g_2$ . The response to a step change of strain $e_0$ is given by [83,85],

$$s(t) = 2G(t)e_0 = \frac{g_1}{g_1 + g_2}[g_2 + g_1 \exp(-t/T_2)]e_0 \tag{3-12}$$

where $T_2 = \eta/(g_1 + g_2)$

The second material, Maxwell body, is a spring of modulus $g$ in series with a dashpot of viscosity $\eta$. The creep response is [83,85],

$$e(t) = 0.5J_1(t)s_0 = [\frac{1}{g} + \frac{1}{\eta}t]s_0 \tag{3-13}$$

and the relaxation response is [83,85],

$$s(t) = 2G(t)e_0 = [g \ \exp(-t/T)]e_0 \tag{3-14}$$

where $T = \eta/g$ is the relaxation time of the material.

The first material exhibits delayed elasticity but the ultimate strain is limited to a finite value. The second material shows a steady creep under constant stress, so that it strains

continuously with time. This model is only valid during time intervals when the strains remain small. For Maxwell model to be representative of a solid rather than fluid, the viscosity must be large, comparable in magnitude to the modulus of elasticity.

In chapter 5 we use Kelvin-Voight and Kelvin modes for the sensor-tissue analysis. Kelvin-Voight model includes a spring of modulus $g$ parallel to a dashpot of an equivalent viscous damping coefficient $c$. For Kelvin-Voight model the constitutive equation is expressed as,

$$c\dot{e}(t) + ge(t) = s_0 \tag{3-15}$$

The creep response to a step change in stress $s_0$ is given by,

$$e(t) = 0.5J_1(t)s_0 = \frac{1}{g}(1 + \exp(-t/T)s_0 \tag{3-16}$$

where $T = g/c$

Constitutive equations for Kelvin model are studied in chapter 5.

# CHAPTER 4

# VISCOELASTIC GRASPING CONTACT ANALYSIS

In the previous chapters a brief discussion on the contact mechanics and viscoelastic analysis was provided, which will be useful to study the grasping contact analysis of organs which may be treated as viscoelastic materials.

In this chapter, analytical and finite element methods are employed to determine the contact pressure on the surface of a tissue being grasped by an endoscopic grasper, in Minimally Invasive Surgery (MIS). It is highly important to avoid damage to the tissues while grasping and manipulation during endoscopic surgery. Therefore, it is essential to determine the exact contact pressure on the surface of the tissue. To this end, initially a comprehensive closed form, finite element and experimental analysis of grasping contact pressure on viscoelastic materials which have similar properties as that of biological tissues is studied. The behavior of a grasper with wedge-like and semi-cylindrical teeth, when pressed into a linear viscoelastic material is examined. Initially, a single wedge penetrating into a solid is studied and then is extended to the grasper. The elastic wedge indentation is the basis of the closed form analysis and the effects of time are included in the equations by considering the corresponding integral operator from viscoelastic stress-strain relations. In addition, a finite element analysis is carried out in Ansys- 10 software. Finally, the experimental results are presented to validate both analytical and FEM results. The results of this study provide a closed form expression for grasping contact pressure force and contact area along with the variations of stress in tissue obtained through FEM analysis.

## 4.1 Grasping Contact Analysis of Biological Tissues with Wedge-liked Teeth Grasper with Applications in Minimally Invasive Surgery

### 4.1.1 Viscoelastic Contact Analysis

In chapter two the contact pressure between a wedge and an elastic solid as shown in figure (4-1) has been expressed as,

$$p(x) = \frac{E \cot \alpha}{\pi(1-\nu^2)} \cosh^{-1}(\frac{a}{x}) \tag{4-1}$$

where $E$, $\nu$ and $a$ are Young's modulus, Poisson's ratio and contact area respectively. Using equation (4-1), the changes of the contact pressure against $x$ can be plotted. This is shown in figure (4-2). It can be seen that for an elastic object the contact pressure gradually reduces away from the tip of the wedge.

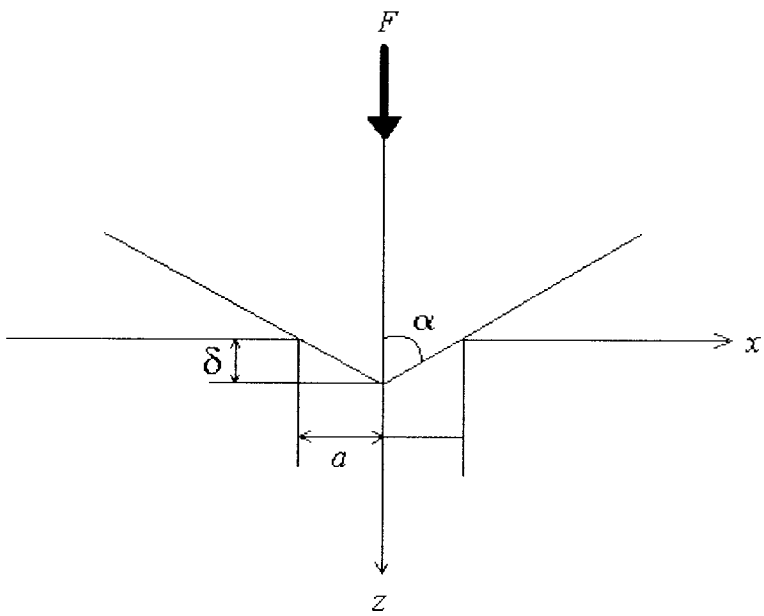


**Figure (4-1).** Rigid wedge indenting into a viscoelastic solid.

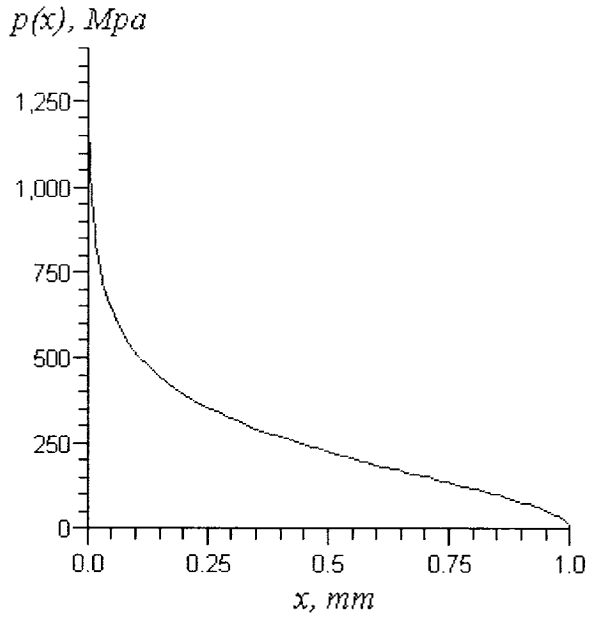


**Figure (4-2).** Variation of the contact pressure in an elastic contact along transverse direction (*G=235 Mpa, a=1mm, α=60°, v=0.5*).

When the material is viscoelastic, contact pressure and area vary with time and hence, following Radok's suggestion [48], the Poisson's ratio is considered time independent and *E(t)* is replaced by $2G(t)(1+\upsilon)$ . Consequently equation (4-1) is expressed as,

$$p(x,t) = \frac{2\cot\alpha}{\pi(1-\upsilon)} \int_0^t G(t-t') \frac{\partial \cosh^{-1}(a(t')/x)}{\partial t'} dt' \tag{4-2}$$

The integral form of equation (4-2) can be interpreted as the linear superposition of small changes in *p(x,t)* caused by infinitesimal step changes in contact area. Therefore, for both the models defined by equations (3-11) to (3-14) in chapter 3, for a constant value of contact area with incompressibility condition ($\upsilon = 0.5$), equation (4-2) can be rewritten as,

$$p(x,t) = \frac{4G(t)\cot\alpha}{\pi}\cosh^{-1}(\frac{a}{x}) \tag{4-3}$$

For the elastic contact, the relationship between contact area, $a$, and force, $F$, is given by,

$F = \int_{-a}^{a} p(x)dx = \frac{2aG\cot\alpha}{(1-\upsilon)}$ , where $p(x)$ is taken from equation (4-1) and $F$ is force per unit of length. Then,

$$a = \frac{F(1-\nu)}{2G\cot\alpha} \tag{4-4}$$

When the Poison's ratio is assumed 0.5 for a viscoelastic material, equation (4-4) can be written as,

$$a(t) = \frac{1}{4\cot\alpha}\int_0^t J_1(t-t')\frac{\partial F(t')}{\partial t'}dt' \tag{4-5}$$

Under a step load, $a(t)$ becomes,

$$a(t) = \frac{1}{4\cot\alpha}J_1(t)F \tag{4-6}$$

By considering the delayed elasticity material and using equations (4-3) and (4-6), we can express the contact pressure as,

$$p(x,t) = \frac{2g_1[g_2 + g_1\exp(-t/T_2)]\cot\alpha}{(g_1+g_2)\pi}\cosh^{-1}(\frac{a}{x}) \tag{4-7}$$

and,

$$a(t) = \frac{F}{2\cot\alpha}[\frac{1}{g_1} + \frac{1}{g_2}(1-\exp(-t/T_1))] \tag{4-8}$$

Figure (4-3) shows the changes in contact pressure against time and location. It is seen that at the constant value of the strain contact pressure decreases rapidly and reduces towards a constant value, which is the steady state.

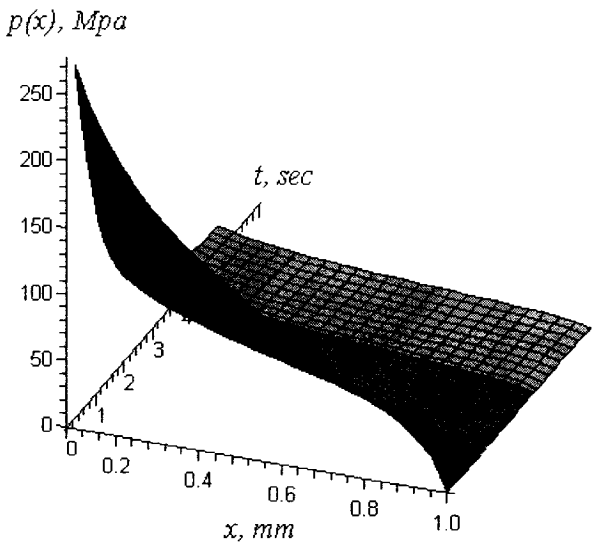


**Figure (4-3).** Variation of contact pressure in delayed elasticity material against time and along transverse direction ($g_1$ = *235 Mpa*, $g_2$= *26 Mpa*, $\alpha$=*60°*, $T_2$=*1sec*, *a=1mm*).

Figures (4-4) shows the increase in contact area with time under a constant value of force.

This is a critical situation in MIS and can damage the tissues.

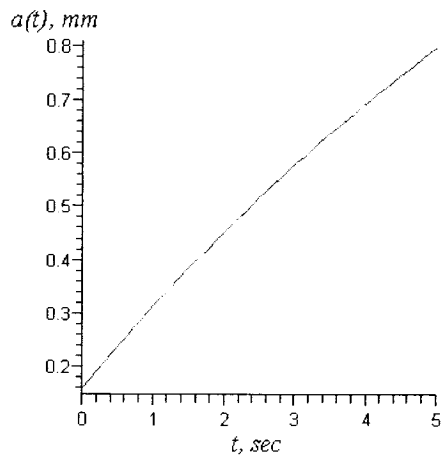


**Figure (4-4).** Increase of contact area with time in delayed elasticity material under constant force ($T_1$=*10 sec*, *F=50 N/mm*, $g_1$ = *235 Mpa*, $g_2$= *26 Mpa*, $\alpha$=*60°*).

If Maxwell solid is considered, the contact pressure and area are given by,

$$p(x,t) = \frac{2g.\exp(-t/T).\cot\alpha}{\pi}\cosh^{-1}(\frac{a}{x}) \tag{4-9}$$

$$a(t) = \frac{F}{2\cot\alpha}(\frac{1}{g}+\frac{1}{\eta}t) \tag{4-10}$$

As shown in figure (4-5), the change in the contact pressure with time is very fast but the pressure tends towards zero for a constant $a$, which cannot be true in reality.

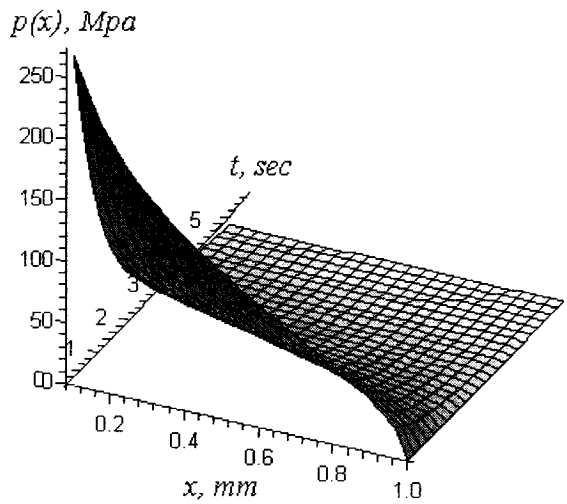


**Figure (4-5).** Change of contact pressure in Maxwell material against time and along transverse direction (*T=1sec, g = 235 Mpa, α=60°, a=1mm*).

### 4.1.2 Grasping contact analysis

For the purpose of analysis, the contact stresses around the single tooth are assumed to be concentrated close to the contact area and decrease rapidly in intensity with distance from the point of contact. Thus, the region of interest lies close to the contact. Provided the dimensions of the tissue are large compared with the dimensions of the contact area, the stresses in this region are not critically dependent upon the shape of the tissue distant from the contact area. On the other hand, since the linear viscoelastic theory is

considered, the superposition principle can be evoked to analyze the grasping contact problem.

Considering figure (4-6) which shows the schematic of grasper, and equation (4-7), the grasping contact force per unit length on the top of the delayed elasticity material for constant indentation area can be written as,

$$F(t)=\frac{2g_1[g_2+g_1\exp(-t/T_2)]\cot\alpha}{\pi(g_1+g_2)}\left[\int_a \cosh^{-1}\left(\frac{a}{x}\right)dx+\int_{\Delta-a}^{\Delta+a}\cosh^{-1}\left(\frac{a}{x-\Delta}\right)dx+\int_{2\Delta-a}^{2\Delta+a}\cosh^{-1}\left(\frac{a}{x-2\Delta}\right)dx+\cdots\right] \quad (4\text{-}11)$$

or,

$$F(t)=\frac{2Nag_1[g_2+g_1\exp(-t/T_2)]\cot\alpha}{(g_1+g_2)} \quad (4\text{-}12)$$

where $N$ is the number of teeth of the grasper.

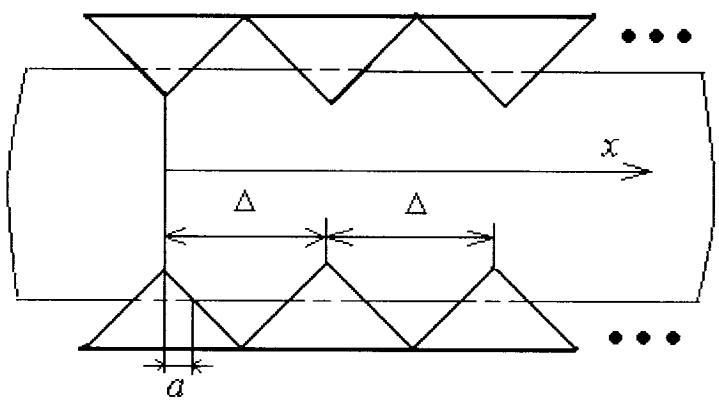


**Figure (4-6).** Schematic of grasper with wedge teeth.

As shown in figure (4-7), total force applied to the grasper decreases with time for a constant value of contact area.

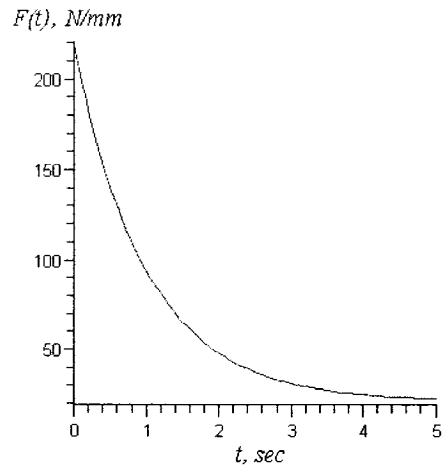


**Figure (4-7).** Decay of total force against time for the grasping contact with wedge teeth grasper ($g_1$ = *235 Mpa,* $g_2$= *26 Mpa,* $\alpha$=*60°,* $T_2$=*1sec, a=0.1mm, number of teeth:8*).

Considering equation (4-8) for a constant indenting load, the creep of the contact area would be,

$$a(t) = \frac{F}{2N.\cot\alpha}[\frac{1}{g_1} + \frac{1}{g_2}(1 - \exp(-t/T_1))] \qquad (4\text{-}13)$$

Equation (4-13) expresses the variation of contact area with time in different values of a step force. In figure (4-8), increase in the contact area with time in different values of step load is shown. In MIS when a surgeon uses the graspers, it is imperative to understand that contact area and consequently contact depth will increase under a constant load. Otherwise, there is a possibility of causing damage to the organs.

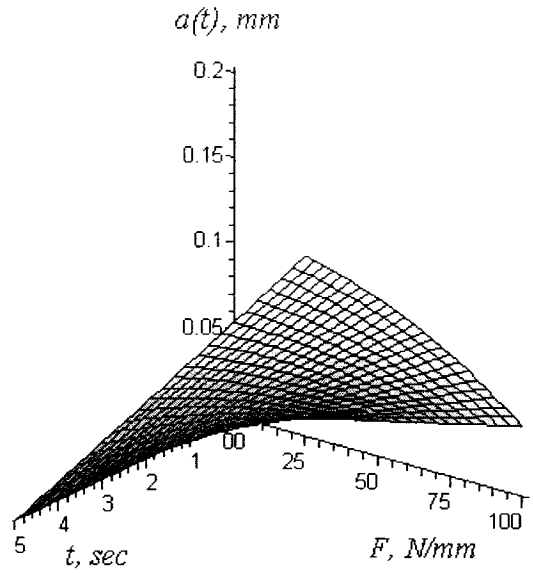


**Figure (4-8).** Increase of contact area with time in delayed elasticity material against force (*$T_1$=10, $g_1$ = 235 Mpa, $g_2$= 26 Mpa, α=60°, number of the teeth: 8*).

### 4.1.3 Finite Element Analysis

A comprehensive finite element analysis is conducted using Ansys 10 (For more information, refer to the Appendix III). In this analysis, a 20 mm thick tissue is grasped by two jaws of a tooth-like endoscopic grasper. Figure (4-9) shows the grasper-tissue model. A viscoelastic Plane-182 element has been considered for the model. This element is the most suitable choice for viscoelastic materials in two dimensions.

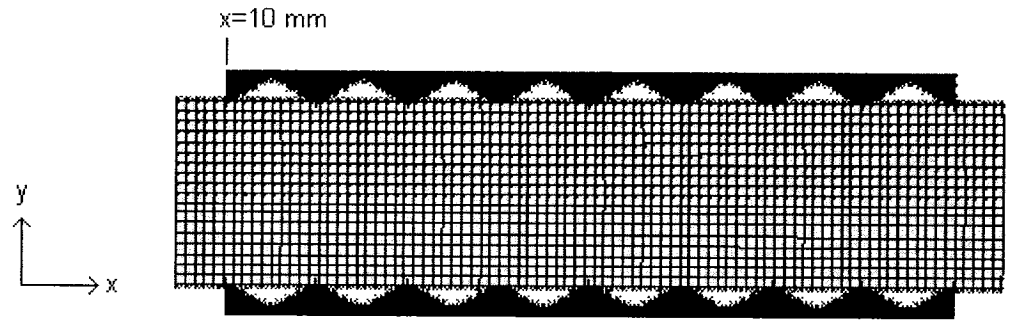


**Figure (4-9).** Ansys model for tissue and grasper (*tip to tip distance of the teeth: 5 mm, semi-angle of each tooth: α=60°, thickness of the tissue: 20 mm*).

The boundary conditions for this model are shown in the figure (4-10). Because of the symmetry, tissue is fixed at symmetry line along the tissue length. A uniformly distributed load is applied to the grasper, which is fixed along x-axis in its one side.

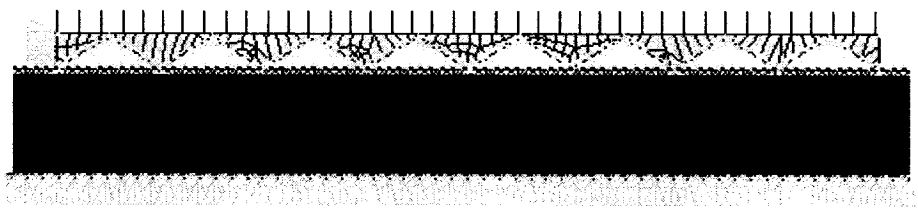

**Figure (4-10).** Meshing and loading of semi-model.

In this analysis the shear modulus of the tissue is obtained using equation (3-12). Table (4-1) shows the values of time dependent shear modulus used in this analysis.

**Table (4-1).** Time dependent shear modulus.

| *t (sec)* | 0 | 1 | 2 | 3 | 4 | 5 |
|---|---|---|---|---|---|---|
| *G(t)* *Mpa* | 117.5 | 50.62 | 26.21 | 17.07 | 13.70 | 12.44 |

When the teeth of the grasper is indented into the tissue, deformation of the tissue, Von Mises stress, stresses in *x*, *y* (normal stresses) and *y-x* directions (shear stress) are obtained and shown in figures (4-11) to (4-16).

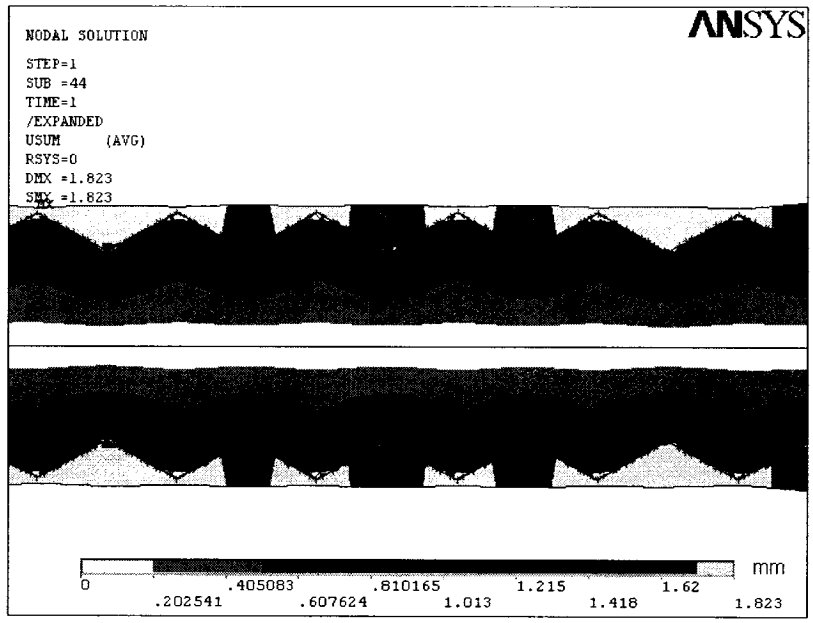


**Figure (4-11).** Deflection of the tissue when grasped.

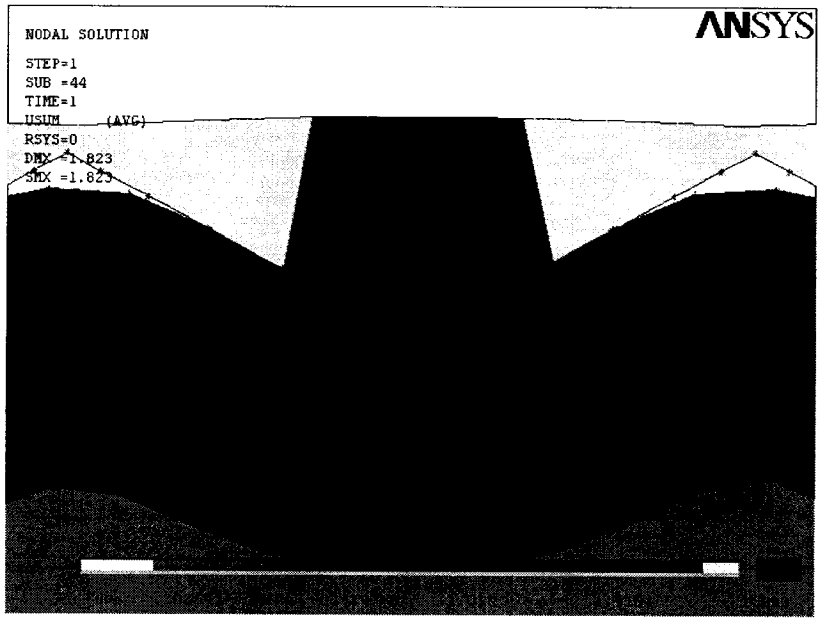


**Figure (4-12).** Local deformation of tissue by a tooth.

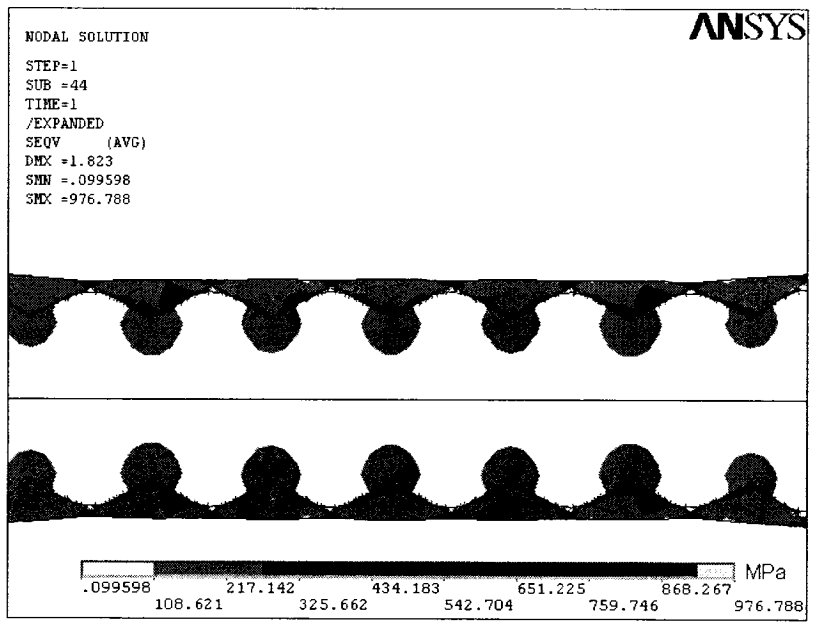


**Figure (4-13).** Von Mises stress in tissue.

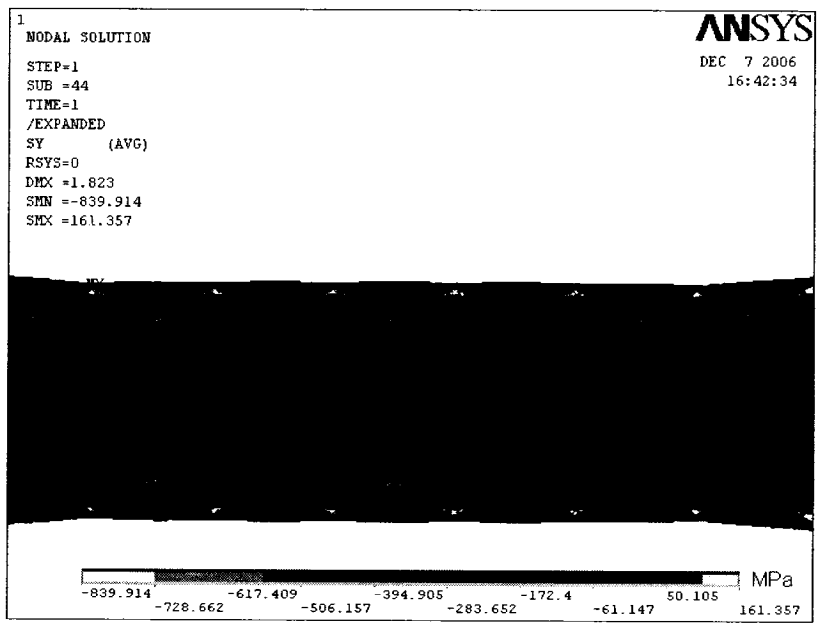


**Figure (4-14).** Normal stress in y-axis.

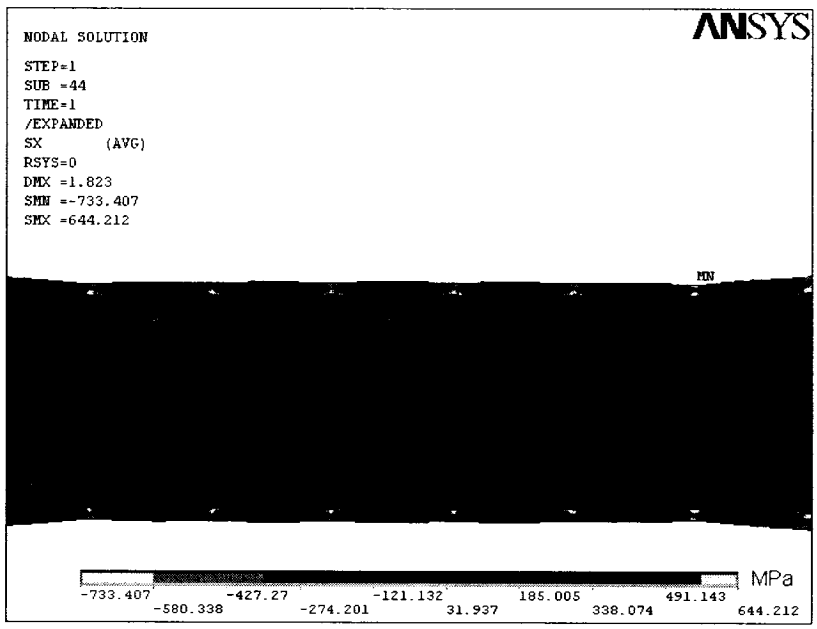


**Figure (4-15).** Normal stress in x-axis.

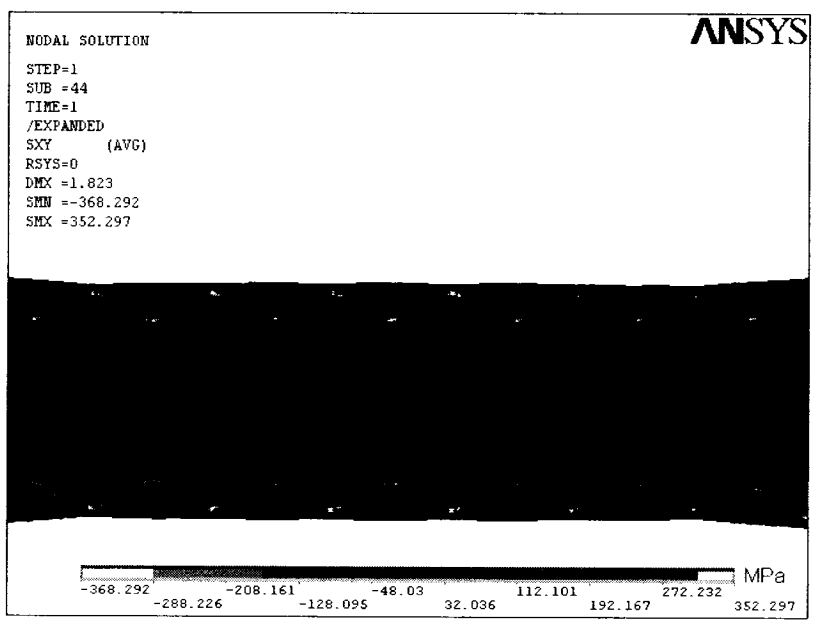


**Figure (4-16).** Shear stress in xy-axis.

Following relations are employed to calculate pressure in the contact surfaces:

$$p(x,t) = s_{ij}(x,t)n_i n_j \tag{4-14}$$

where, $n_i$ or $n_j$ are normal to the contact surfaces and $s_{ij}$ are the values of stresses on the surface of the contact area. For the grasper with semi angles of 60°, normal to the surface is given as:

$\vec{n} = -0.5\vec{i} + 0.866\vec{j}$, for the right side of teeth (4-15)

$\vec{n} = 0.5\vec{i} + 0.866\vec{j}$ , for the left side of teeth (4-16)

Substituting the values of stresses resulting from FEA in equation (4-14), we can calculate the contact pressure. It has been found that a close agreement exists in the contact pressure obtained from FEM and that by closed form solution. In general, the FEA yielded higher values than those by closed form analysis except in a few isolated cases without any identifiable trends. The magnitudes of contact pressure under the same loading and situation of the analytical part are outlined in the table (4-2).

**Table (4-2).** Comparison of contact pressures by finite element and closed form analysis*

| *x (mm)* | *FE(Ansys) P(x),MPa* | *Analytical P(x),MPa* | Difference (%) | *x (mm)* | *FE(Ansys) P(x),MPa* | *Analytical P(x),MPa* | Difference (%) |
|---|---|---|---|---|---|---|---|
| 10.1 | 315.95 | 317.19 | -0.3 | 25.56 | 188.30 | 167.31 | 11.1 |
| 14.08 | 124.32 | 121.26 | 2.4 | 26.08 | 125.75 | 121.26 | 3.6 |
| 14.60 | 194.69 | 197.15 | -1.2 | 28.69 | 99.31 | 89.04 | 10.1 |
| 15.13 | 307.26 | 294.56 | 4.1 | 29.21 | 130.41 | 135.86 | -4.2 |
| 18.78 | 109.35 | 92.74 | 15.1 | 30.78 | 135.41 | 136.97 | -1.1 |
| 19.80 | 279.88 | 257.42 | 8 | 33.47 | 191.73 | 183.10 | 9.5 |
| 20.86 | 139.71 | 128.08 | 8.3 | 40.17 | 286.41 | 271.42 | 5.2 |
| 24.00 | 127.07 | 113.26 | 11 | 43.82 | 107.08 | 96.60 | 10 |
| 24.50 | 191.09 | 177.46 | 7 | 44.34 | 140.10 | 151.59 | -8.2 |

**Initial and boundary conditions: a=2mm, t=0, G(0)=117.45 Mpa*

### 4.1.4 Experimental Analysis

Experimental tests have been performed on two typical elastometric materials. These materials possess characteristics similar to these tissues. PVDF films (Goodfellow Co. USA) have been used as the sensing elements on the grasper to obtain force and contact pressure.

Initially we designed, fabricated and calibrated an array of $25\mu$ thick uniaxially drawn PVDF sensor. PVDF films are arranged to form parallel strips of sensing elements. Four strips of uniaxially drawn metalized on both sides of PVDF films are glued onto a prototype grasper (figure (4-17)). In gluing of the PVDF films, care was taken to ensure that the strips of the films were glued uniformly with a thin layer of non-conductive glue. It is important to note that PVDF is more sensitive in the drawn direction. The piezoelectric coefficient in the drawn direction is ten times higher than that in the transverse directions. To this end, all the strips of the PVDF films were glued on the grasper in such a way that the drawn directions of the films were aligned towards the depth of the teeth. This would ensure that all of the sensing elements have the same sensitivity. The conventional axes of the PVDF films are shown in figure (4-18). More information about the piezoelectricity is explained in appendix II.

When an object is pressed onto the teeth of the grasper, the strips of sensor elements produce voltage which can be viewed in a computer monitor. Since the voltage output of a PVDF film is proportional to the applied force [81], a combination of output voltages produced by the strips of sensing elements demonstrate the force and contact pressure at various points on the contact area. Therefore, the ratio of the voltages shows the ratio of the contact forces and pressures on the specified contact areas. Since the tooth of grasper is symmetrical about the line passing through the tip, only two voltage signals that are produced by sensing areas on one side of tooth are analyzed.

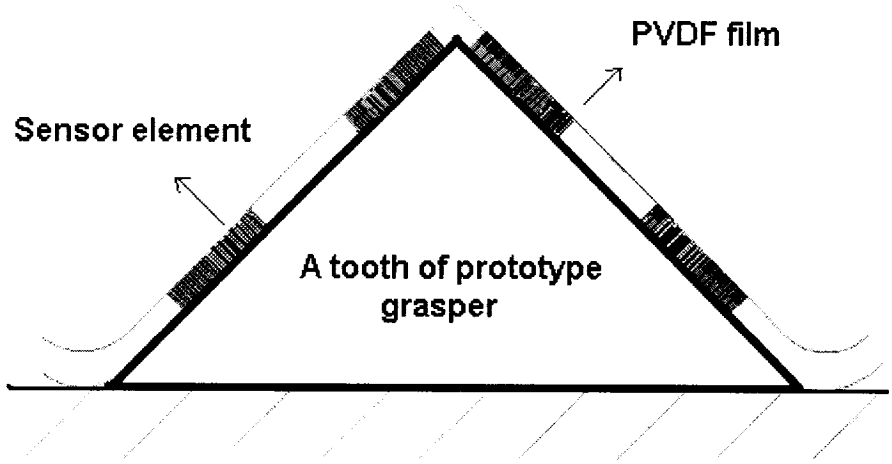


**Figure (4-17).** Schematic of four strips of PVDF film glued on a single prototype tooth.

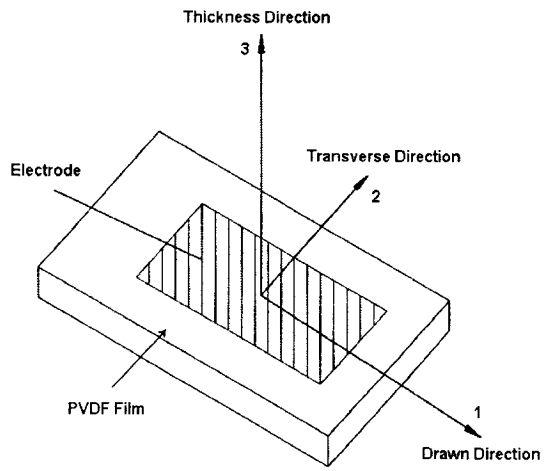


**Figure (4-18).** Schematic picture of a PVDF film showing the conventional identification of the axes. The 1, 2, 3 directions represent the drawn, transverse and thickness direction of the film, respectively.

#### 4.1.4.1 Experimental Set up

The schematic diagram of the experimental set up, developed to analyze the performance of the sensor, is shown in figure (4-19).

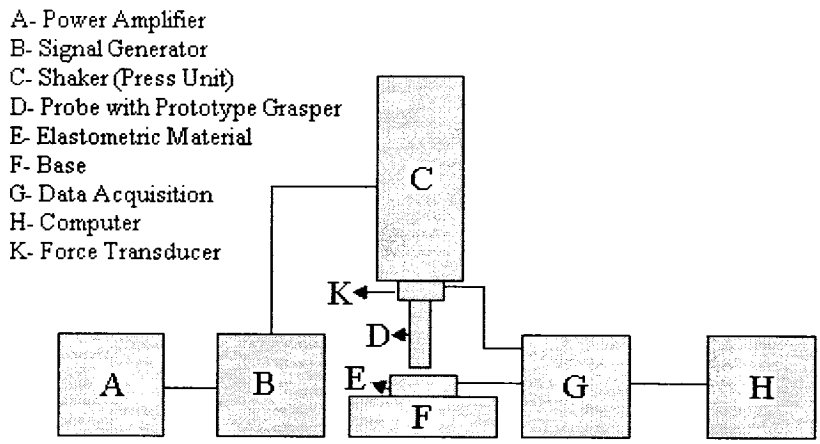


**Figure (4-19).** Block diagram of the experimental setup.

The equipment and their specifications used in the experimental set up are listed as follows:

- Dual Mode Power Amplifier: (four Pieces.) Model 504E, Kistler Instrument Corp.
  Useful Amplifier factor: 1V/lbf

- Signal Generator: Agilent 33220A
  20MHz Function/Arbitrary Waveform Generator

- V203 Shaker: made by Ling Dynamic Systems LTD. Main specification,
  Useful frequency Range: 5 ~ 13000Hz;
  Velocity sine peak: 1.49m/s;
  Amplifier rating: 0.048kVA;
  Displacement pk-pk: 5.0mm;

- Charge Amplifier: Type 2634.

Amplifier factor: 10mv/lbf

- Force Transducer: Type 9712B50, Kistler Instrument Corp.

  Sensitivity: 92.9mv/lbf;

  Measuring range: 50lbf;

  Temperature: -50~120°C.

- Prototype grasper with sensors: Aluminum bar, connected with force transducer, passing force to tactile sensor.

The complete experimental set up with all the electronic components and the display unit is shown in the figure (4-20).

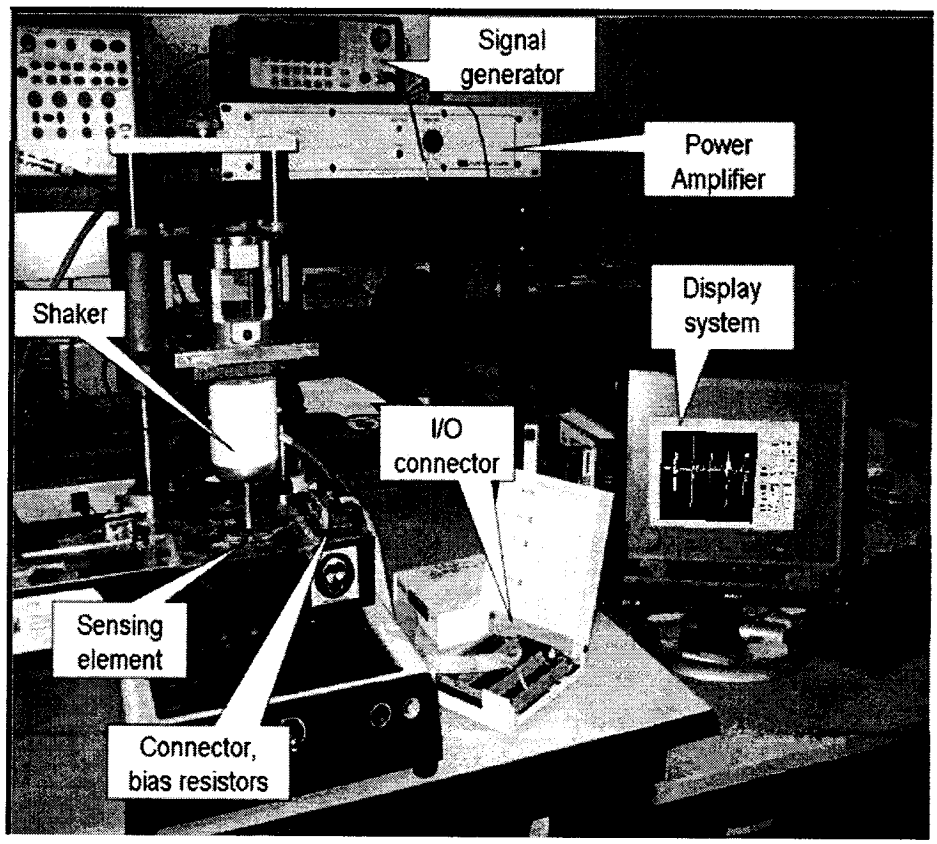


**Figure (4-20).** Experimental setup.

#### 4.1.4.2 Experiments

Figures (4-21) and (4-22) show the four teeth macro type fabricated grasper. The purpose of the tests is to find the contact pressure ratio between the two areas on single side of a tooth for four teeth of the grasper. To this end, a device with four teeth was fabricated and strips of PVDF films were glued, as shown in figure (4-17), by non-conductive glue.

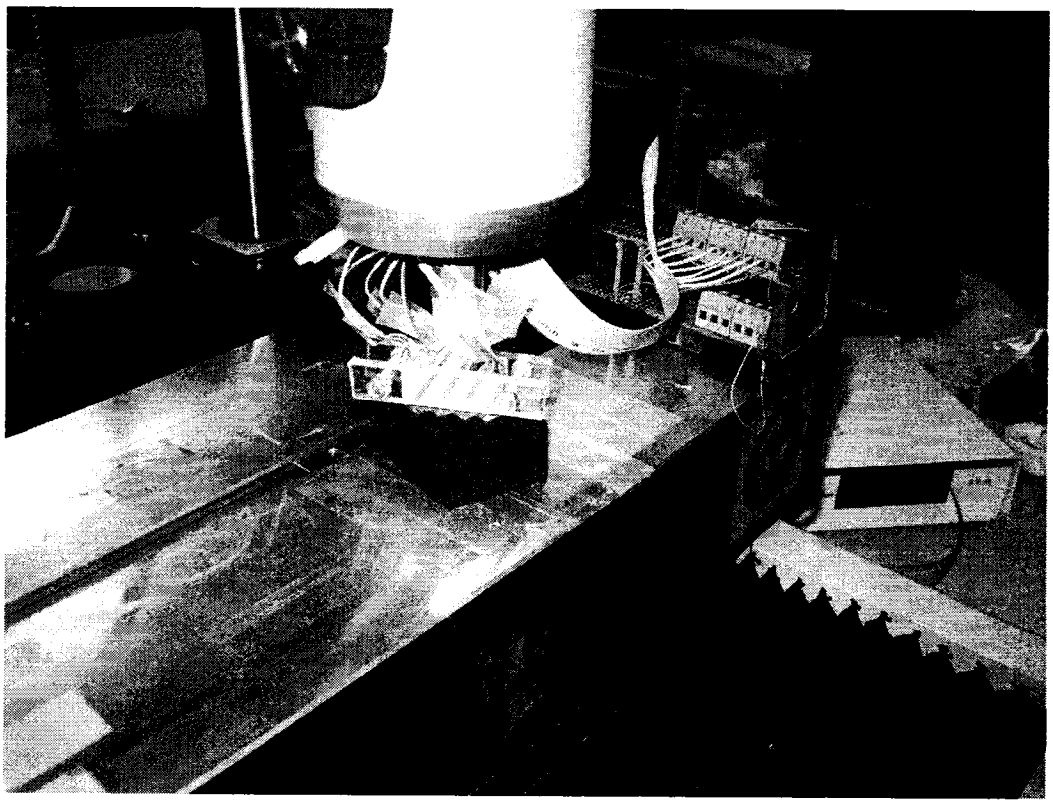

**Figure (4-21).** Macro type grasper and press unit.

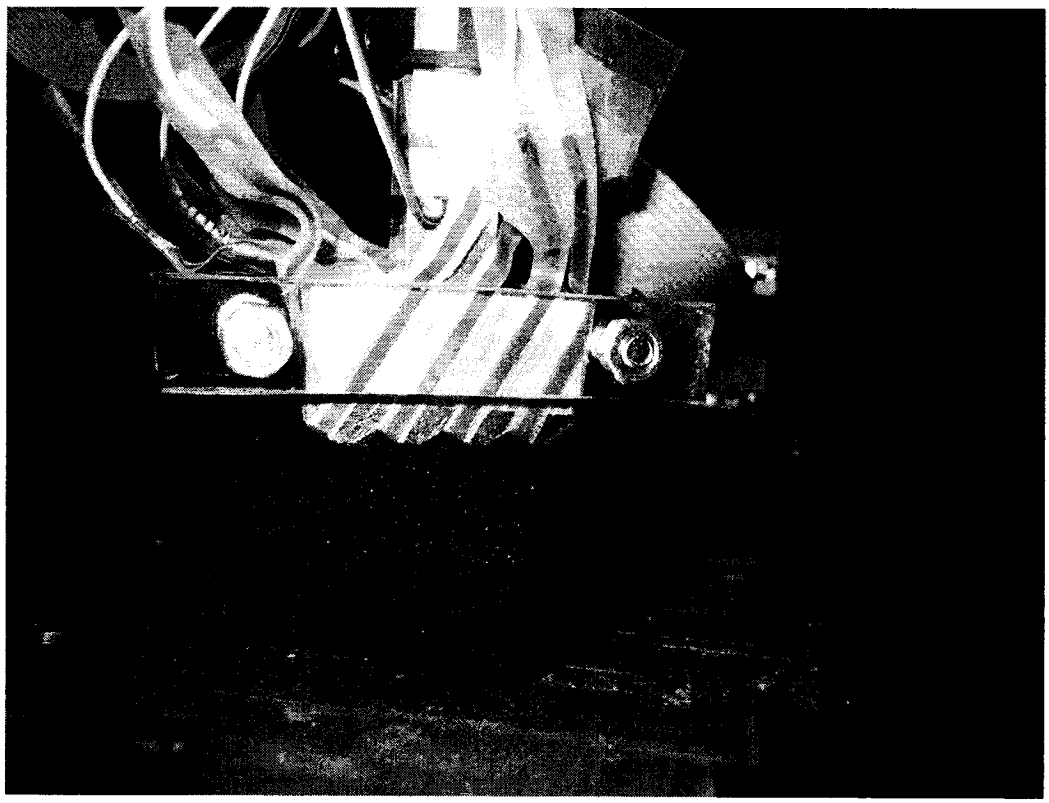

**Figure (4-22).** Macro type grasper and material.

Figures (4-23) and (4-24) show the responses of the sensors under a step loading-unloading for two different samples. The sensor outputs of Mat#1 is shown in figure (4-23) which is harder than Mat#2 whose output is shown in figure (4-24). Channels 1 to 4 are related to the sensors which are close to the tip of the teeth and channels 5 to 8 are connected to the sensors that are fixed in the lower sides of teeth. 50 Hz main frequency was superimposed on the transient signals. During the experimental analysis, this frequency was filtered.

The results obtained from the tests are shown in figures (4-23) and (4-24), respectively. It is shown that the average contact pressure ratio on the sensing areas which are closed to the tip of teeth with sensing areas on the lower sides of teeth is about two (the ratio of CH1/CH5, CH2/CH6, CH3/CH7 and CH4/CH8 are all about 2). This is the ratio that agrees with both closed form and finite element analysis results (table (4-3)). In addition, although Mat#1 is harder than Mat#2 and its peak to peak voltage values are higher, the contact pressure ratio does not differ. On the other hand, after the one second of the application of load, the contact force and pressure decrease which shows the effect of viscoelasticity of the materials.

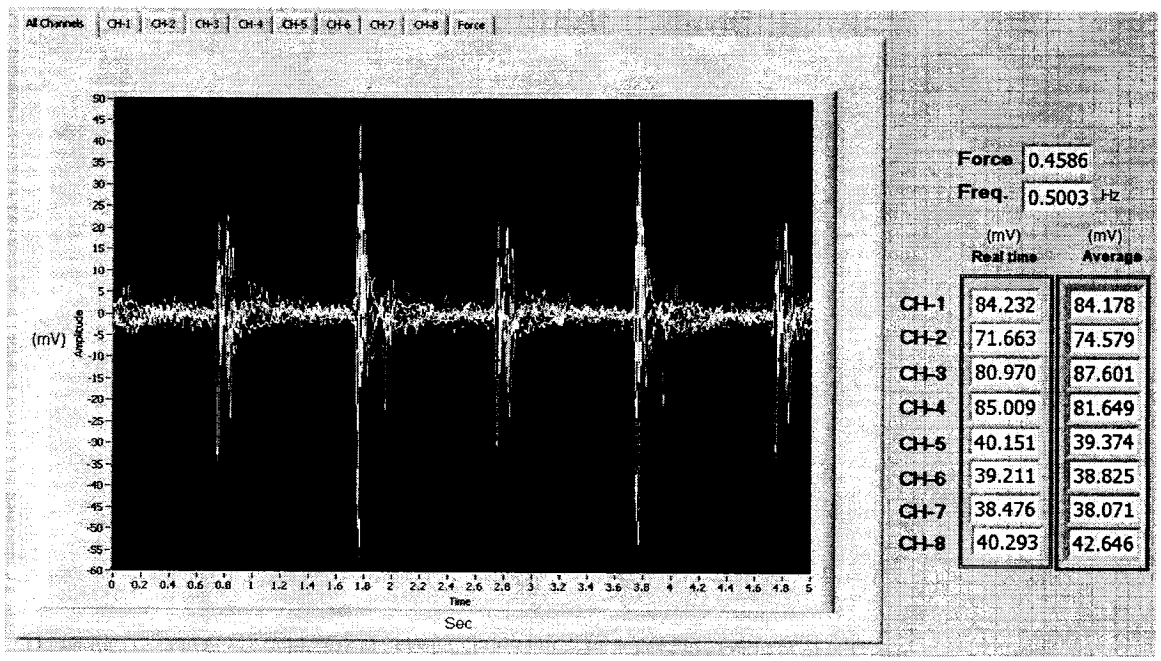


**Figure (4-23).** Sensor output under a step load for Mat#1 ($E = 32\ Mpa$).

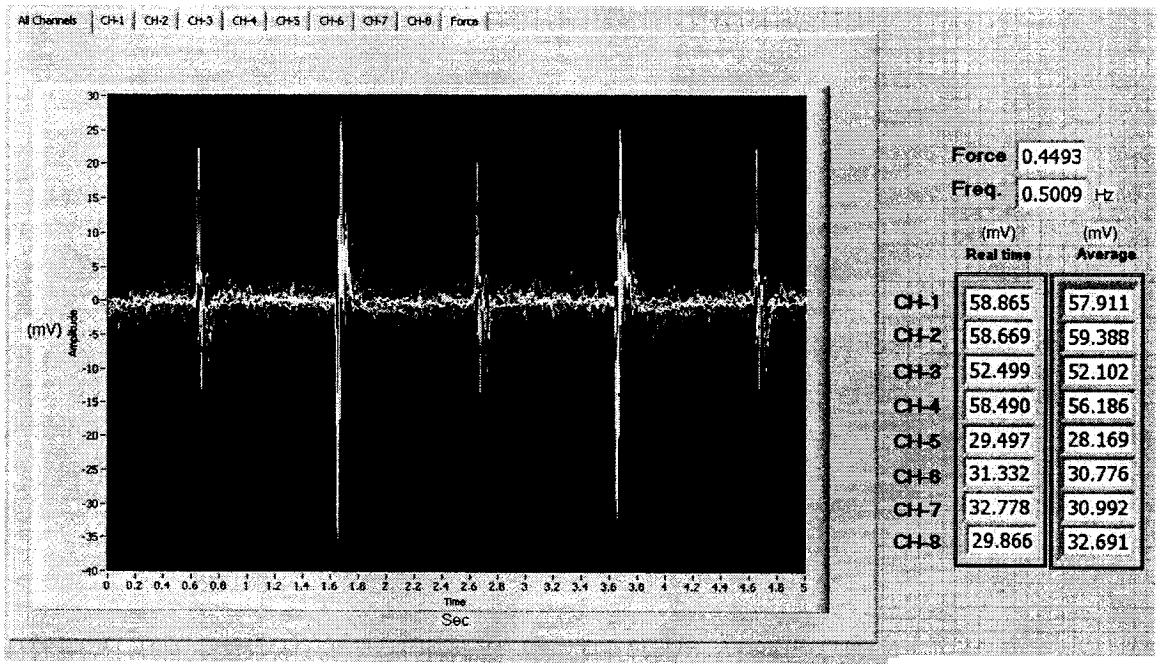


**Figure (4-24).** Sensor output under a step load for Mat#2 (*E=7 Mpa*).

**Table (4-3).** The average force ratios between the sensing areas close to tip with the lower sensing areas.

| | **Experimental** | **Closed form** | **Finite Element** |
|---|---|---|---|
| **MAT # 1** | 2.06 | 2.15 | 2.27 |
| **MAT # 2** | 1.93 | 2.17 | 2.21 |

## 4.2 Grasping Contact Analysis of Biological Tissues with Semi-Cylinderical Teeth Grasper with Applications in Minimally Invasive Surgery

### 4.2.1 Cylindrical Contact Closed Form Analysis

In this section a rigid semi-cylinder tooth with radius R, penetrating normally into the viscoelastic solid (figure 4-25) is considered to verify the effect of the shape of grasper on the contact pressure.

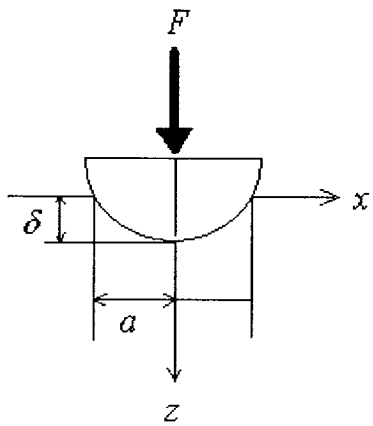


**Figure (4-25).** A rigid semi- cylinder indents to a viscoelastic solid.

The contact pressure between a rigid cylinder tooth and an elastic solid is given by Johnson [83],

$$p(x) = \frac{G}{(1-\nu)R}(a^2 - x^2)^{1/2} \tag{4-17}$$

where $G$, $\nu$ and $a$ are shear modulus, Poisson's ratio and contact area, respectively. Figure (4-26) shows the variation of the contact pressure against $x$.

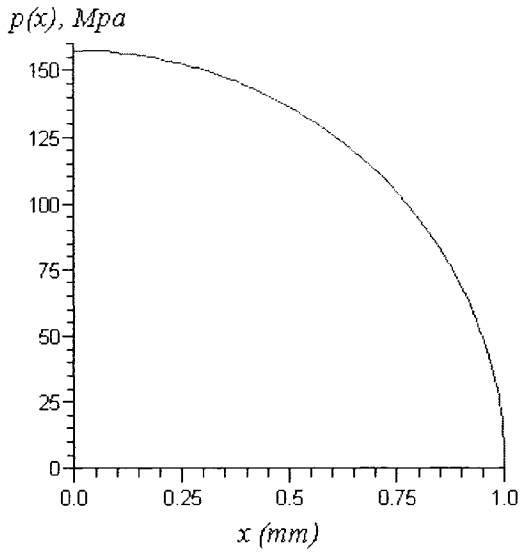


**Figure (4-26).** The variation of the contact pressure against x in elastic contact (*G=235 Gpa, a=1mm, R=3 mm, v=0.5*).

Assuming that the Poison's ratio is time independent, the relationship between contact pressure and contact area for a viscoelastic contact is given by:

$$p(x,t) = \frac{1}{(1-\nu)R} \int_0 G(t-t') \frac{d}{dt'} (a^2 - x^2)^{1/2} dt' \qquad (4\text{-}18)$$

In the following, we assume that Poisson's ratio is time independent. In addition, the viscoelastic material is assumed to be incompressible and so, *B(t)* tends to go to infinity and its stress-strain relation is expressed in terms of single function describing its behavior in shear. This approximation is reasonable for tissues and polymers, whose values of Poisson's ratio usually exceed 0.4. Therefore, for a time independent values of *a* equation (3-18) is reduced to the following expression,

$$p(x,t) = \frac{2}{R} G(t)(a^2 - x^2)^{1/2} \tag{4-19}$$

For an elastic material, the relationship between contact area $a$ and force, $F$ is given by the following equation,

$$F = \int_a^a p(x)dx = \frac{\pi a^2 G}{2(1-\upsilon)R} \tag{4-20}$$

where $p(x)$ is substituted from equation (4-17) in the integral and $F$ is force per unit length.

Equation (4-20) can also be written as,

$$a = \left( \frac{2(1-\nu)RF}{\pi G} \right)^{1/2} \tag{4-21}$$

Since we assumed that the viscoelastic material is considered incompressible, Equation (4-20) can be written as,

$$F(t) = \frac{\pi}{R} \int_0 G(t-t') \left( \frac{da^2(t')}{dt'} \right) dt' \tag{4-22}$$

Under a constant value of contact area, $F(t)$ becomes,

$$F(t) = \frac{\pi G(t) a^2}{R} \tag{4-23}$$

Inversely, under a constant value of total load, $a(t)$ is expressed as,

$$a(t) = \left( \frac{RF}{\pi} J(t) \right)^{1/2} \tag{4-24}$$

By taking the delayed elasticity material, equations (4-25), (4-26) and (4-27) are expressed, respectively, as,

$$p(x,t) = \frac{g_1[g_2 + g_1 \exp(-t/T_2)]}{(g_1 + g_2)R}(a^2 - x^2)^{1/2} \tag{4-25}$$

$$F(t) = \frac{\pi g_1[g_2 + g_1 \exp(-t/T_2)]a^2}{2(g_1 + g_2)R} \tag{4-26}$$

$$a(t) = \left\{\frac{2RF}{\pi}[\frac{1}{g_1} + \frac{1}{g_2}(1 - \exp(-t/T_1)]\right\}^{1/2} \tag{4-27}$$

Figure (4-27) shows the changes of contact pressure against time and location. It is seen that at the constant value of the strain, the contact pressure decreases monotonically and goes to a constant value, which is stable situation.

Figure (4-28) shows the decreasing of the force along the time under a constant contact area situation. As shown in fig (4-29), with increasing contact area, the total load increases significantly and decrease along the time rapidly.

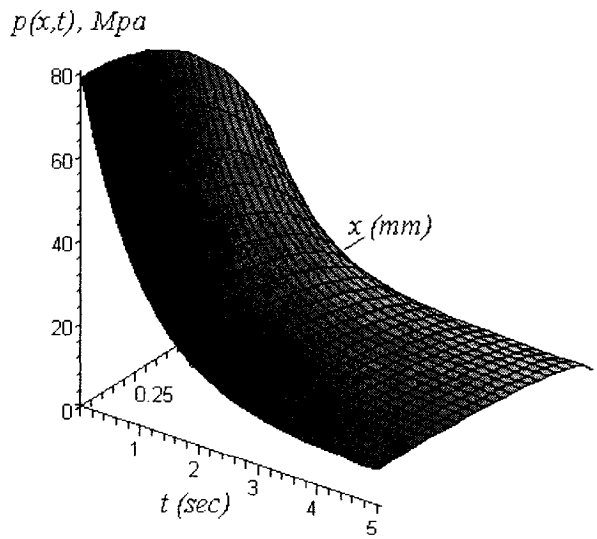


**Figure (4-27).** Variation of contact pressure in delayed elasticity material against time and location in viscoelastic contact ($g_1$ = *235 Mpa*, $g_2$= *26 Mpa*, *R=3mm*, $T_2$=*1 sec*, *a=1mm*).

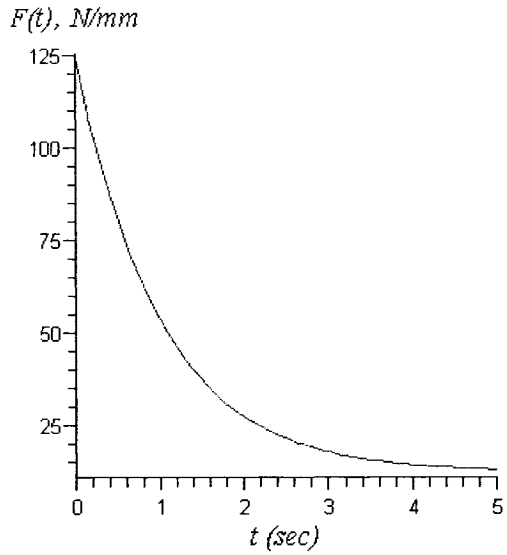


**Figure (4-28).** Variation of total force per mm against time ($g_1$ = *235 Mpa*, $g_2$= *26 Mpa*, *R=3mm*, $T_2$=*1 sec*, *a=1mm*).

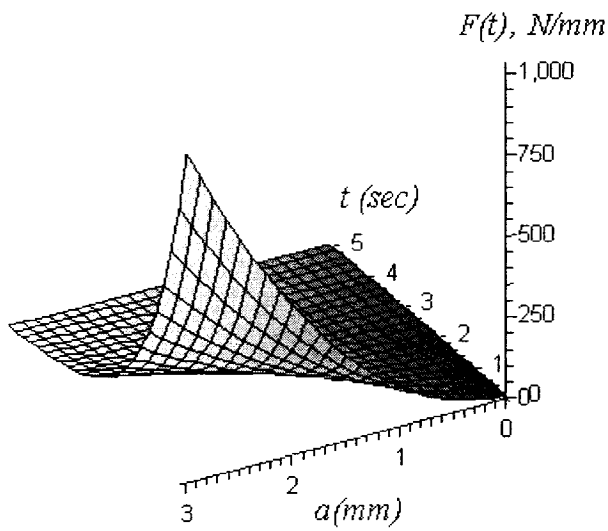


**Figure (4-29).** Variation of total Force per mm against time in various magnitudes of contact area ($g_1$ = *235 Mpa*, $g_2$= *26 Mpa*, *R=3mm*, $T_2$=*1 sec*, *a=1mm*).

Figures (4-30) shows the increase of contact area under a constant value of force along the time. This is a critical situation in MIS and can damage the tissues. We will discuss this issue in the next section.

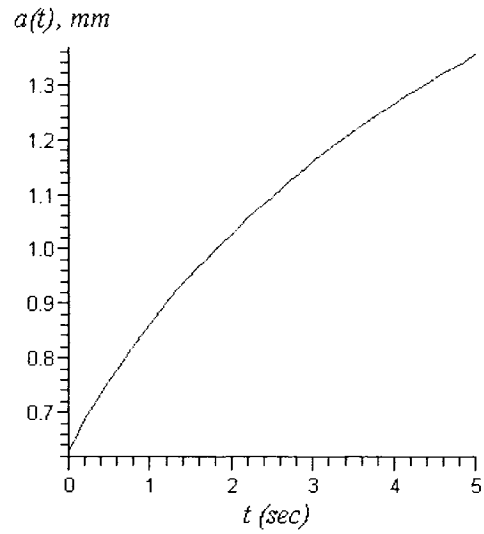


**Figure (4-30).** Increase of contact area in delayed elasticity material under a constant value of force along the time ($T_1$=*10, F=50 N/mm,* $g_1$ = *235 Mpa,* $g_2$= *26 Mpa, R=3mm*).

If Maxwell solid is considered, the contact pressure and area are given by,

$$p(x,t) = \frac{g[\exp(-t/T)]}{R}(a^2 - x^2)^{1/2} \tag{4-28}$$

$$F(t) = \frac{\pi g[\exp(-t/T)]a^2}{2R} \tag{4-29}$$

As seen in figure (4-31), the changes of the contact pressure is very fast along the time and pressure tends to go to zero for a constant $a$.

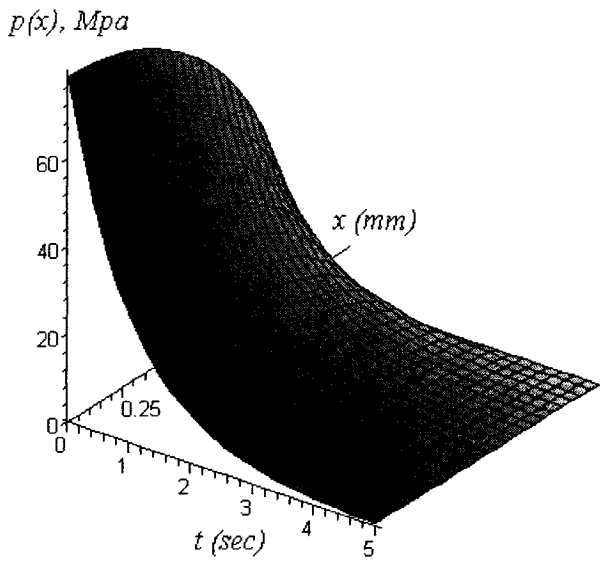


**Figure (4-31).** Change of contact pressure in Maxwell material against time and location in viscoelastic contact (*T=1(s), g = 235 Mpa, R=3mm, a=1mm*).

### 4.2.2 Grasping contact analysis

Considering figure (4-32) which shows the schematic picture of grasper and equation (4-26), the grasping contact force per unit length on the top of the delayed elasticity material for constant indentation area can be written as,

$$F(t)=\frac{g_1[g_2+g_1\exp(-t/T_2)]}{(g_1+g_2)}[\int_a(a^2-x^2)^{1/2}dx+\int_{\Delta-a}^{\Delta+a}(a^2-x^2)^{1/2}dx+\int_{\Delta-a}^{2\Delta+a}(a^2-x^2)^{1/2}dx+\cdots] \quad (4\text{-}30)$$

or,

$$F(t)=\frac{\pi N g_1[g_2+g_1\exp(-t/T_2)]a^2}{2(g_1+g_2)R} \quad (4\text{-}31)$$

where $N$ is the number of the teeth of the grasper.

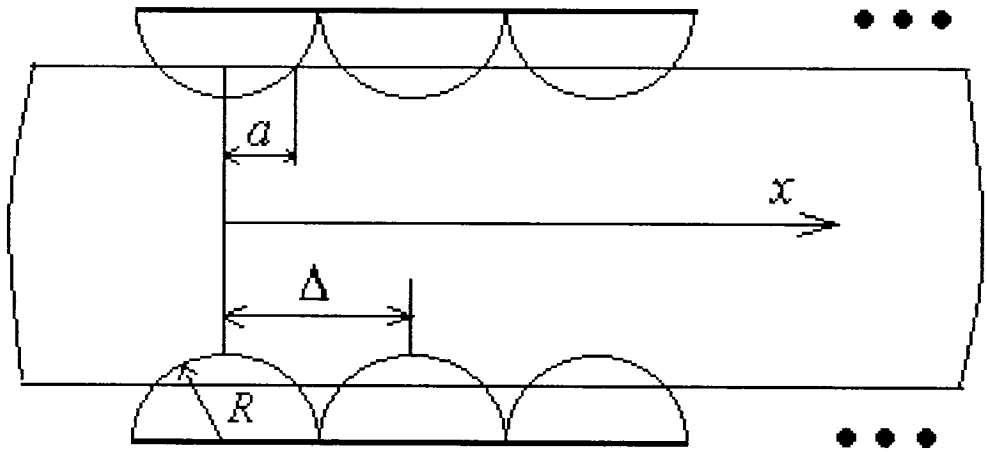


**Figure (4-32).** A schematic picture of grasper.

Considering equation (4-27) for a constant indenting load, the creep of the contact area would be,

$$a(t) = \left\{ \frac{2RF}{\pi N} [\frac{1}{g_1} + \frac{1}{g_2}(1 - \exp(-t/T_1)] \right\}^{1/2} \tag{4-32}$$

As it is shows in figure (4-33), increasing both force and time cause the increase of contact area. In MIS when a surgeon uses the graspers, it is imperative to understand that contact area and consequently contact depth will increase under a constant load. Otherwise, there is a possibility of causing damage to the organs.

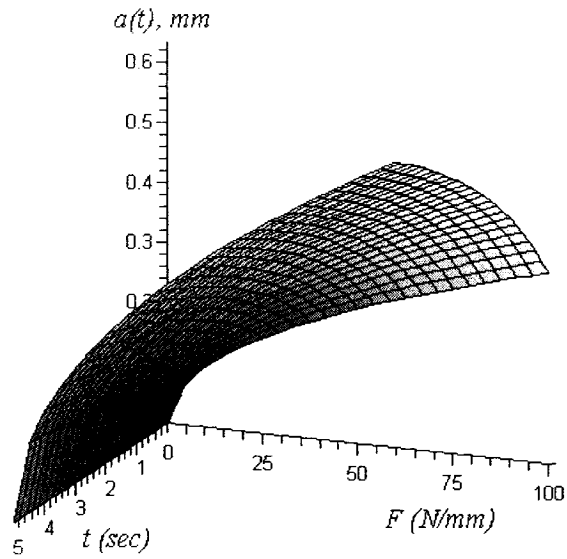


**Figure (4-33).** Increase of contact area in delayed elasticity material against force and time with a given values: $T_1=10$, $g_1 = 235$ *Mpa*, $g_2= 26$ *Mpa*, $R=3$*mm*, *number of the teeth: 8.*

### 4.2.3 Finite Element Analysis

A comprehensive numerical analysis has been done using of Ansys 10. A viscoelastic Plane-182 element has been considered for the model. This element is the most suitable choice for viscoelastic materials in two dimensions.

The semi-grasper-tissue model and boundary conditions are shown in the figure (4-34). Because of the symmetry, tissue has been fixed at the bottom. A uniformly distributed force has been applied to the grasper on one side.

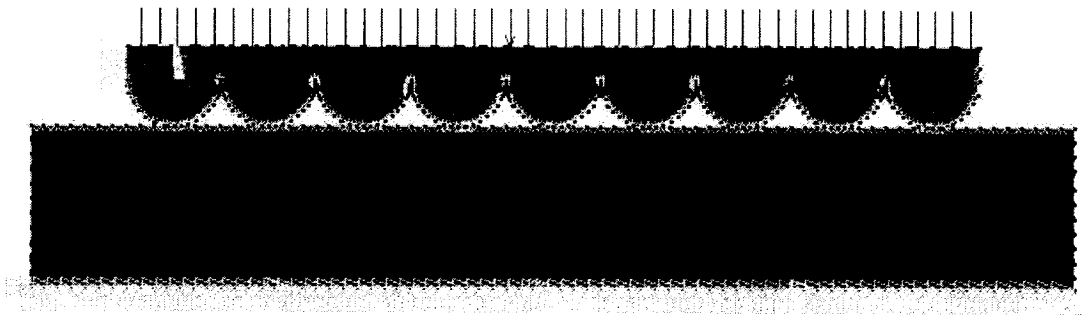

**Figure (4-34).** Ansys semi-model for tissue/grasper, meshing and loading (*tip-to-tip distance of the teeth: 6 mm, thickness of the tissue: 20 mm*).

The material properties are listed in table (4-4). Those properties are obtained from the delayed elasticity equation (3-12).

**Table (4-4).** Time dependent shear modulus.

| *t (sec)* | 0 | 1 | 2 | 3 | 4 | 5 |
|---|---|---|---|---|---|---|
| *G(t)* *Mpa* | 117.45 | 50.87 | 26.21 | 17.07 | 13.70 | 12.44 |

When the teeth of the grasper are indented into the tissue, stresses in *x, y* (normal stresses), *y-x* directions (shear stress) and deformation of the tissue are obtained and shown in figures (4-35) to (4-38).

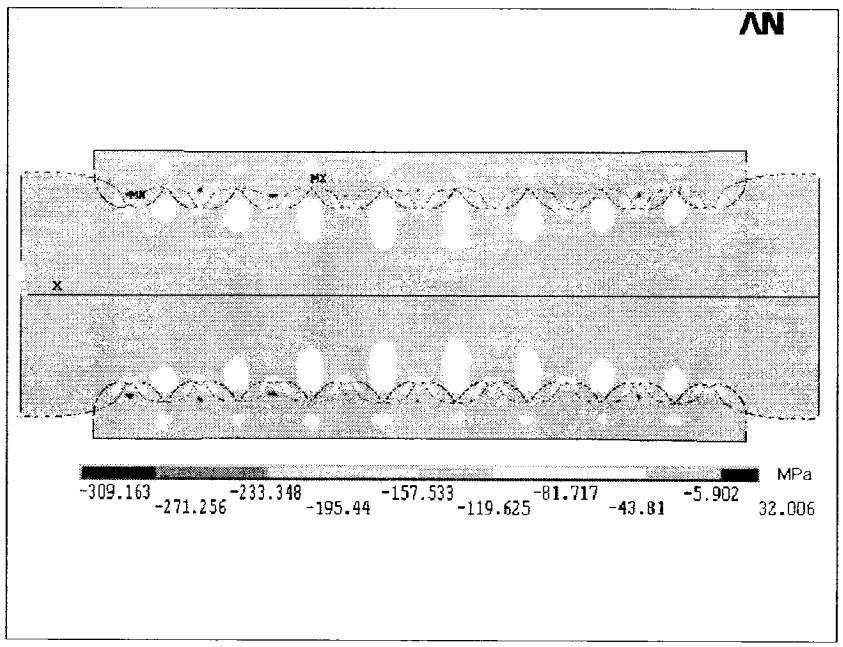


**Figure (4-35).** Normal stress in x-axis.

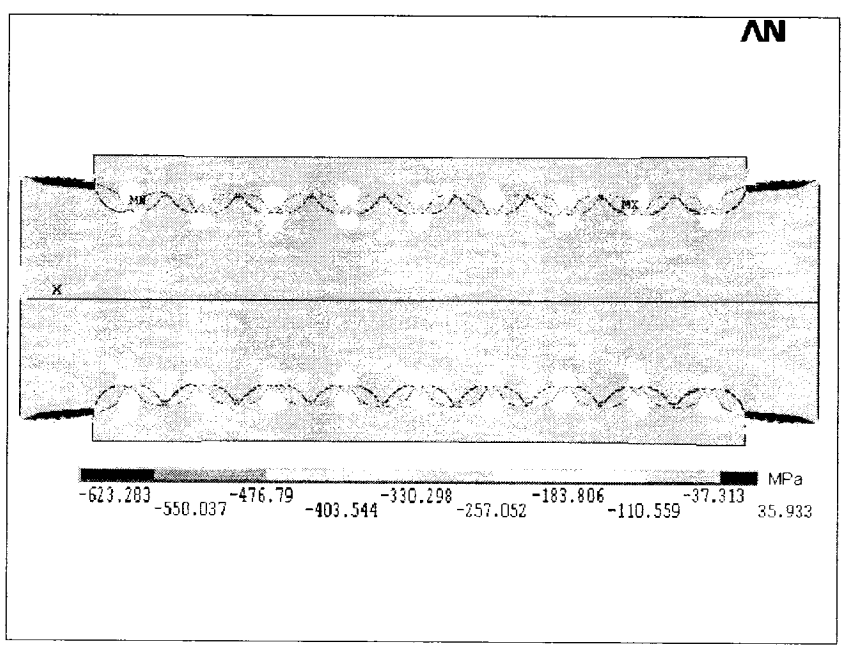


**Figure(4-36).** Normal stress in y-axis.

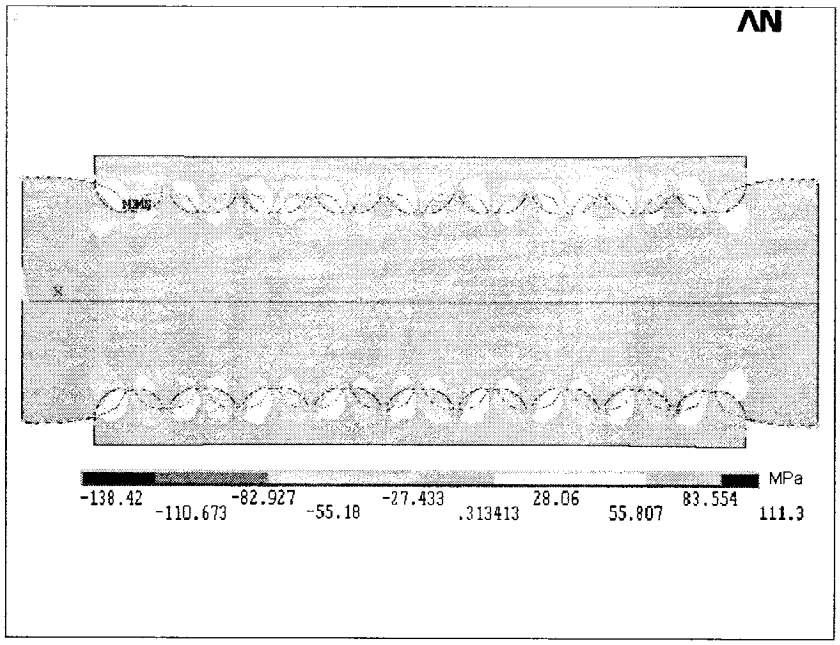


**Figure (4-37).** Shear stress in xy-axis.

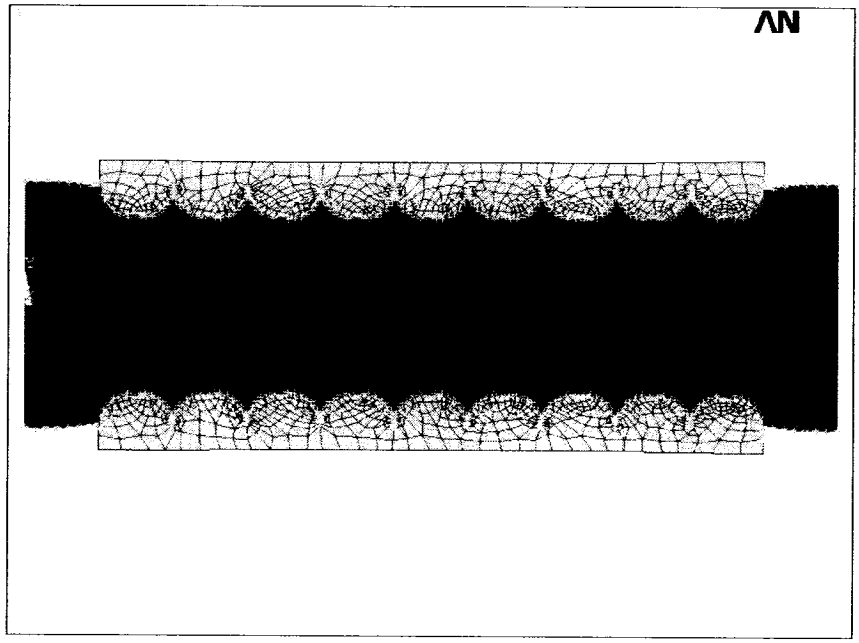


**Figure (4-38).** Deflection of the tissue.

Using equation (4-14) for 2-dimension space, pressure in the contact surfaces can be obtained by the following equation,

$$p(x,t) = \sigma_x(x,t)\cos^2\theta + 2\sigma_{xy}(x,t)\cos\theta\sin\theta + \sigma_y(x,t)\sin^2\theta \quad (4\text{-}33)$$

where, $\sigma_x$ , $\sigma_y$ and $\sigma_{xy}$ are normal shear stresses, respectively, and $\theta$ denotes the angle of normal to the contact surface with $x$ axis. The magnitudes of contact pressure under the same loading and situation of the analytical part for some arbitrary points are outlined in the table (4-5). It seen that the error range from 4%-16% with reasonable agreement exists in the values of contact pressure obtained from FEA and closed form solution.

**Table (4-5).** Comparison of contact pressures by finite element and closed form analysis*

| $x$ (mm) | Numerical $P(x)$, MPa | Analytical $P(x)$, MPa | Difference (%) |
|---|---|---|---|
| 6.45 | 94.818 | 112.04 | 16 |
| 7.30 | 57.010 | 58.59 | 2.7 |
| 12.45 | 96.136 | 112.04 | 14.2 |
| 13.30 | 56.486 | 58.59 | 4 |
| 16.74 | 55.656 | 62.49 | 10.5 |
| 25.31 | 54.830 | 58.58 | 6.4 |
| 28.74 | 58.399 | 62.49 | 5.6 |
| 31.31 | 53.135 | 58.58 | 9,3 |
| 34.74 | 58.948 | 62.49 | 5.5 |
| 35.59 | 96.411 | 112.97 | 13.9 |
| 37.31 | 50.915 | 58.58 | 13.1 |

**Initial and boundary conditions: a=2mm, t=0, G (0) =117.45 MPa.*

### 4.3 Discussion and conclusions

The closed form analysis provides relations between total force, contact area, and relaxation and creep modulus for linear viscoelastic grasping contact with both corrugated wedge-like and semi-cylinder profile. Comparison of the finite element results with those closed form analysis shows that the assumption that the contact stresses are close to the contact area, is correct. Therefore, we could use the superposition principle for the closed form grasping analysis. In addition, the finite element results agree with the results of the closed form analysis at different times during application of the load.

The study shows that under a constant load the contact area increases exponentially. Thus, fast unloading is essential for preventing any damage to tissues especially when the endurance pressure is applied to the tissues. On the other hand, the total force applied to the grasper decreases with time for a constant contact area. Another result of this study is that by increasing the number of the teeth, the rate of change of contact area reduces. In other words, to prevent any possible damage to the tissue, the number of the teeth must be increased. The experimental analysis is done to support the closed form and FEA results. The results of this study enable the surgeons to be aware of the contact force and pressure that is applied to the tissues, thus preventing any damage to tissues during the surgery. Finally, comparing the results, between those for wedge teeth and semi-cylindrical teeth it is seen that that semi-cylindrical teeth will reduce tissue damage unlike the triangular teeth.

Next chapter will discuss the design, analysis and fabrication of the tactile sensor in order to determine the properties and particularly the compliance of the biological tissues during minimally invasive surgery.

# CHAPTER 5

# DESIGN AND FABRICATION OF A TACTILE SENSOR FOR CHARACTERIZATION OF BIOLOGICAL TISSUES

In this chapter, we present the design, analysis, fabrication and assembly of four tooth microfabricated tactile sensors integrated with the upper and lower jaws of an endoscopic surgical grasper tool, in order to determine the properties and particularly the compliance of the biological tissues during minimally invasive surgery. Two viscoelastic Kelvin-Voight and Kelvin models are employed for tissue characterization. A comprehensive closed form and finite element analysis have been carried out to express the relationship between the force ratio, compliance and the equivalent viscous damping of the tissue. The designed sensor uses a PVDF film as its sensing element. The sensor consists of arrays of rigid and compliant elements which are mounted on the tip of an endoscopic surgical grasper tool. Relative force between adjacent parts of the contact object is used to measure the viscoelastic properties.

## 5.1 Sensor design

The sensor structure consists of an array of four individual sensors on both sides of an endoscopic grasper jaw for measuring the compliance of the objects between them. The sensor structure consists of four different parts, as shown in the figures (5-1) and (5-2), namely rigid and the compliant cylinders, the sensing element and the substrate. The rigid cylinder is machined from Plexiglas 3mm in diameter and 1mm thick. The purpose of the rigid cylinder is dual. It not only acts as major sensing element but also increases the friction between the grasper and the sensed object. The second cylinder is the compliant cylinder which surrounds the rigid cylinder. The compliant ring shaped cylinder is

micromolded from liquid silicone rubber. For the demonstration purposes, the outer diameter of the compliant cylinder is 6 mm and the inner diameter is 4 mm. The thickness of the cylinders is 1 mm. Due to fabrication limitations, a gap of 0.5 mm is used between the rigid and the compliant cylinders. This gap can be reduced further to a negligible amount with more precise fabrication process.

A 25 μm bi-axially oriented, metalized and poled PVDF film is sandwiched between the cylinders and the substrate. It has piezoelectric strain coefficients of $d_{31}$, $d_{32}$ and $d_{33}$ of 20, 2 and -20 pC/N, respectively, and is used as the sensing element [28-30]. The PVDF film contains patterned aluminum electrodes right underneath the rigid and the soft cylinders. The patterned PVDF films are glued to a 0.5 mm thick Silicon substrate. The output charges from both the PVDF are fed to data acquisition system through electrical connections.

One of the important advantages of this design is the thermal insulation provided to the PVDF films by the rigid and the compliant cylinders. Due to this when the grasper is in contact with different objects at different temperatures there are no spurious output and hence the pyroelectric effect is not a problem in this specified design. During the actual testing, the object is assumed to have viscoelastic behavior.

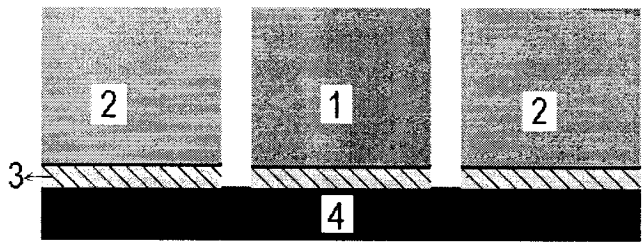


1- Rigid cylinder
2- Compliant cylinder
3- PVDF
4- Si substrate

**Figure (5-1).** Cross sectional view of the sensor.

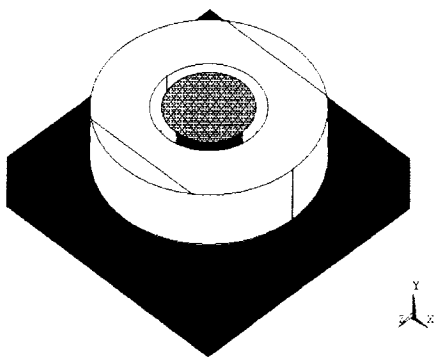

**Figure (5-2).** Isometric view of the sensor.

### 5.1.1 Design of Base Substrate

Sensor design consists of a square base plate. It is made up of copper. The modulus of the copper lies between the 50 *GPa* to 100 *GPa*. In our analysis we used 70 *GPa* and Poisson ratio of 0.3. The base plate has size of the 6 x 6 x 0.5 *mm*. The properties of the plate material are as given in table (5-1). The schematic diagram of the plates is shown in the figure (5-3).

**Table (5-1)**. The properties of the copper.

| Properties of Copper used as base plate for sensor | |
|---|---|
| Young's Modulus | 70 *GPa* |
| Density | 1190 $Kg/m^3$ |
| Poisson Ratio | 0.3 |
| Dimension of Plate | 6 x 6 x 0.5 *mm* |

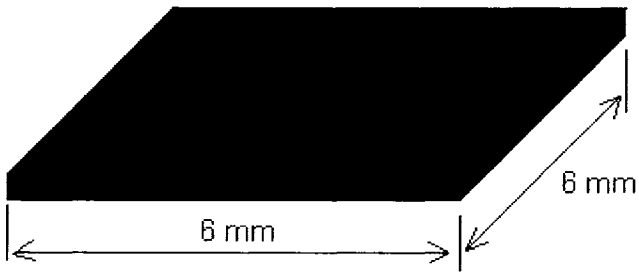


**Figure (5-3).** Design of base plate for the Sensor.

### 5.1.2 Design of PVDF Films

Piezoelectric substances are new materials used for sensors and actuators with the help of microelectromechanical systems technology. When external force is applied to piezo-materials, it generates charge on the surface, which is proportional to applied mechanical force. The converse effect is also there, where applied voltage generates deformation in the materials. Piezoelectricity relates to the crystalline ionic structure. PVDF films in shape of circular cross section are used for measuring the force on the rigid cylinder and soft cylinder of the sensor. Circular and ring shaped PVDF films are under the rigid and the soft cylinder, respectively, and are named as PVDF-1 and PVDF-2, respectively. The design of the PVDF-1 and PVDF-2 are discussed below.

A single layer of PVDF film was taken and was patterned using lithography process according to the required design and dimension. The PVDF-1, which is circular with 3mm diameter, is sandwiched between the base plate and the rigid cylinder. This PVDF-1 film measures the force acting on the rigid cylinder.

The other PVDF film is in the shape of a ring with inner radius of 2 mm and outer radius of 3mm. Both the PVDF films have the same material properties. PVDF-2 film is sandwiched between the soft cylinder and base plate. This PVDF film measures force on the outer soft cylinder. Both the rigid and the soft cylinders are attached to the PVDF using non-conductive glue.

PVDF film is anisotropic in nature. Film used in the sensor is polarized in '$Z$' direction, as shown in figure (5-4), and the charge developed is taken from two electrodes on the face of the aluminium of the PVDF film. During the analysis of the forces, it was

assumed that there was no shear forces in the sensor and only $Z$ direction force and deformation was taken into account.

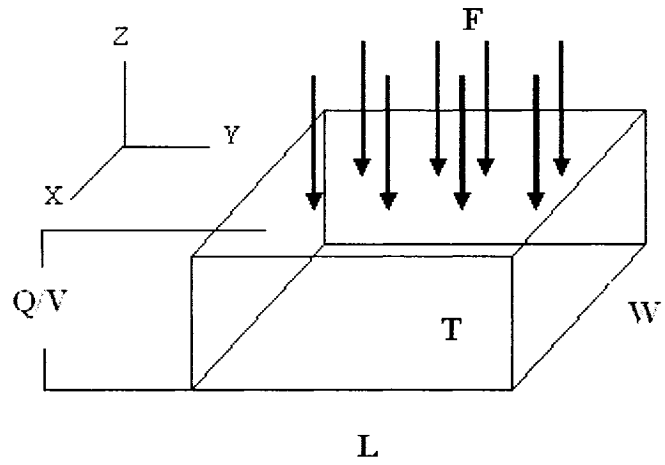


**Figure (5-4).** Polarization of a PVDF film.

PVDF-2 was used as sensing element under the compliant cylinder. For defining the properties of PVDF we have to concentrate on its structural and electric behavior. Four parameters are required for analysis of the piezoelectric behavior, i.e. density, anisotropic array, permittivity and piezoelectric matrix. These parameters are supplied by the manufacturer. All the parameters PVDF film are defined in the Appendix II under piezoelectricity.

### 5.1.3 Rigid Cylinder Design

The rigid cylinder is made of high pressure plexiglass. The plexiglass polymer was used as rigid cylinder because of its non conductive nature with good rigidness. It has good mechanical properties, with a modulus of elasticity of $70GPa$ and Poisson's ratio of 0.3. The electrical resistivity offered by the rigid cylinder is quite high. This rigid part of the cylinder acts as the teeth in sensor. When the force is applied on the sensor, the compliant cylinder experiences more compression as compared to the rigid cylinder. As a result of

this compression the rigid part protrudes relative to the compliant part. This provides the gripping effect to the tissue. The diameter, D of the cylinder is 3mm and height of cylinder, $T_2$ (or $T_3$ in section 5.3.2) is 1 mm and shown in figure (5-5).

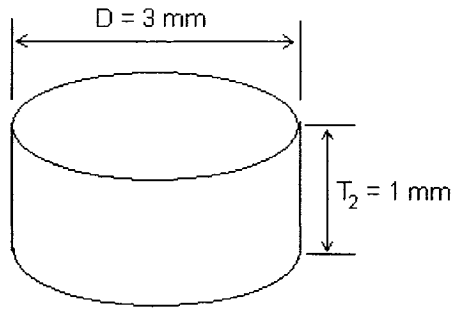


**Figure(5-5).** Rigid cylinder made up of Plexiglass Size: *R1.5 mm ×1 mm.*

### 5.1.4 Compliant Cylinder Design

The rigid cylinder is surrounded by the compliant cylinder. The size of the compliant cylinder is $R_1 = 2\ mm$, $R_2 = 3mm$ and height of the cylinder is 1mm as shown in figure (5-6). The rubber material used for this cylinder is Liquid Silicone Rubber (LSR) sylgard 184 purchased from Dow Corning with modulus of elasticity 7.1*MPa*.

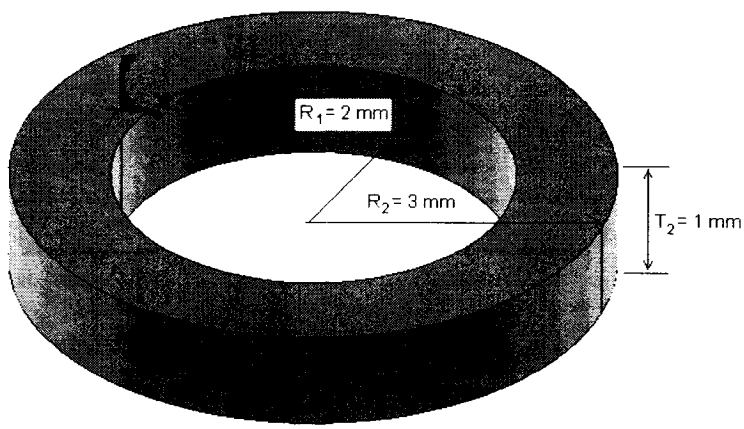


**Figure (5-6).** Compliant cylinder is made up of soft rubber.

### 5.1.5 Sensed Object Design

As discussed in chapter 4, tissue behaves like a viscoelastic material. Viscous behavior makes tissue to change its deflection and stress with time. This behavior is not considered in our experimental study. The tissue is considered as rubber specimen with different modulus of elasticity. The Modulus of Elasticity, range of samples used varies from 10MPa to 200MPa. The size of sample is kept similar to the base plate size. The thickness is varied for different samples and similarly the length is varied.

## 5.2 Four Sensor Design

The single sensor used for study will not serve the purpose of the endoscope grasper mounting. Endoscope grasper required number of small micro machined tactile sensors mounted in the form of an array. In practical application on the endoscope grasper, these sensors could be from 4 to 6 in a regular array pattern. Even though, there could be different arrangements for assembling the sensor on the endoscope, we limited our approach and focus on only one type of sensor designs.

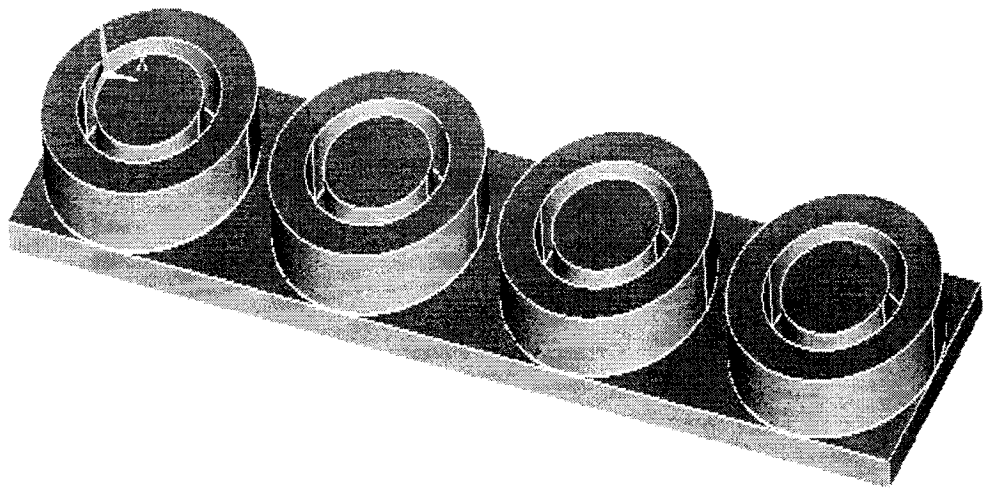

**Figure (5-7).** Array of sensor on a common base.

Figure(5-7) shows the arrangement of four sensors on a substrate. In this design, we have a common substrate for all the four sensors and it is integrated to the grasper jaw with a help of a dovetail fix that will slide into the grasper teeth. In total there are eight sensors combining both sets of teeth. The object is grasped by both jaws with the sensors and the output from the eight sensors is fed to the data acquisition system and is calibrated to visualize the softness of the different objects being grasped. Once the objects are tested by the sensors, the dovetail fix can be conveniently removed from the grasper teeth. The following figures will display the technical details of the grasper design as well as the dovetail fix.

The base plate used for the array of sensor changes in dimension. The dimensions of the base plate are 40X10X0.5 mm. A fixture of the required dimension is machined and the

copper substrates along with the sensor are mounted to the endoscopic grasper. Figure (5-8) gives the complete details of the endoscopic grasper mounting and also its isometric view with the sensors.

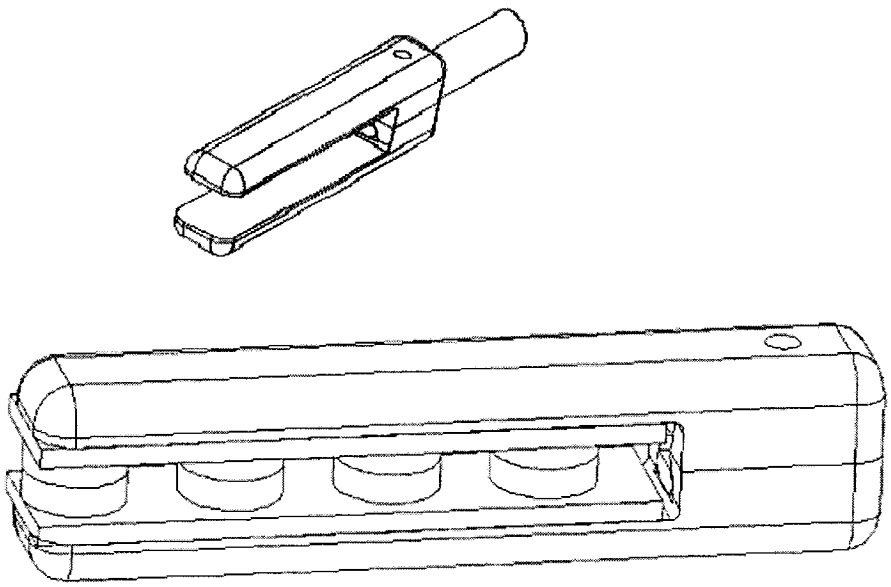

**Figure (5-8).** AutoCAD drawing of endoscope grasper mounting with the sensors

### 5.3 Sensor analysis

In the following analysis, two well known viscoelastic models, namely, Kelvin-Voight and Kelvin [88] are employed to define the behavior of tissue. We analyzed the sensor with two models to verify how the models can affect the results.

#### 5.3.1 Kelvin-Voight Model

This model includes a spring of modulus $g$ parallel to a dashpot of an equivalent viscous damping coefficient $c$. For Kelvin-Voight model the constitutive equation is expressed as,

$$c\dot{e}(t) + ge(t) = s_0 \tag{5-1}$$

The creep response to a step change in stress $s_0$ is given by,

$$e(t) = 0.5J_1(t)s_0 = \frac{1}{g}(1 + \exp(-t/T)s_0 \tag{5-2}$$

where $T = g/c$

Figure (5-9) shows the proposed model. As seen in this figure the viscoelastic object is pressed to the sensor with known force, a part of which flows through the rigid cylinder and the rest through a compliant cylinder in the sensor. For simplicity, the annular gap between the cylinders is neglected and load is assumed to be uniformly distributed throughout. In this way the parts of the object in contact with each element of the sensor are deformed to different extents.

In the following $E_1$ is Young's modulus and $c$ is the viscous damping coefficient per unit area of the object and $E_2$ is Young's modulus of the compliant cylinder. In addition, it is assumed that the viscoelastic object can not take any bending load and hence the rigid cylinder experiences the load applied on the viscoelastic object just above it only. The same assumption holds good for the compliant cylinder.

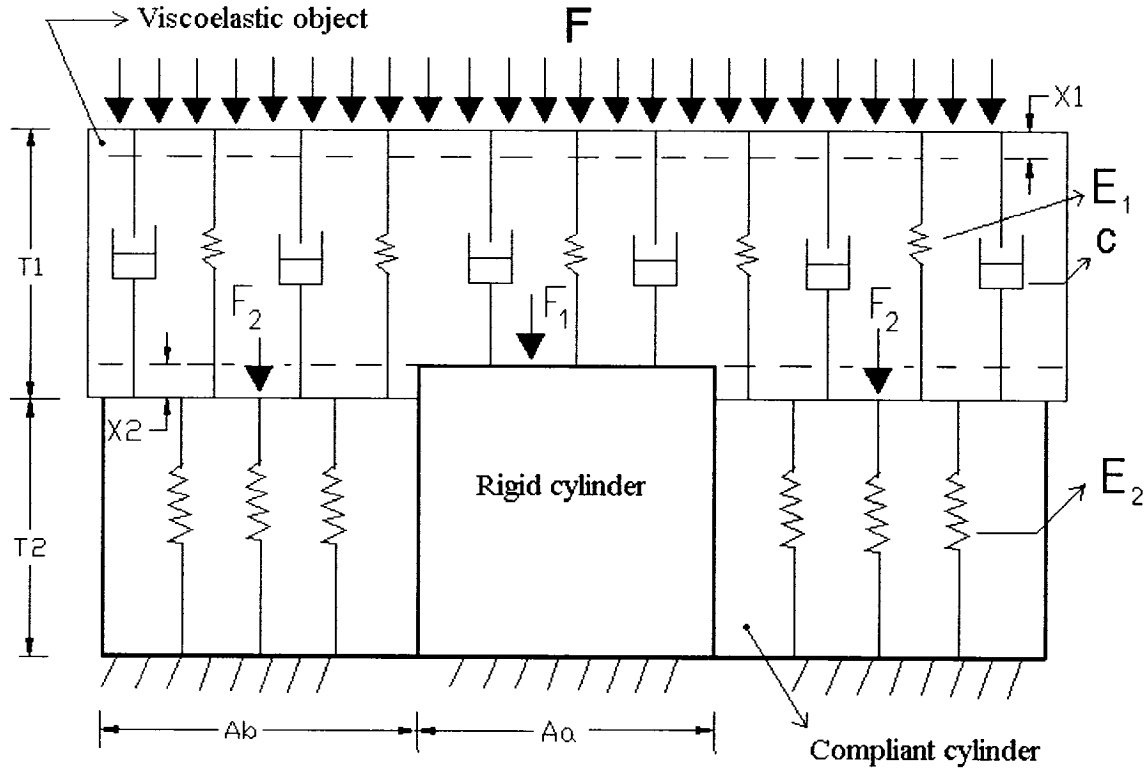


**Figure (5-9).** Analytical model of sensor-object configuration.*

* *Definition of the Notations:* $A_a$*: Area of the rigid cylinder,* $A_b$*: Area of the compliant cylinder,* $T_1, E_1$ *: Thickness and Young's modulus of the modeled object under investigation,* $T_2, E_2$ *:Thickness and Young's modulus of compliant cylinder, c : Viscous damper per square meter of the modeled object.*

Considering the equation (5-1), the force $F_1$ carried by the rigid cylinder can be written as,

$$F_1 = A_a\left(\frac{E_1 X_1}{T_1} + c\dot{X}_1\right) \tag{5-3}$$

where the $X_1$ is the deformation of the sensed object over the rigid cylinder and the compliant element of the sensor deformed to an amount $X_2$. The deformations $X_1$ and

$X_2$ are independent of each other. There is no shear force between the sensor and the sensed object.

The force $F_2$ carried by the compliant cylinder is,

$$F_2 = A_b[\frac{E_1(X_1 - X_2)}{T_1} + c(\dot{X}_1 - \dot{X}_2)] \tag{5-4}$$

Since the part of the force, $F_2$, flows through the object, the force $F_2$ can also be written in terms of sensor element deformation as,

$$F_2 = \frac{E_2 A_b X_2}{T_2} \tag{5-5}$$

The total force applied on the viscoelastic object is $F=F_1+F_2$.

The Force Ratio $F_1/F_2$ is given by,

$$\frac{F_1}{F_2} = \frac{A_a(\frac{E_1 X_1}{T_1} + c\dot{X}_1)}{\frac{E_2 A_b X_2}{T_2}} \tag{5-6}$$

Multiplying by $T_1T_2$, we get,

$$\frac{F_1}{F_2} = \frac{E_1 A_a X_1 T_2 + c A_a \dot{X}_1 T_1 T_2}{E_2 A_b X_2 T_1} \tag{5-7}$$

Now Equating equations (5-4) and (5-5) we get,

$$A_b[\frac{E_1(X_1 - X_2)}{T_1} + c(\dot{X}_1 - \dot{X}_2)] = \frac{E_2 A_b X_2}{T_2} \tag{5-8}$$

Rearranging the above equation we get,

$$c\dot{X}_2 + [\frac{E_1}{T_1} + \frac{E_2}{T_2}]X_2 = c\dot{X}_1 + \frac{E_1 X_1}{T_1} \tag{5-9}$$

Equation (5-9) is of the form $A\dot{y} + By = M\dot{x} + Nx$, which must be equal to a constant since both the $x$ and $y$ variables are time dependent and are independent. Hence from equation (5-9) we can assume,

$$\frac{[\frac{E_1}{T_1} + \frac{E_2}{T_2}]}{c} = \alpha \text{ and } \frac{[\frac{E_1}{T_1}]}{c} = \beta \tag{5-10}$$

Hence equation (5-9) can be simplified as,

$$\dot{X}_2 + \alpha X_2 = \dot{X}_1 + \beta X_1 = \omega \tag{5-11}$$

The general solution for the above equation is,

$$\begin{aligned} X_2 &= K_2 e^{(-\alpha t)} + \omega/\alpha \\ X_1 &= K_1 e^{(-\beta t)} + \omega/\beta \end{aligned} \tag{5-12}$$

where $K_2$, $K_1$ and $\omega$ are constant values.

Now substituting the above solutions into equation (5-7), we get,

$$\frac{F_1}{F_2} = \frac{E_1 A_a T_2 [K_1 e^{(-\beta t)} + (\omega/\beta)] + A_a T_1 T_2 c[\omega e^{(-\beta t)}]}{E_2 A_b T_1 [K_2 e^{(-\alpha t)} + (\omega/\alpha)}} \tag{5-13}$$

Initial conditions: When $t=0$, $X_1=X_2=0$. Hence from equation (5-12) after applying initial conditions we get,

$$K_1 = -\omega/\beta$$
$$K_2 = -\omega/\alpha \tag{5-14}$$

Substituting $K_1$, $K_2$ values in equation (5-13) we get,

$$\frac{F_1}{F_2} = \frac{E_1 A_a T_2[(-\omega/\beta)e^{(-\beta t)} + (\omega/\beta)] + A_a T_1 T_2 c[\omega e^{(-\beta t)}]}{E_2 A_b T_1[(-\omega/\alpha)e^{(-\alpha t)} + (\omega/\alpha)]} \tag{5-15}$$

Eliminating $\omega$ we get,

$$\frac{F_1}{F_2} = \frac{E_1 A_a T_2[\frac{1-e^{(-\beta t)}}{\beta})] + A_a T_1 T_2 c e^{(-\beta t)}}{E_2 A_b T_1[\frac{1-e^{(-\alpha t)}}{\alpha}]} \tag{5-16}$$

Multiplying by $\alpha\beta$ we get,

$$\frac{F_1}{F_2} = \frac{E_1 A_a T_2 \alpha[1-e^{-\beta t}] + A_a T_1 T_2 c\alpha\beta e^{(-\beta t)}}{E_2 A_b T_1 \beta[1-e^{(-\alpha t)}]} \tag{5-17}$$

Substituting the values of $\alpha$ and $\beta$ from equation (5-10) in equation (5-17) we get,

$$\frac{F_1}{F_2} = \frac{\left[E_1 A_a T_2 \left(\frac{E_1}{T_1} + \frac{E_2}{T_2}\right)(1 - e^{-\beta t})\right]/c}{\left[E_2 A_b T_1 (1 - e^{-\alpha t})\left(\frac{E_1}{T_1}\right)\right]/c} + \frac{\left[A_a T_1 T_2 \left(\frac{E_1}{T_1} + \frac{E_2}{T_2}\right)\left(\frac{E_1}{T_1}\right)e^{-\beta t}\right]/c}{\left[E_2 A_b T_1 (1 - e^{-\alpha t})\left(\frac{E_1}{T_1}\right)\right]/c}$$

Above equation is reduced to,

$$\frac{F_1}{F_2} = \frac{A_a}{A_b}\left[1 + \frac{E_1 T_2}{E_2 T_1}\right]\left[\frac{(1 - e^{-\beta t}) + e^{-\beta t}}{1 - e^{-\alpha t}}\right] \tag{5-18}$$

Assume $A_a = A_b$ we get,

$$\frac{F1}{F2} = \left[1 + \frac{E_1 T_2}{E_2 T_1}\right]\left[\frac{1}{1 - e^{-\alpha t}}\right] \tag{5-19}$$

Figures (5-10), (5-11) and (5-12) show the indirect variation of the force ratio with modulus of elasticity and the viscosity of the tissue at different times. As seen in figure (5-10), the force ratio increases rapidly to a very large magnitude and then decays down quickly. With increase in the loading and unloading time, the force ratio reduces to a lower magnitude as shown in figure (5-11) and figure (5-12). It means faster loading and unloading can give more accurate results to find the viscoelastic properties.

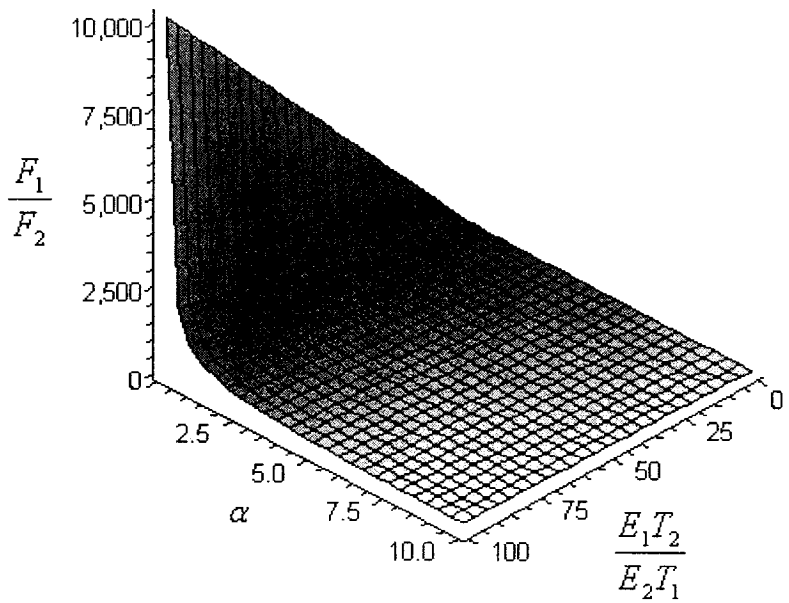


**Figure (5-10).** Variation of force ratio with modulus of elasticity and viscosity of the Kelvin-Voight model at a loading-unloading time of 0.1 sec.

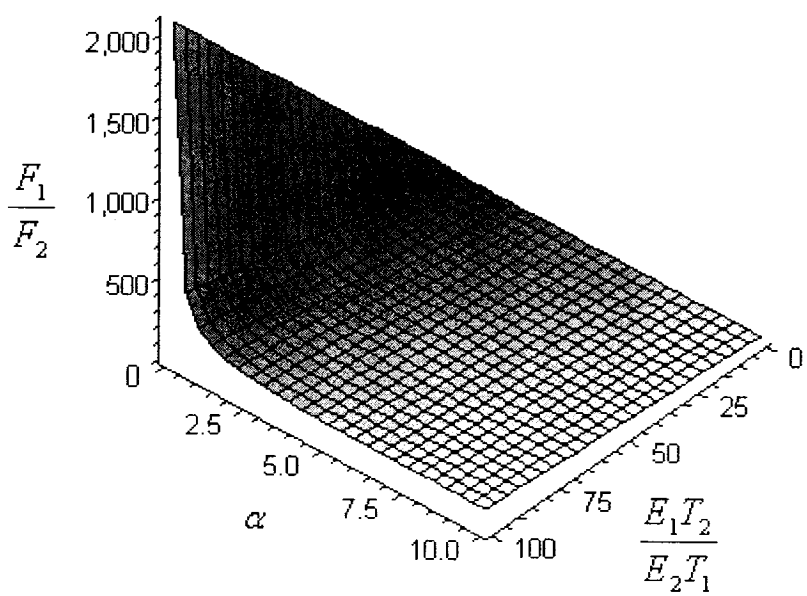


**Figure (5-11).** Variation of force ratio with modulus of elasticity and viscosity of the Kelvin-Voight model at a loading-unloading time of 0.5 sec.

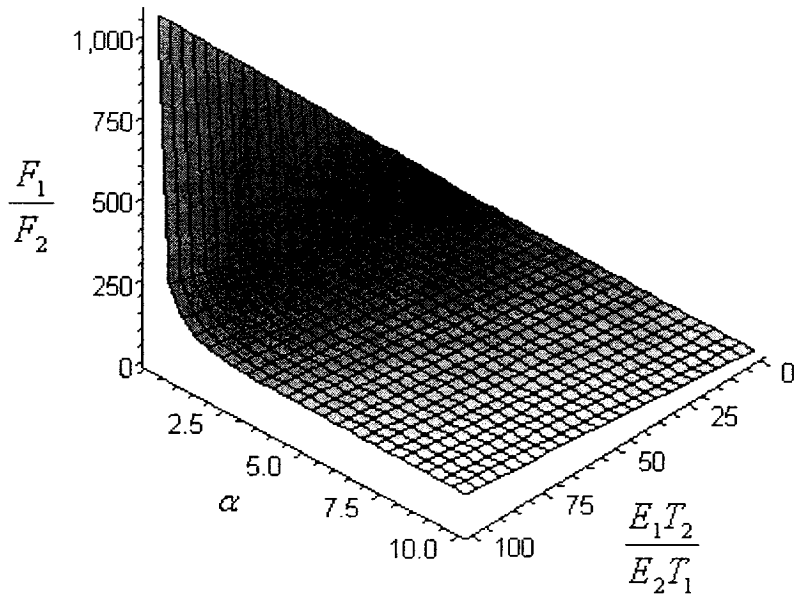


**Figure (5-12).** Variation of force ratio with modulus of elasticity and viscosity of the Kelvin-Voight model at a loading-unloading time of 1 sec.

From equation (5-19), when we put $c = 0$ which means $\alpha \to \infty$ , the equation reduces to,

$$\frac{F1}{F2} = \left[1 + \frac{E_1 T_2}{E_2 T_1}\right] \tag{5-20}$$

The above equation relates to elastic behavior of the sensor. Figure (5-13) shows the linear relation between the force ratio and Young's modulus of the elastic object.

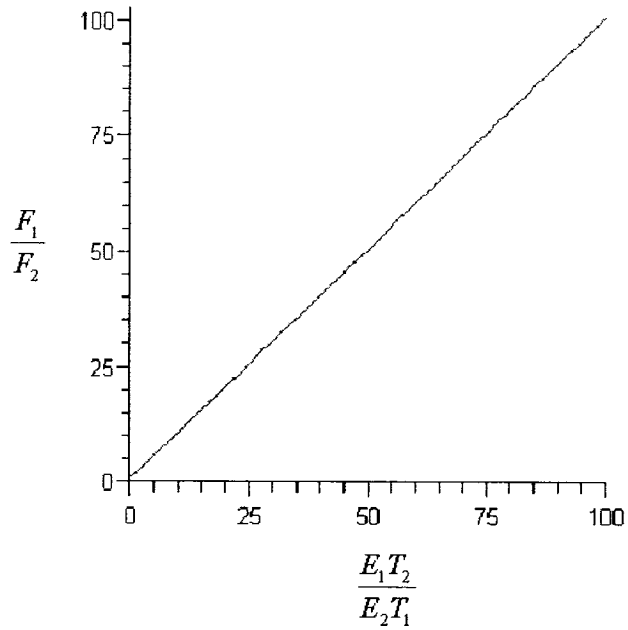


**Figure (5-13).** Variation of force ratio with modulus of elasticity in an elastic model.

### 5.3.2 Kelvin Model

The constitutive force displacement relation for Kelvin model can be derived as follows. From figure (5-14) we can see that F is the total force applied, $K_1$, $K_2$ are spring constants which are parallel to each other and $c$ is the damping coefficient.

The total force $F$ can be written as,

$$F = K_1 X + F_2$$

The total deformation $X$ can be expressed as a sum of $X_a$ and $X_b$, where $X_a$ is the spring displacement and $X_b$ is the relative displacement of the damper. This can be represented as follows.

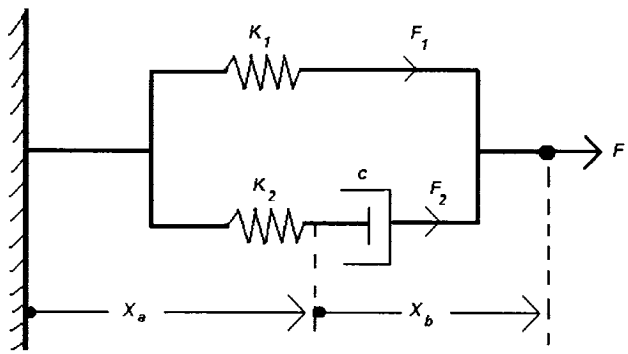


**Figure (5-14)**. Kelvin model.

$$X = X_a + X_b = \frac{F_2}{K_2} + \int_0^t \frac{F_2}{c} dt = \frac{F_2}{K_{eq}} \tag{5-21}$$

$$\frac{1}{K_2} + \frac{1}{cD} = \frac{1}{K_{eq}} \Rightarrow K_{eq} = \frac{K_2 \times cD}{K_2 + cD}$$

where $D$ is the Del operator and is defined as, $D(f(t)) = \frac{d(f(t))}{dt}$ and

$$\frac{1}{D}(f(t)) = \int f(t)dt$$

Substituting these values in equation (5-21), we get

$$F = K_1 X + \frac{K_2 \times cD}{K_2 + cD} X \Rightarrow F = X(K_1 + \frac{K_2 \times cD}{K_2 + cD}) \tag{5-22}$$

Rearranging the above equation, we get

$$F = [\frac{(K_1 K_2 + (K_1 + K_2)cD)}{K_2 + cD}]X \tag{5-23}$$

This is the general constitutive equation for the Kelvin model. This model is employed to analyze the sensor-tissue system modeled by a distributed Kelvin model as shown in the figure (5-15). The distributed Kelvin model is characterized by modulus of elasticities $E_1$, which is considered for determination of compliance, and $E_2$ and a distributed viscous damping coefficient of $C$ per unit length.

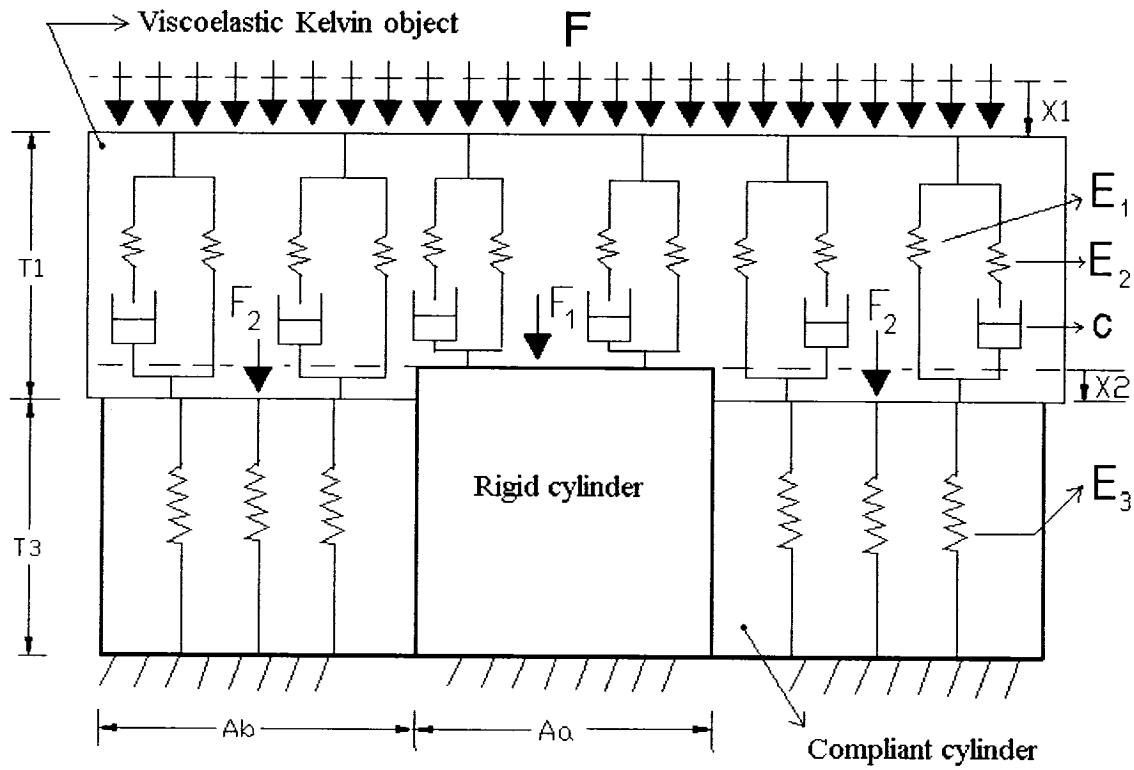


**Figure (5-15).** Analytical model of sensor–object configuration*

**Definition of the Notations*: *(Aa , area of the rigid cylinder; Ab, area of the compliant cylinder; T1, E1, E2 thickness and Young's modulus of the modeled object under investigation; T3, E3, thickness and Young's modulus of compliant cylinder; C, viscous damping co-efficient.).*

Considering the explanations in the previous section and following equation (5-23) the force $F_1$ carried by the rigid cylinder and the force $F_2$ carried by the soft cylinder on the application of a uniform load as shown in figure (5-15) are written as follows,

$$F_1 = A_a \left[ \frac{\left( \left( \frac{E_1 E_2}{T_1 T_2} \right) + \left( \frac{E_1}{T_1} + \frac{E_2}{T_2} \right) CD \right)}{\left( \frac{E_2}{T_2} + CD \right)} \right] X_1 \tag{5-24}$$

$$F_2 = A_b \left[ \frac{\left( \left( \frac{E_1 E_2}{T_1 T_2} \right) + \left( \frac{E_1}{T_1} + \frac{E_2}{T_2} \right) CD \right)}{\left( \frac{E_2}{T_2} + CD \right)} \right] (X_1 - X_2) \tag{5-25}$$

The force $F_2$ can also be written as sensor element deformation as

$$F_2 = \frac{E_3 A_b}{T_3} X_2 \tag{5-26}$$

From the above equations (5-24) and (5-26), we can write the force ratio as,

$$\frac{F_1}{F_2} = \frac{A_a K_I X_1}{A_b K_{III} X_2} \tag{5-27}$$

$$\text{where } \left[ \frac{\left( \left( \frac{E_1 E_2}{T_1 T_2} \right) + \left( \frac{E_1}{T_1} + \frac{E_2}{T_2} \right) CD \right)}{\left( \frac{E_2}{T_2} + CD \right)} \right] = K_I \text{ and } \frac{E_3}{T_3} = K_{III} \tag{5-28}$$

From equation (5-25) and (5-26) we get,

$$A_b K_I (X_1 - X_2) = A_b K_{III} X_2 \tag{5-29}$$

Since in reality, $T_1 = T_2$ and substituting the values of $K_I$ and $K_{III}$ we get,

$$A_b \left[ \frac{\left( \left( \frac{E_1 E_2}{T_1^2} \right) + \left( \frac{E_1}{T_1} + \frac{E_2}{T_1} \right) CD \right)}{\left( \frac{E_2}{T_1} + CD \right)} \right] (X_1 - X_2) = A_b \frac{E_3}{T_3} X_2 \tag{5-30}$$

$$\left[ \frac{\left( \left( \frac{E_1 E_2}{T_1} \right) + (E_1 + E_2) CD \right)}{(E_2 + T_1 CD)} \right] (X_1 - X_2) = \frac{E_3}{T_3} X_2 \tag{5-31}$$

Rearranging equation (5-31), we get,

$$X_2 \left( \frac{E_3}{T_3} + \frac{\frac{E_1 E_2}{T_1} + (E_1 + E_2) CD}{E_2 + T_1 CD} \right) = \left( \frac{\frac{E_1 E_2}{T_1} + (E_1 + E_2) CD}{E_2 + T_1 CD} \right) X_1 \tag{5-32}$$

Substituting equation (5-28) in equation (5-32), we get

$$X_2 (K_{III} + K_I) = (K_I) X_1 = \omega \tag{5-33}$$

$$K_I X_1 = \omega \text{ and } (K_{III} + K_I) X_2 = \omega \tag{5-34}$$

where, $\dfrac{\frac{E_1 E_2}{T_1} + (E_1 + E_2) CD}{E_2 + T_1 CD} = K_I$ and $\dfrac{E_3}{T_3} = K_{III}$

Thus from equation (5-33), we get,

Rearranging, we get a differential equation in $X_1$ as,

$$\frac{E_1E_2}{T_1}X_1 + (E_1 + E_2)C\dot{X}_1 = E_2\omega$$

$$\dot{X}_1 + \left(\frac{E_1E_2}{(E_1 + E_2)T_1C}\right)X_1 = \frac{E_2\omega}{(E_1 + E_2)C} \tag{5-35}$$

The solution of the above differential equation is

$$X_1 = K_1e^{(-\alpha t)} + \frac{\gamma}{\alpha} \tag{5-36}$$

where,

$$\left(\frac{E_1E_2}{(E_1 + E_2)T_1C}\right) = \alpha \quad \text{and} \quad \frac{E_2\omega}{(E_1 + E_2)C} = \gamma \tag{5-37}$$

Again from equation (5-33) we get,

$$X_2\left(\frac{E_3}{T_3} + \frac{\dfrac{E_1E_2}{T_1} + (E_1 + E_2)CD}{E_2 + T_1CD}\right) = \omega \tag{5-38}$$

Rearranging and simplifying we get,

$$\left(\frac{E_2E_3 + E_3T_1CD}{T_3} + \frac{E_1E_2}{T_1} + (E_1 + E_2)CD\right)X_2 = E_2\omega \tag{5-39}$$

On further solving and rearranging, we get a differential equation in $X_2$ as,

$$\dot{X}_2 + \left( \frac{\left( \frac{E_2 E_3}{T_3} + \frac{E_1 E_2}{T_2} \right)}{C\left( \frac{E_3 T_1}{T_3} + E_1 + E_2 \right)} \right) X_2 = \frac{E_2 \omega}{C\left( \frac{E_3 T_1}{T_3} + E_1 + E_2 \right)} \tag{5-40}$$

The above differential equation can be expressed as,

$$\dot{X}_2 + \beta X_2 = \eta \tag{5-41}$$

where, $\left( \frac{\left( \frac{E_2 E_3}{T_3} + \frac{E_1 E_2}{T_2} \right)}{C\left( \frac{E_3 T_1}{T_3} + E_1 + E_2 \right)} \right) = \beta$ and $\frac{E_2 \omega}{C\left( \frac{E_3 T_1}{T_3} + E_1 + E_2 \right)} = \eta$ (5-42)

The solution of equation (5-41) is expressed as,

$$X_2 = K_2 e^{-(\beta t)} + \frac{\eta}{\beta} \tag{5-43}$$

When $t = 0, X_1 = X_2 = 0$ which implies that $K_2 = -\frac{\eta}{\beta}$ and $K_1 = -\frac{\gamma}{\alpha}$

Substituting the above values for $X_1$ and $X_2$ in equation (5-27), we get

$$\frac{F_1}{F_2} = \frac{A_a \left( \frac{E_1 E_2}{T_1} + (E_1 + E_2) CD}{E_2 + T_1 CD} \right) \left( -\frac{\gamma}{\alpha} e^{-(\alpha t)} + \frac{\gamma}{\alpha} \right)}{A_b \frac{E_3}{T_3} \left( -\frac{\eta}{\beta} e^{-(\beta t)} + \frac{\eta}{\beta} \right)} \tag{5-44}$$

$$\frac{F_1}{F_2} = \frac{(A_a)\frac{\gamma}{\alpha}\left[\left(-e^{-(\alpha t)}+1\right)\frac{E_1E_2}{T_1}+(E_1+E_2)C\left(\alpha e^{-(\alpha t)}\right)\right]}{(A_b)\frac{\eta}{\beta}\frac{E_3}{T_3}\left[\left(-e^{-(\beta t)}+1\right)E_2+T_1C\left(e^{-(\beta t)}\right)\right]} \tag{5-45}$$

Multiplying by $\alpha\beta$, assuming $A_a$=$A_b$ and eliminating $\omega$ we get,

$$\frac{F_1}{F_2} = \left(\frac{T3}{E3}+\frac{T1}{E1}\right)\frac{\left[\left(-e^{-(\alpha t)}+1\right)\frac{E_1E_2}{T_1}+(E_1+E_2)C\left(\alpha e^{-(\alpha t)}\right)\right]}{\left[\left(-e^{-(\beta t)}+1\right)E_2+T_1C\left(e^{-(\beta t)}\right)\right]} \tag{5-46}$$

Let us consider $A = \dfrac{\left(-e^{-(\alpha t)}+1\right)\frac{E_1E_2}{T_1}+(E_1+E_2)C\left(\alpha e^{-(\alpha t)}\right)}{\left(-e^{-(\beta t)}+1\right)E_2+T_1C\left(e^{-(\beta t)}\right)}$ (5-47)

Simplifying it we can get,

$$A = \frac{\left(-e^{-(\alpha t)}+1\right)\frac{E_1E_2}{T_1}}{\left(-e^{-(\beta t)}+1\right)E_2+T_1C\beta\left(e^{-(\beta t)}\right)}+\frac{(E_1+E_2)C\left(\alpha e^{-(\alpha t)}\right)}{\left(-e^{-(\beta t)}+1\right)E_2+T_1C\left(e^{-(\beta t)}\right)} \tag{5-48}$$

Substituting the value of $\beta$ from equation (5-42), we get,

$$A = \frac{\left(-e^{-(\alpha t)}+1\right)\frac{E_1E_2}{T_1}}{\left(-e^{-(\beta t)}+1\right)E_2+T_1\left(\frac{\frac{E_2E_3}{T_3}+\frac{E_1E_2}{T_1}}{\frac{E_3T_1}{T_3}+E_1+E_2}\right)e^{-(\beta t)}}+\frac{(E_1+E_2)C\left(\frac{E_1E_2}{(E_1+E_2)T_1C}\right)e^{-(\alpha t)}}{\left(-e^{-(\beta t)}+1\right)E_2+T_1\left(\frac{\frac{E_2E_3}{T_3}+\frac{E_1E_2}{T_1}}{\frac{E_3T_1}{T_3}+E_1+E_2}\right)e^{-(\beta t)}}$$

Simplifying and rearranging we get,

$$A = \frac{\frac{E_1 E_2}{T_1}}{\left(-e^{-(\beta t)}+1\right)E_2 + T_1\left(\frac{\frac{E_2 E_3}{T_3}+\frac{E_1 E_2}{T_1}}{\frac{E_3 T_1}{T_3}+E_1+E_2}\right)e^{-(\beta t)}} \tag{5-49}$$

Let us consider the denominator of the equation (5-49) as follows,

$$S = \left(-e^{-(\beta t)}+1\right)E_2 + T_1\left(\frac{\frac{E_2 E_3}{T_3}+\frac{E_1 E_2}{T_1}}{\frac{E_3 T_1}{T_3}+E_1+E_2}\right)e^{-(\beta t)} \tag{5-50}$$

Simplifying the denominator, we get,

$$S = \left(-e^{-(\beta t)}+1\right)E_2 + T_1\left(\frac{E_2 E_3 T_1 + T_3 E_1 E_2}{E_3 T_1 + E_1 T_3 + E_2 T_3}\right)e^{-(\beta t)} \tag{5-51}$$

Simplifying further we get,

$$S = \frac{-E_2{}^2 T_3 e^{-(\beta t)} + E_2(E_3 T_1 + T_3(E_1+E_2))}{E_3 T_1 + T_3(E_1+E_2)} \tag{5-52}$$

Similarly $A$ can be expressed as,

$$A = \frac{E_1}{T_1}\left(\frac{E_3 T_1 + T_3(E_1+E_2)}{E_3 T_1 + T_3(E_1+E_2) - E_2 T_3 e^{-(\beta t)}}\right) \tag{5-53}$$

Substituting the above value in equation (5-46), we get

$$\frac{F_1}{F_2} = \frac{E_1}{T_1}\left(\frac{T_3}{E_3} + \frac{T_1}{E_1}\right)\left(\frac{(E_3T_1 + T_3(E_1 + E_2)}{E_3T_1 + T_3(E_1 + E_2) - E_2T_3e^{-(\beta t)}}\right) \tag{5-54}$$

After rearranging this results in,

$$\frac{F_1}{F_2} = \left(1 + \frac{E_1T_3}{E_3T_1}\right)\left(\frac{1}{1 - \left(\frac{E_2T_3}{E_3T_1 + T_3(E_1 + E_2)}\right)e^{-(\beta t)}}\right) \tag{5-55}$$

where $\beta = \left(\frac{\frac{E_2E_3}{T_3} + \frac{E_1E_2}{T_1}}{C\left(\frac{E_3T_1}{T_3} + E_1 + E_2\right)}\right)$

Equation (5-55) expresses the relationship between the force ratios, which are obtained experimentally, with the properties of the tissue at any instant. By measuring the force ratios over the period of time, the properties of the tissues such as $E_1$, $E_2$ and $C$ can be ascertained from equation (5-55) using the trial and error method through the computational analysis.

In the equation (5-55), if $t \to \infty$, or $C=0$ corresponding to negligible damping, we get $e^{-(\beta t)} = 0$. Therefore the whole equation can be reduced to an elastic behavior of the sensor-tissue model.

$$\frac{F_1}{F_2} = \left(1 + \frac{E_1T_3}{E_3T_1}\right) \tag{5-56}$$

Equation (5-56) is identical to the equation (5-20). It means that after a few seconds the selected model does not have influence on the result of sensor.

The above sensor-tissue model can be extended to an array of four sensors integrated to an endoscopic grasper based on the moment applied to the grasper jaws.

Assume $\frac{R_1}{d} = \frac{R_2}{2d} = \frac{R_3}{3d} = \frac{R_4}{4d}$ $\Rightarrow$ $R_1 = \frac{R_2}{2} = \frac{R_3}{3} = \frac{R_4}{4}$

where $R_1$, $R_2$, $R_3$ and $R_4$ are the reaction forces under the four sensors on the endoscopic grasper as shown in figure (5-16).

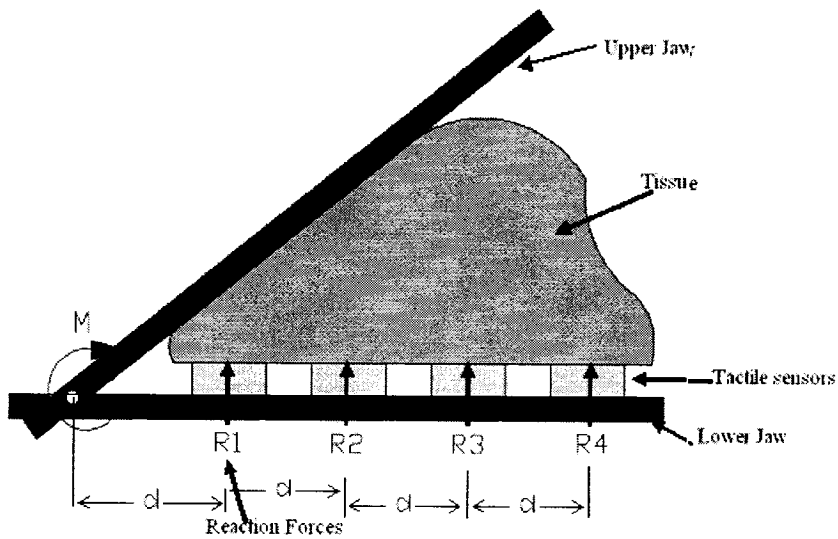


**Figure (5-16).** Reaction force of the array of sensor on grasper jaw.

Taking moment about joint $O$, we get,

$$M = R_1 d + 2R_1(2d) + 3R_1(3d) + 4R_1(4d)$$

$$M = 30R_1 d \Rightarrow R_1 = \frac{M}{30d} \qquad (5\text{-}57)$$

From the above equation (5-57), we can calculate the total forces applied to each sensor at the specific location.

### 5.4 Sensor Fabrication

In following, we describe the basic microfabrication processes used to fabricate the piezoelectric tactile sensor. The assembly of the sensor is also discussed.

#### 5.4.1 Micromachining

Semiconductor sensors are transducers that convert mechanical signals into electrical signals that are widely used for the measurement and control of physical variables. The list of applications of semiconductor devices is vast and discussion of the same is out of scope of this thesis. Over the past twenty years, interest in semiconductor sensors has been greatly fuelled by the application of microelectronic technology to the fabrication of mechanical devices. Micromachining technology takes advantage of the benefits of semiconductor technology to address the manufacturing and performance requirements of the sensor industry

In general, there is no single technology that can allow for fabrication of a wide variety of sensors. There are however two classifications in silicon micro-sensor technology namely Bulk Micromachining and Surface Micromachining. Bulk-micro machined sensors are made by accurate machining of a relatively thick substrate while Surface-micro machined sensors are fabricated from stacked thin films. Both technologies however, use materials and processes borrowed from VLSI technology. The three processes of deposition, lithography, and etching are sufficient to construct a wide variety of mechanical structures required for specific sensors.

Surface micromachining is the fabrication of micromechanical structures by deposition and etching of thin structural and sacrificial films. Surface micromachining relies on encasing specific structural parts of a device in layers of a sacrificial material during the fabrication process. The sacrificial material is then dissolved in a chemical etchant that does not attack the structural parts. In surface micromachining, the substrate wafer is used primarily as a mechanical support on which multiple, alternating layers of structural and sacrificial material are deposited and patterned to realize micromechanical structures. Surface micromachining enables the fabrication of complex, multicomponent, integrated micromechanical structures that would be impossible with traditional bulk micromachining. Thus, simple microstructures such as beams, membranes as well as complex structures such as linkages, encapsulated resonators can be fabricated on top of a silicon substrate.

### 5.4.2 Sensor Microfabrication Process

The tactile sensor consists of a silicon substrate with a PVDF film sandwiched between the silicon substrate and the rigid and soft cylinders. The geometrical size of the sensor was selected from the design calculations performed. Two designs, one a single sensor and other one with four sensors were realized. Both the designs had a silicon substrate as the base. Silicon substrate, PVDF, plexiglass and liquid silicone rubber were the materials involved in the fabrication of the sensor.

The microfabrication process sequences of the sensor are described below.

### 5.4.3 Silicon Wafer Cleaning Process

The material that is used for the substrate is silicon. The silicon wafer was first diced to the required dimension and then was cleaned to eliminate impurities such as dust, sodium, aluminum and native oxide. The cleaning process carried out is described as follows:

A double sided polished silicon wafer is first immersed in acetone and rinsed carefully for about 5 mins. Once the wafer is rinsed it is placed in an atmosphere of nitrogen so that any moisture that is present in the silicon is completely blown away. Then the diced wafer is kept in a hotplate and heated at 50°C for 5- 10 mins so that all the moisture is completely dried. Thus we have a silicon wafer devoid of any impurities.

### 5.4.4 Fabrication of Cylinders

#### A) Micro molding of outer cylinders

The next process is to get the outer hollow cylinder of the compliant rubber material. The fabrication of the outer hollow cylinder with a compliant object can be achieved by the process called micromolding. The material that is used for micromolding is liquid silicone rubber (SYLGARD 184) which was purchased from Dow corning Inc.

- The soft cylinder is fabricated by the process of micro molding of LIQUID SILICONE RUBBER (LSR) [85]. The desired shape is a hollow cylinder.
- To start with we have to create a mold cavity of the required shape and size of 6 mm outer diameter, 4 mm inner diameter and 1 mm depth. This cavity in the shape of hollow cylinder was achieved by very high precision machining.

- Once the cavity is created the LSR which comes as a combination of base (Octamethylcyclotetrasiloxane) and curing agent (Dimethyl, methylhydrogen siloxane) is mixed thoroughly in a beaker in a ratio 10:1. During mixing of the base and curing agent a lot of bubbles will be created. To get rid of these bubbles the base-curing agent mixture is deaerated with the help of a vacuum pump. This process is repeated until all the bubbles are completely removed.
- Once the bubbles are removed, the base-curing agent mixture is carefully poured into the mold cavity which was created by high precision machining. A few drops of teflon is sprayed around the mold cavity for easy removal of the cured rubbers.
- Then the mold cavity along with the LSR mixture is cured in an oven at a temperature of 150°C for 15 mins. The general curing temperature and the time for Sylgard 184 LSR is defined in table (5-2).

**Table (5-2).** Curing time-temperature chart for Sylgard 184 [62]

| Curing Temperature | Curing Time |
|---|---|
| Room temp | 48 hours |
| 100°C (212°F) | 45 minutes |
| 125°C (257°F) | 20 minutes |
| 150°C (302°F) | 10 minutes |

- Once the curing process is over, the ring shaped liquid silicone rubber structures are released from the cavity. Thus the final shape is realized which is of the order of 1 mm height as shown in figure (5-17).

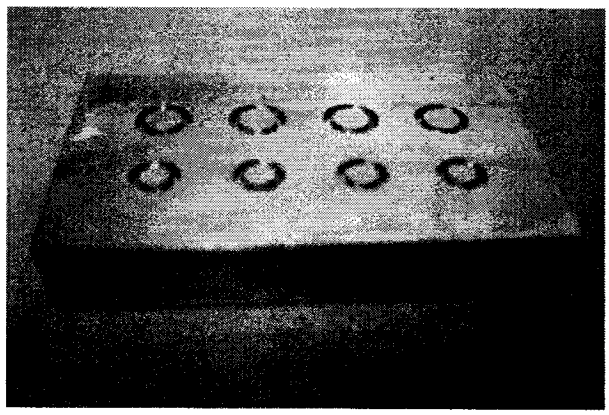

**Figure (5-17).** Mold cavity.

**B) Inner rigid Cylinder**

The inner rigid cylinder is made of plexiglass which is machined to the required diameter of 3 mm and 1mm height by high precision machining.

### 5.4.5 Patterning of PVDF films

This is the process of patterning the PVDF film for getting the required shape. UV light is directed through a mask to selectively expose photosensitive materials. Patterned regions can be manipulated by various processes (E.g.: Etching). In this process the PVDF film was patterned to get the required cylindrical shape. This section describes in detail the standard photolithography process.

#### 5.4.5.1 Overview of the Photolithography Process

Photolithography plays an important role in the fabrication of all micromechanical devices. During microelectronics device fabrication, there arises a need to selectively subject a portion of the sample to a variety of fabrication steps, leaving the rest of the sample untouched. Photolithography enables one to accomplish this. Patterning of

geometry with extremely high precision has been a major challenge for engineers. Photolithography or microlithography has been the only viable solution for producing high precision patterns on substrates at micro scale.

The photolithography is carried out in room illuminated with yellow light in order to reduce the adverse effects of light on the photosensitive resist material. In this process, photoresist (PR) is applied on a wafer by spin coating. The coated wafer is then dried in an oven, exposed to UV light and then developed using a developer. The purpose of the photo resist is to protect chosen regions of the wafer for subsequent fabrication steps. A schematic depicting of the process of photolithography is shown in the figure (5-18).

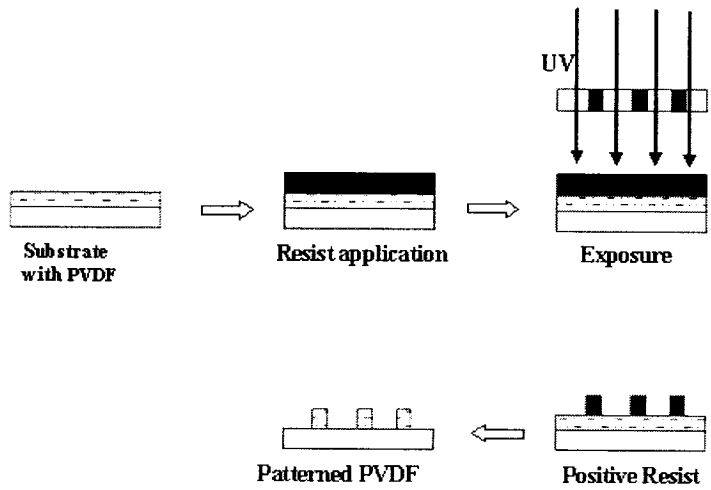


**Figure (5-18).** Photolithography process.

This section describes the photolithography process employed for our sensor fabrication.

a. Surface Preparation

b. Coating (Spin Casting)

c. Pre-Bake (Soft Bake)

d. Alignment

e. Exposure

f. Development

g. Post-Bake (Hard Bake)

h. Stripping of PR

**a) Surface Preparation:**

In this process the PVDF film is glued onto a silicon wafer using the photo resist (PR). A bare silicon wafer is first cleaned as described in the Section 3.2.1 and photoresist is spin coated on it. The photoresist here acts as glue for the PVDF on the silicon wafer. Then the PVDF film of the required size is cut and placed over the surface spin with photoresist. It is pressed so that the PVDF film gets glued to the substrate. Then the substrate along with the PVDF is soft baked for 30 sec at 75°C on a hot plate. Thus the PVDF is glued to the silicon substrate.

**b) Spin coating:**

There are number of photoresists that can be utilized in photolithography. Photoresists are generally classified as positive photoresist and negative photoresists. Positive photoresists are more sensitive to ultraviolet rays while the negative photoresists are less sensitive to X-ray exposure but more sensitive to electron beams. Generally positive resists provide more clear definition of the patterns. Hence we use a positive photoresist Shipley S1818 in our lithography process. Silicon wafer along with the PVDF film is held on a spinner chuck by vacuum and photoresist is coated to uniform thickness by spin coating. Seven to eight drops of photoresist is dropped onto the PVDF film and the chuck

is spun at a speed of 500 rpm for 15 sec and then at 3000 rpm for 30 seconds. By this method of spinning we ensure that the photoresist is coated uniformly over the PVDF film. The resist thickness is set primarily by resist viscosity and by spinner rotational speed. Figures (5-19) and (5-20) show the schematic and picture of a spin coater setup.

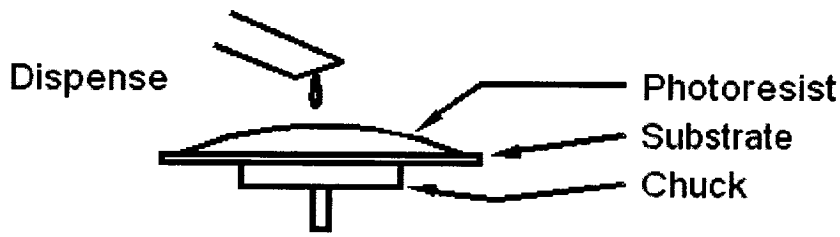


**Figure (5-19).** Schematic of spin coating set-up.

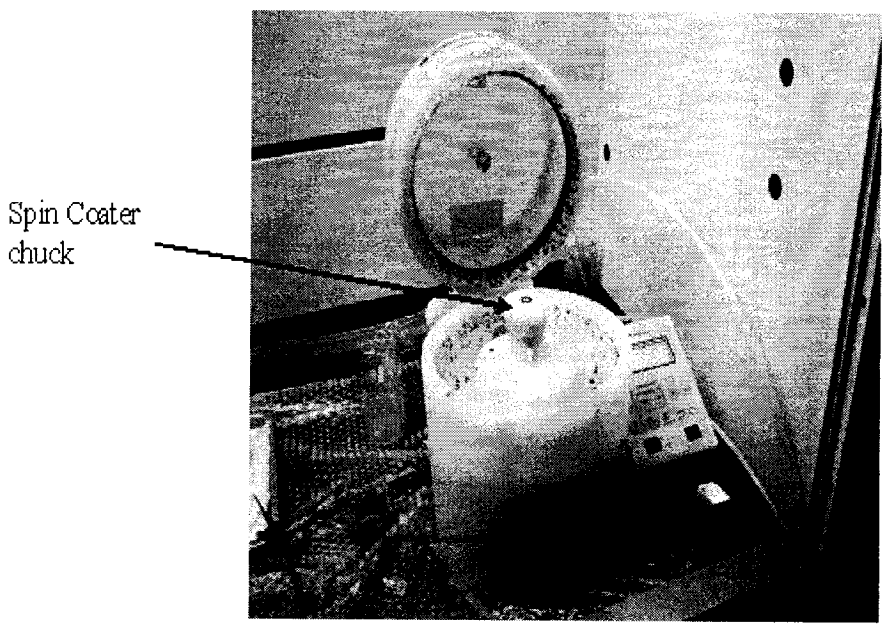


**Figure (5-20).** Spin coater set-up.

**c) Soft Bake:**

Once the PR is spun on the PVDF film the very next step is to soft bake it in an oven. This process is done to evaporate the coating solvent and to densify the resist after spin coating. Typical thermal cycles are

- 50°C for 40 min. in an oven
- 75-85°C for 45 sec. on a hot plate

Once the sample is soft baked, the next procedure is to expose it to UV light through the predefined light field mask. Figure (5-21) shows the photolithography set-up used to pattern PVDF.

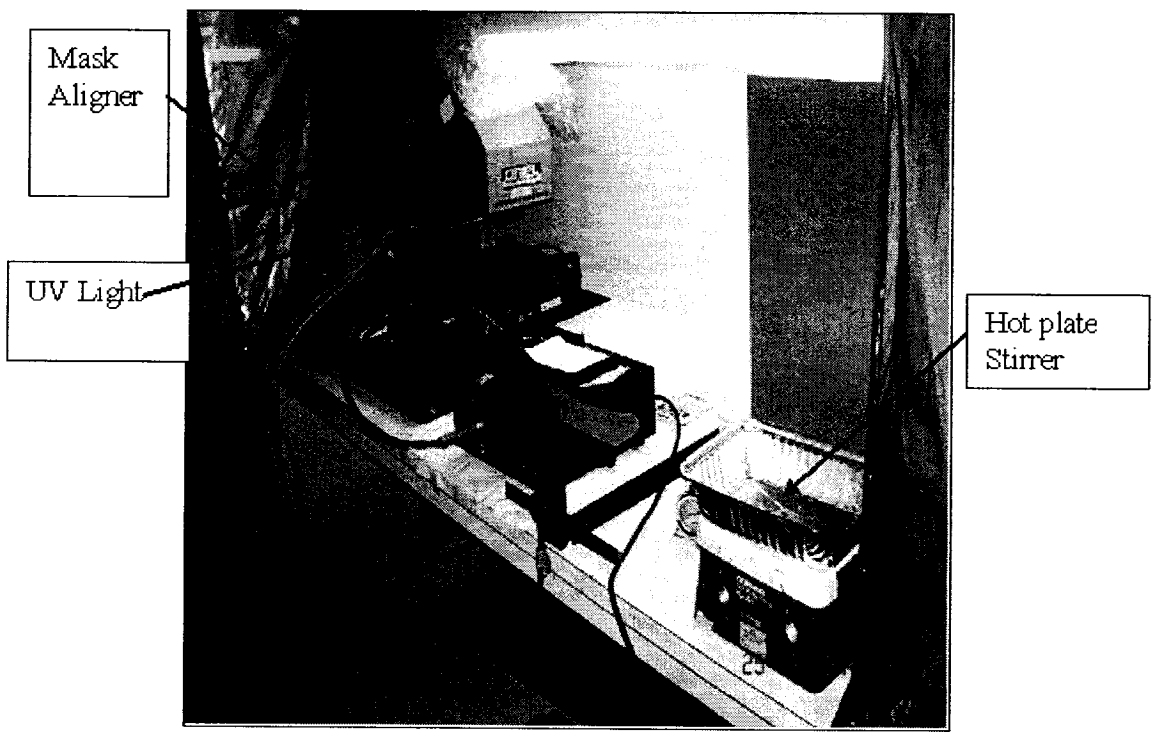


**Figure (5-21).** Photolithography Set-up.

**d) Mask Alignment and Exposure:**

Initially the mask for patterning aluminium electrodes on the PVDF film is designed in the AutoCAD and it is transferred on to a transparent sheet as shown in figure (5-22) and figure (5-23). For our design we need a light field mask as the aluminium electrodes have to be etched on a specific region. Once the Mask is aligned with the wafer using the alignment marks, the resist is exposed to the UV light through the mask. The exposure time for this sample is 23 sec.

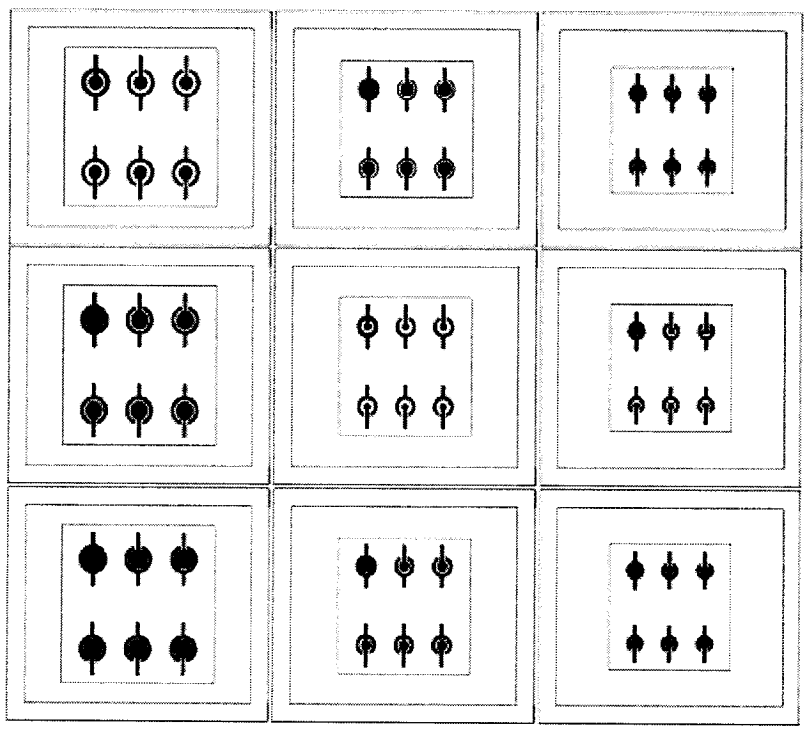

**Figure (5-22).** Mask layout for patterning.

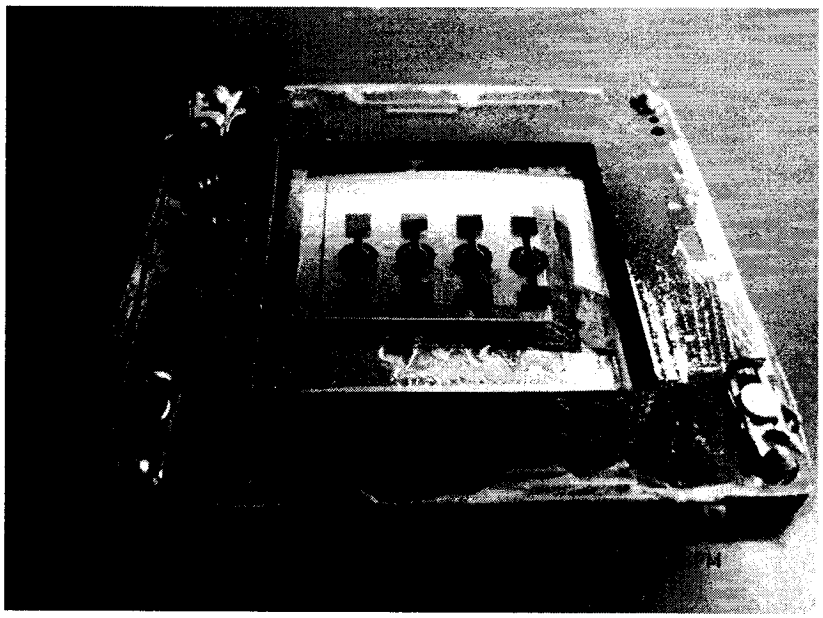

**Figure (5-23).** Mask for patterning.

**e) Photoresist Removal:**

Once the sample is exposed to the UV light source the next step is to develop the exposed sample in the developer solution. The sample is dipped in the developer solution and rinsed continuously until a clear pattern is visible. All the exposed regions of the sample will be completely removed by the developer solution. Once the sample is clearly developed it is rinsed in distilled water for a few seconds. After the sample is rinsed in water nitrogen is passed through it to dry the sample.

**f) Post Bake:**

Post bake removes any remaining traces of the coating solvent or developer. This step is necessary in order to harden the photoresist and to improve adhesion of the photoresist to the wafer surface. This eliminates the solvent burst effects in vacuum processing. Post bake introduces some stress into the photoresist. Some shrinkage of the PR may occur. Longer or hotter post bake makes resist removal much more difficult. Usually the post bake is done at temperature of 115° C. But for PVDF it is done at 50°C for 30-40 min.

### 5.4.6 Etching

Once the PR is stripped off, the PVDF sample is dipped in a commercial aluminum etchant TRANSENE ALUMINIUM ETCHANT A, which anisotropically etches the aluminium on the PVDF sheet without affecting the PVDF. In order to prevent under etching of the PVDF sample glued to the silicon wafer, photoresist is applied along the edges of the PVDF film and it is baked till the photoresist hardens. Thus under etching of the aluminium electrodes of the PVDF film is prevented. The etchant is heated in a water bath at 50°C. Once the etchant attains the required temperature the sample is dropped into the etchant and is left for 20-30 min. Then the sample is removed from the etchant and is rinsed in distilled water and is dried nitrogen gas. Thus the patterned aluminium electrodes are etched using a commercially available etchant. Following the above mentioned patterning procedure for a four-sensor PVDF film, we can fabricate a patterned PVDF with sensors as shown in figure (5-24).

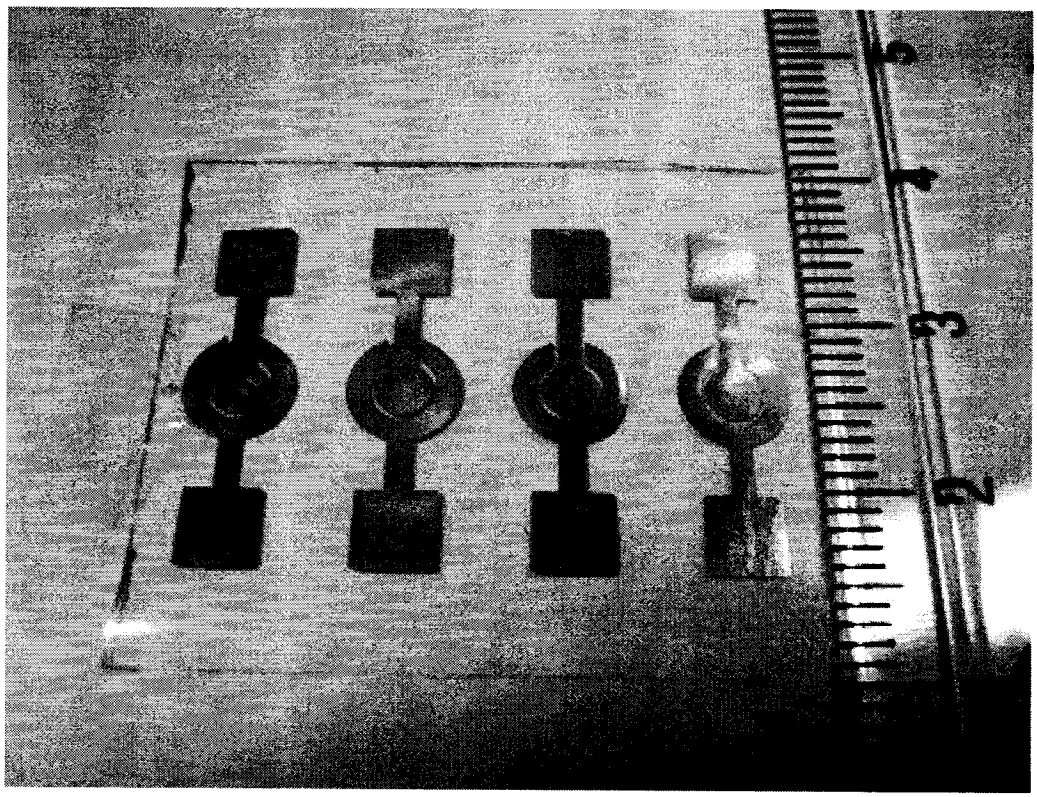

**Figure (5-24).** Patterned PVDF film after etching.

### 5.5 Single Sensor Assembly

Once the different parts of the sensor are realized by following the above procedures, the next step is to assemble them. The following steps are followed to assemble the sensor. A thin layer of nonconductive epoxy is applied to the patterned side of the PVDF. Working under a stereo microscope and using the alignment marks, the rigid and the compliant cylinders are glued over the patterned PVDF films. This assembly is uniformly pressed using a compression block to ensure even adhesion and is cured inside an oven at 50°C for 1 hr. Then electrical leads are attached to the PVDF. This is done by soldering AWG 30 copper wires to the PVDF. The complete assembled sensor is shown in fig (5-25).

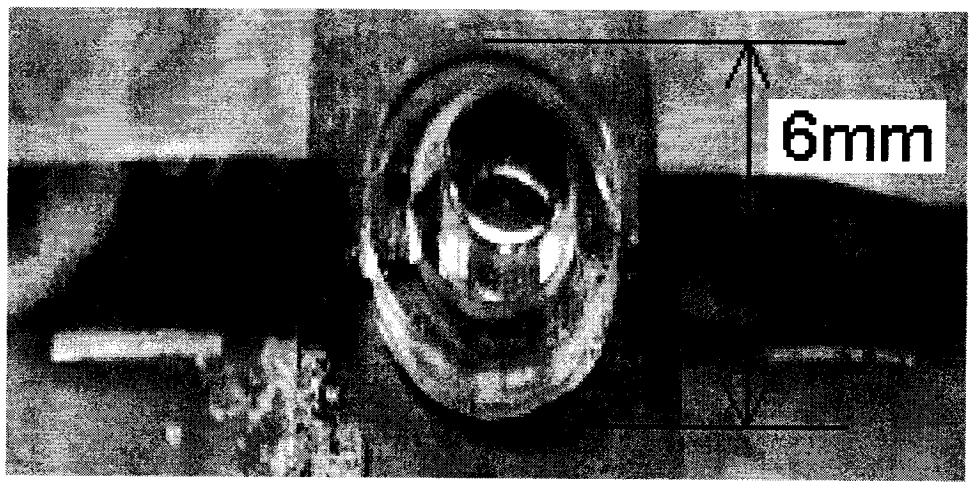


**Figure (5-25).** Assembled sensor after fabrication.

### 5.6 Four Sensor Assembly

The fabrication procedure for a single sensor and four sensors are almost the same except for the etching time. To increase the etching rate, the temperature of the etchant is increased from 50° C to 65° C. The four sensor array after fabrication is assembled in the same way as the single sensor and it is integrated to the grasper with the help of a dovetail jaw. The dovetail jaw which is designed using the AutoCAD is machined in the Concordia university machine shop. The sensor assembly along with the substrate is attached to the dovetail jaw using an epoxy so that it is rigid enough during grasper operation. The figures (5-26) and (5-27) show the four-sensor assembly and its integration with the grasper.

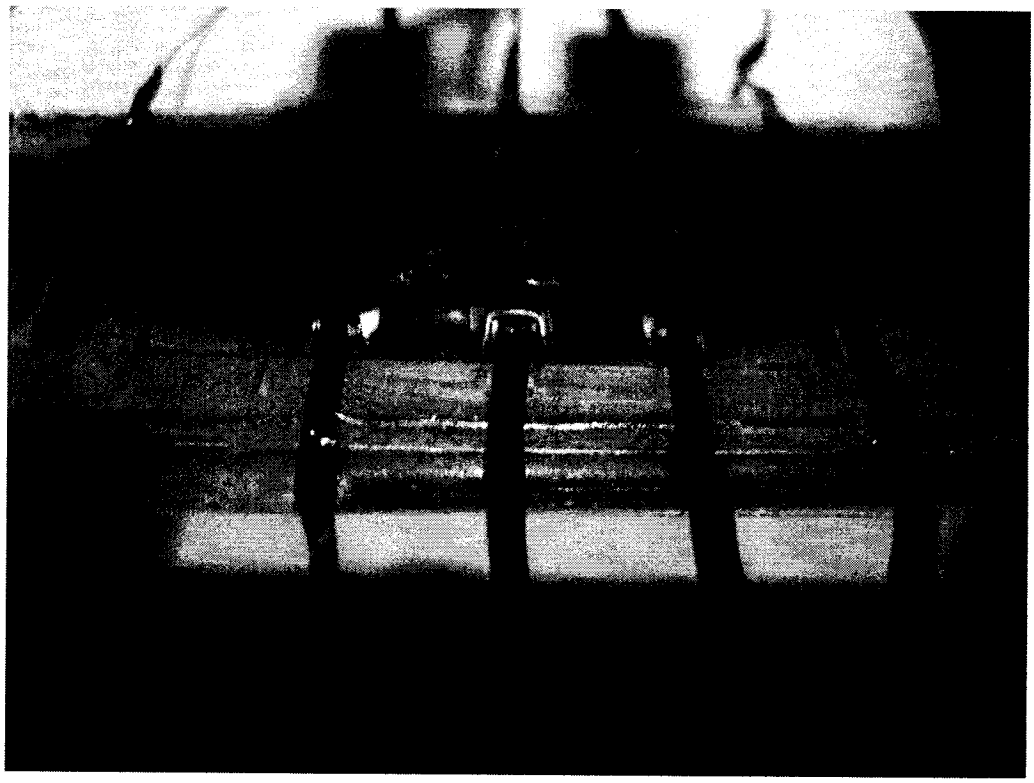

**Figure (5-26).** Array of sensors.

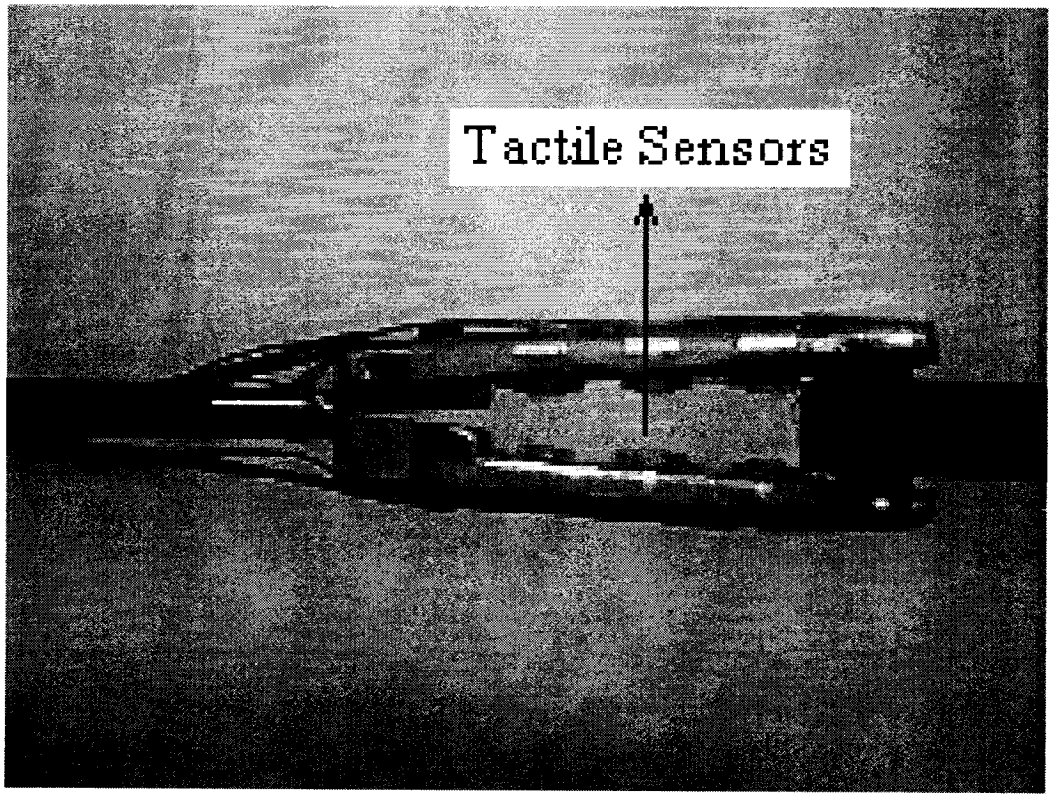


**Figure (5-27).** Endoscopic grasper with four sensors on each jaw.

### 5.7 Single Sensor Testing

The main objective of testing the sensor with different materials is to characterize these materials based on their compliance. The voltage generated by the sensor during the testing of different materials is used in the equations derived to find the softness value of the materials tested. Alternatively, the equations could be solved in a processor integrated with the sensor for ready characterization of the softness values. The details of the experimental setup are represented in figure (5-28). As seen in the figure (5-28), a cylindrical probe, which is attached to a flat and large area end, is used to apply force to the test objects uniformly, driven by a vibration unit, which provides the sinusoidal force.

The magnitude of the applied force is determined by a force transducer (Kistler, Type 9712B50) inserted between the probe and the vibration unit.

(a) (b)

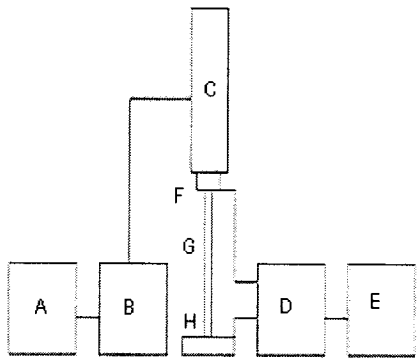


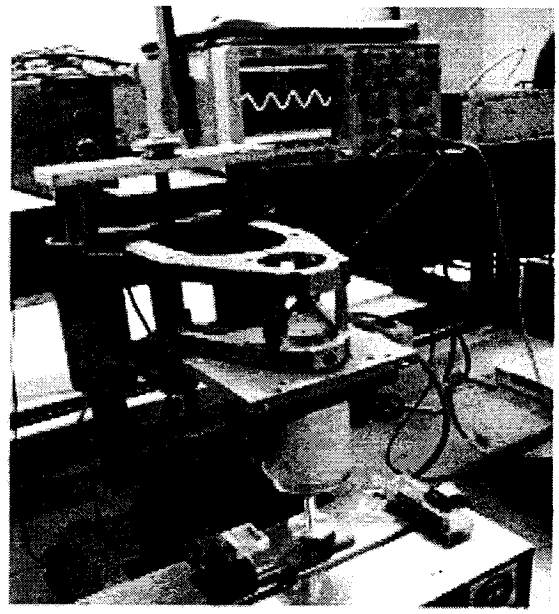

A-Power Amplifier
B- Signal Generator
C-Vibrator
D- A/D Converter
E- Computer
F-Force Transducer
G-Probe
H-Sensor

**Figure (5-28).** (a) Schematic diagram of Testing Setup (b) Photograph of the testing setup.

The test samples are sliced in the form of rectangles using a hot and thin metal string foam cutter. They are placed between a cylindrical probe and the sensor. A sinusoidal force is applied using a force transducer. The test frequency is varied from 10 Hz to 40 Hz and the voltages for each case are recorded. Based on the test materials, the rigid and compliant element of the sensor will carry different forces and hence the PVDF under the

rigid and compliant cylinders generate different voltages. These voltages are fed into a computer using an A/D converter and data acquisition system. Lab view 7.1 software is used to process the signals from the Data acquisition system. The signals from the PVDF have considerable noise, which are removed using a low pass filter of cut-off frequency 45 Hz. The voltage outputs from the rigid and soft cylinders correspond to $F_1$ and $F_2$, respectively, and the amplification factor is 10 mV/lbf. Hence the voltage ratio corresponds to the force ratio. Figure (5-29) shows the voltage outputs from rigid and compliant cylinders for a sample object (Material # 1).

(a)

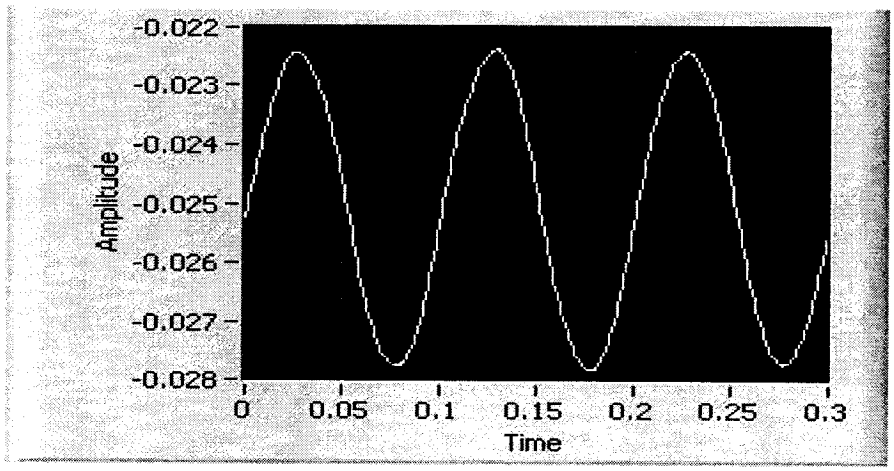


(b)

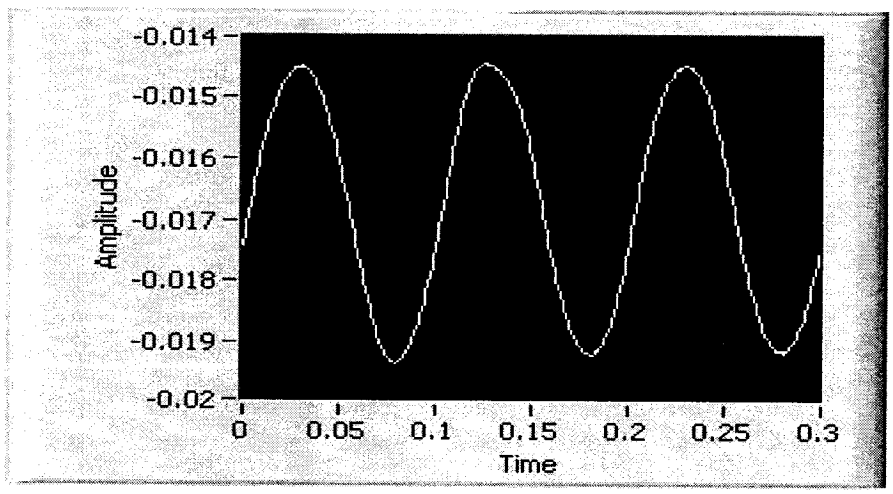


**Figure (5-29).** Voltage output after filtering (a) From the Inner rigid cylinder (b) From the outer soft cylinder.

**Table (5-3).** Experimental result of the sensor for different material and its comparison with given values.

| Material | Inner cylinder Voltage V1 | Outer cylinder Voltage V2 | Voltage ratio V1/V2 | "E" of the Material from Experiment | "E" of the Material from the compression tests | Percentage Error |
|---|---|---|---|---|---|---|
| | Volts | Volts | | MPa | MPa | % |
| Mat#1 | 0.0027 | 0.0024 | 1.10 | 1.66 | 1.36 | 18 |
| Mat#2 | 0.0043 | 0.0017 | 2.45 | 31.46 | 27.5 | 12.5 |
| Mat#3 | 0.0033 | 0.0013 | 2.49 | 106.43 | 98.55 | 7.5 |

Three samples are tested and their E values are calculated by the force ratio values from the tests and using them in equation (5-20) derived in the section 5.3.1. These E values, as shown in table (5-3), are compared to the values of the compression tests performed on the same sample previously. We find a deviation of 10-20%.

### 5.8 Finite Element Analysis for Single Sensor

A FEM analysis is carried out on the sensor-tissue model to find out the reaction forces under the rigid and soft cylinders for different materials being tested. The sensor-tissue model has been built using element solids 92 and 98. Solid 92 is a three dimensional tetrahedral structural solid element with 10 nodes. It has a quadratic displacement behavior and is suitable for a model that has irregular meshing. Each node has three

degrees of freedom in *x, y* and *z* directions. This element is for meshing the irregular and curved parts of sensor. The cylindrical parts and object are meshed with this element as well as the rigid and compliant cylinders. Solid 98 is a tetrahedral coupled field solid with 10 nodes and with up to six degrees of freedom at each node [69]. This element behaves similar to solid 5 but has good meshing properties for irregular geometries. The element has quadratic displacement behavior and is well suited to models having irregular meshes. The three-dimensional magnetic, thermal, electric, piezoelectric and structural field capability is similar to that described for Solid 5 and is used for meshing the circular PVDF films.

A quarter model of the sensor-tissue is used for structural analysis because of meshing issues and the symmetrical in nature of the sensor. A simple structural analysis has been done for different soft materials on top of the sensor. The force obtained at the inner and outer PVDF films has been found for different materials and the force ratio has been found.

The material properties of all the individual parts of the sensor and material specifications were defined as detailed in this chapter. The rigid cylinder and the substrate has the same material properties as discussed in the chapter dealing with sensor design. For these materials, we define the isotropic properties and the Poisson's ratio. Similarly, for the compliant cylinder and sensed object, the isotropic properties and Poisson's ratio are defined as 7.1 *MPa* and 0.45, respectively. The PVDF films have anisotropic behavior and electrical properties. The sensed materials are assigned the material property similar to the samples being tested experimentally. The sensed object properties are changed for

Material#1, Material#2, Material#3 and the ANSYS results are simulated. The sensed object properties are assigned as per the Manufacturer's data.

A quarter model of the sensor with the tissue is considered with the exact dimensions of sensor due to the issues with difficulty in meshing the full sensor, as shown in figures (5-30) and (5-31). The whole structure was created from different parts, which are suitably positioned and glued.

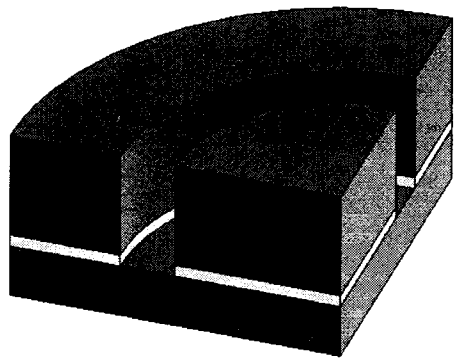

**Figure (5-30).** Sensor structure without the sensed object.

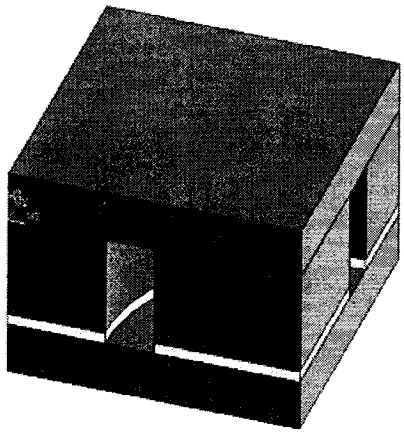

**Figure (5-31).** Sensor structure with the sensed object.

The load is applied on the surface of the sensed object in a uniformly distributed manner as shown in figure (5-32). The boundary conditions is fixed for the sensor whose base substrate is assumed to be fixed. The boundary conditions are applied to a sensed object so as to make zero displacement in the *XY* plane and a load is applied on the sensed object. As shown in figure (5-32), the load is applied on different node numbers on top of the sensed object. A load of 10 N is applied on each node and the force ratios obtained at the PVDF under the inner and outer cylinders are determined.

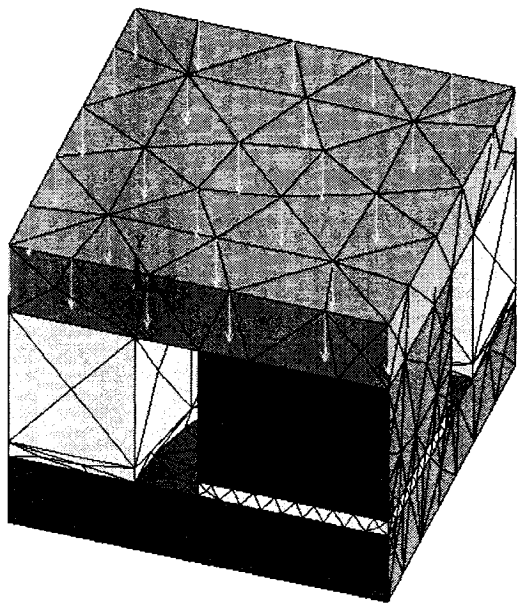

**Figure (5-32).** Uniform Load application on all top nodes.

Deformed shapes of sensor are plotted for checking geometrical deformation in the sensor. Stress distributions are also plotted. The material properties assigned for the sensed object are changed during the simulation according to the sample being tested. The thickness of the sensed object is the same as that of the one tested experimentally.

But our main focus is to determine the effect on the rigid cylinder and voltage generated by PVDF films.

Figure (5-33) shows the deflection of the sensor when the load is applied. The sensed object comprises a hard material (Material#1). It can be seen that the maximum deflection occurs in the rigid cylinder, which means that there is more force on the inner PVDF than on the outer PVDF.

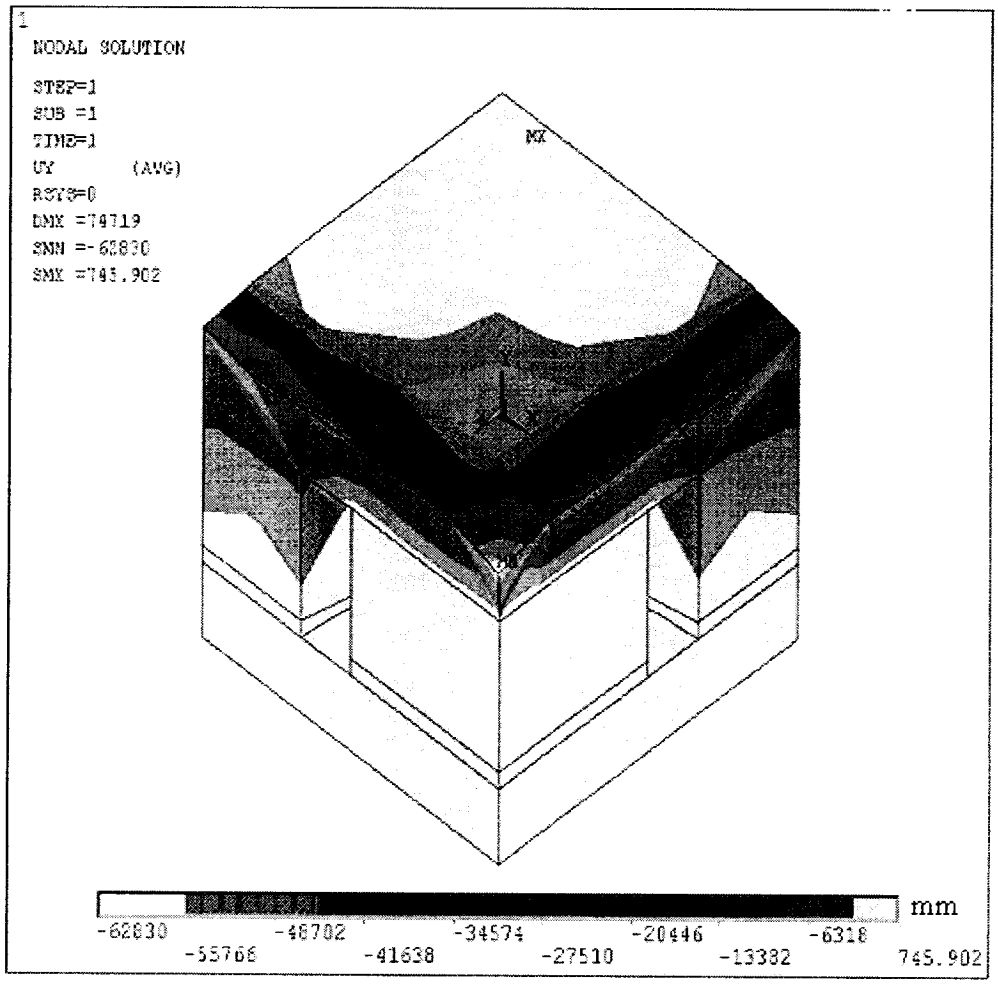


**Figure (5-33).** The deflection of the sensor structure after the application of load.

Figure (5-34) shows the stress distribution in the Y direction along the structure of the sensor for the sensed material (Material#1). It again shows that the maximum stress distribution occurs along the rigid cylinder. The maximum value is 0.927e9 Pa.

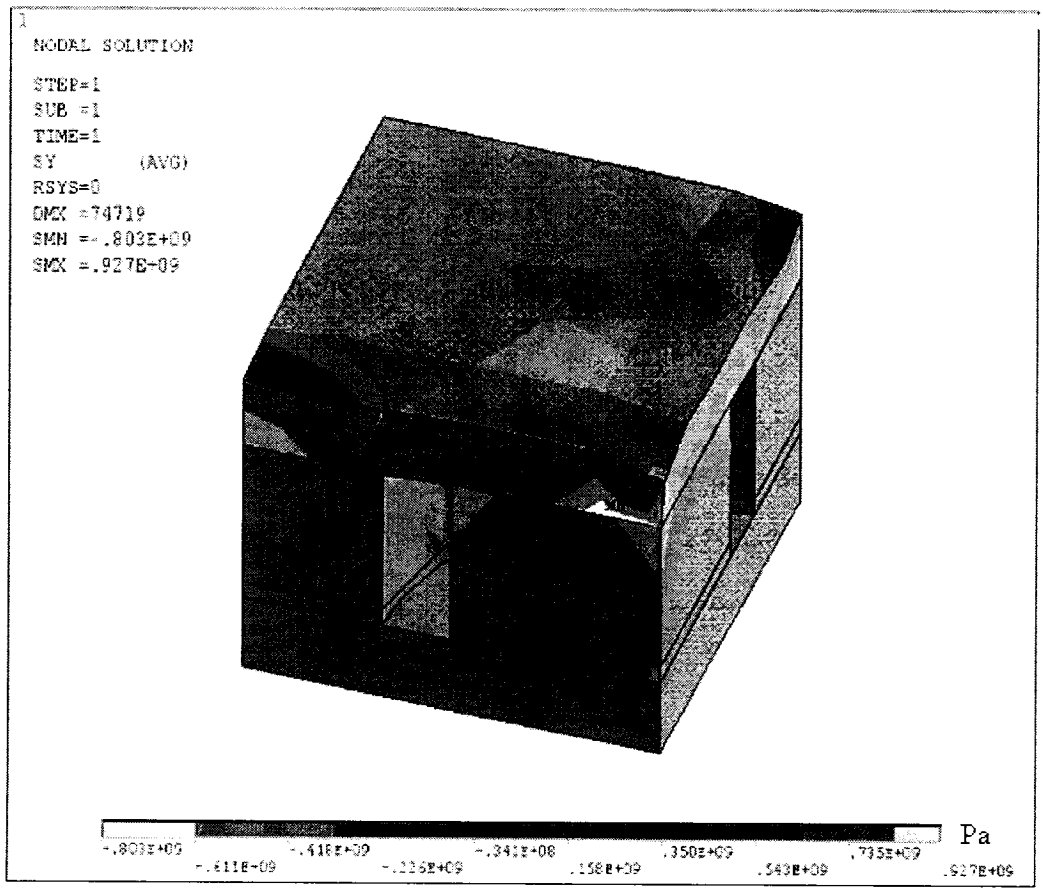


**Figure (5-34).** Stress distribution in the Y direction over the sensor structure.

Figure (5-35) shows the Von-Mises stress distribution across the sensor for Material#1.Finally, the reaction force at the nodes under the inner PVDF and outer PVDF were tabulated and the force ratios obtained as shown in Table (5-4). This force ratio, which is equal to the voltage ratio, is compared to the experimental value. The table

below shows the force values at inner PVDF and the outer PVDF for all the three materials. The maximum stress is 0.279e10 Pa

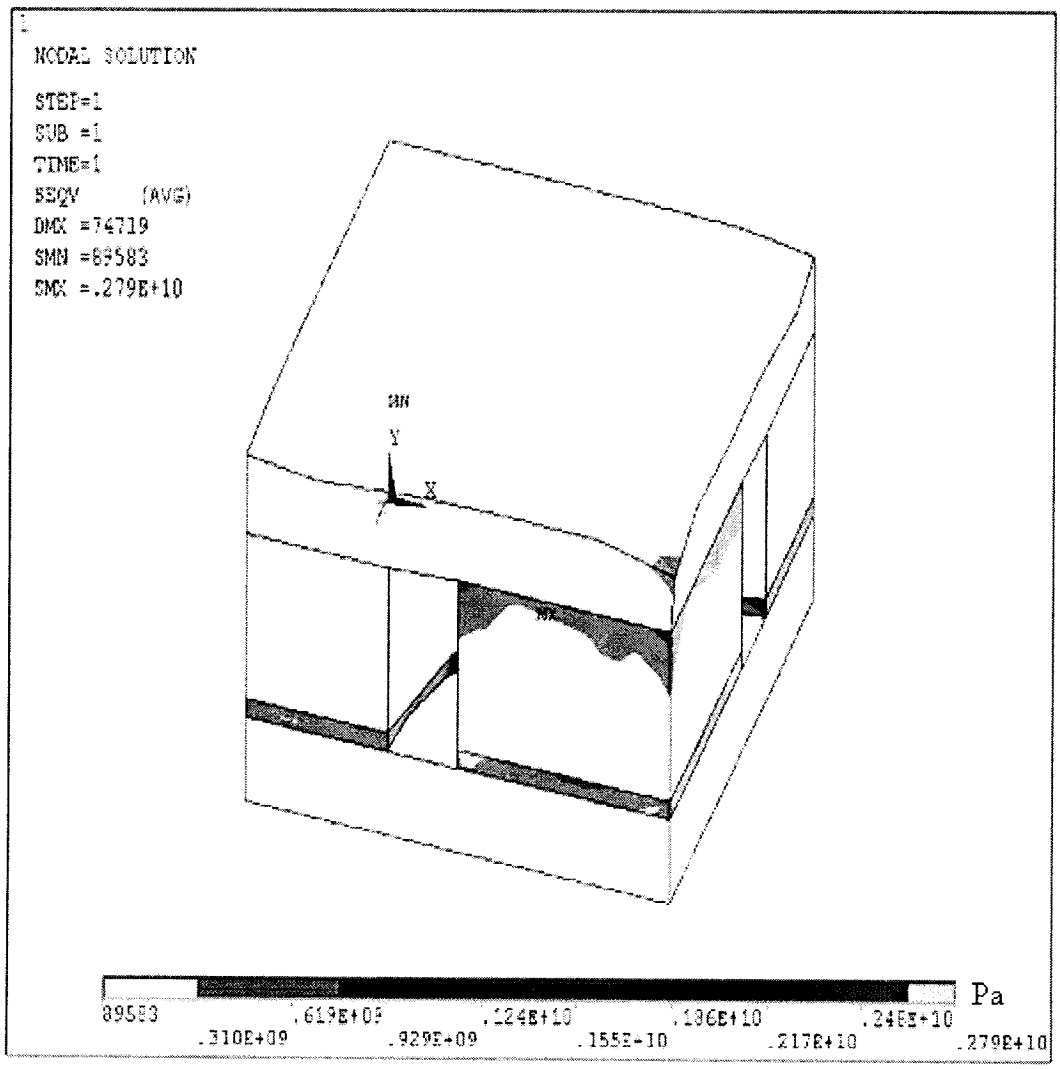


**Figure (5-35).** Von-Mises stress distributions over the sensor structure.

Since the voltage ratio is equal to the force ratio in our sensor design, the reaction force at all the nodes under the inner PVDF and the outer PVDF are found and an average value of these forces is calculated as represented in table (5-4). The force ratio of inner and outer PVDF values are calculated and are compared to the voltage ratio found experimentally for single sensor in previous section and four sensor in next section..

**Table (5-4).** Reaction forces at the Inner and Outer PVDF for material# 1, 2 and 3 obtained by FEA.

| Materials | Force on the inner PVDF under the rigid cylinder $F_1$, N | Force on the outer PVDF from the compliant cylinder $F_2$, N | Force Ratio $F_1/F_2$ |
|---|---|---|---|
| MAT#1 | 8.23 | 1.77 | 4.64 |
| MAT#2 | 5.275 | 5.19 | 1.016 |
| MAT#3 | 5.342 | 5.722 | 0.933 |

### 5.9 Four- Sensor Array Testing

The four-sensor array after fabrication was assembled in the same way as the single sensor. The smart endoscopic grasper test system consists of an array of tactile sensors. The sensor is tested for a step load force input and each has two analog voltage outputs, which are generated from the forces applied by the load cell to the object. The sample

material under the sensor testing is shown in figure (5-36). These voltages are proportional to the softness of the grasped object and are interfaced using a data acquisition card via connectors and an electronic system. Using the data acquisition card, the signals are amplified, filtered, digitized and finally processed by a computer. Three kinds of materials are tested. A step load is applied to the test object. The peak to peak voltage and frequency values from the three channels is captured by the data acquisition and interface system.

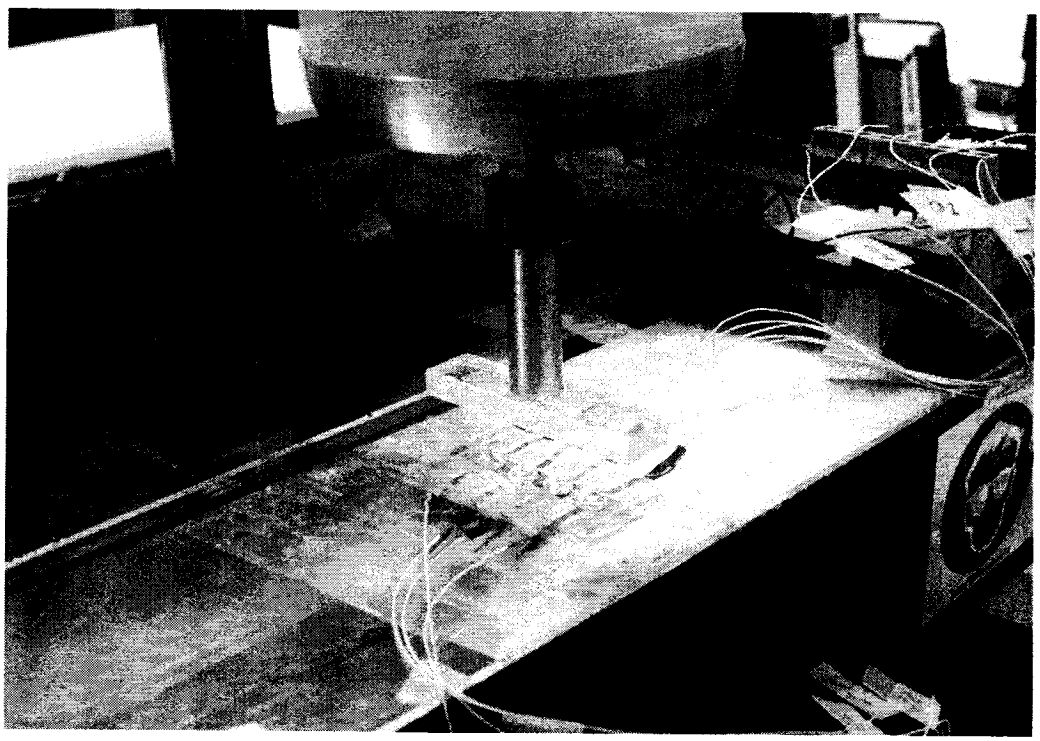

**Figure (5-36).** Sensor array with test object.

Three sample materials are tested by placing them on top of the array of sensors and applying a sinusoidal load of 1.8V at 10Hz. The readings from the PVDF under the rigid cylinder and the PVDF under the outer cylinder are recorded and tabulated. In the figures (5-37), (5-38) and (5-39) I1, I2, I3 and I4 denote the voltages (in millivolts) from the PVDF under the inner cylinder and O1, O2, O3 and O4 denote the voltages (in millivolts) from the PVDF under the outer cylinder and n1, n2, n3 and n4 denote the force ratio between the inner and outer PVDF.

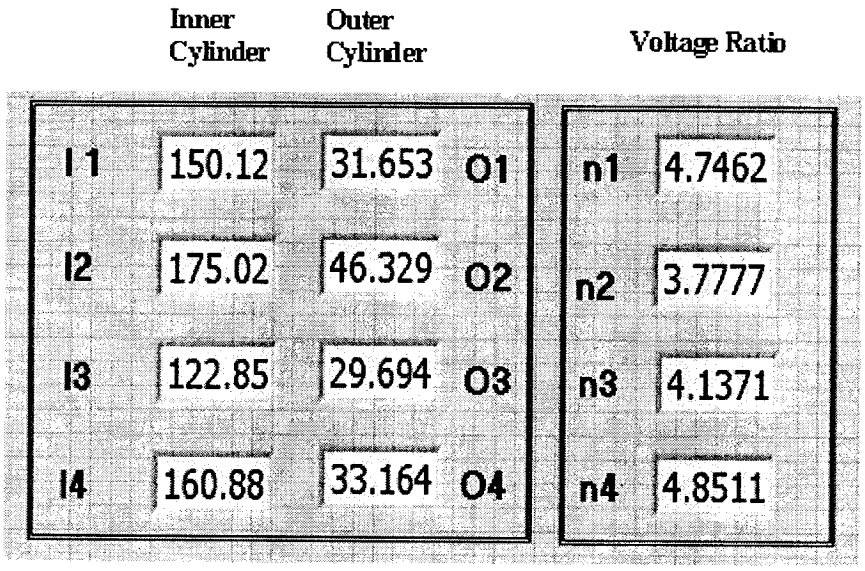


**Figure (5-37).** Four-sensor design voltage output for material#1.

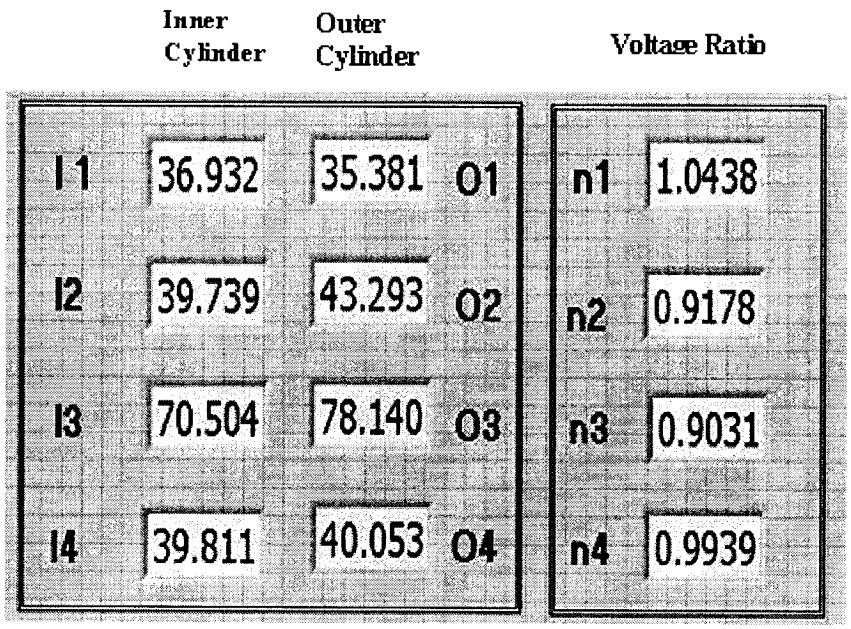


**Figure (5-38).** Four-sensor design voltage output for material#2.

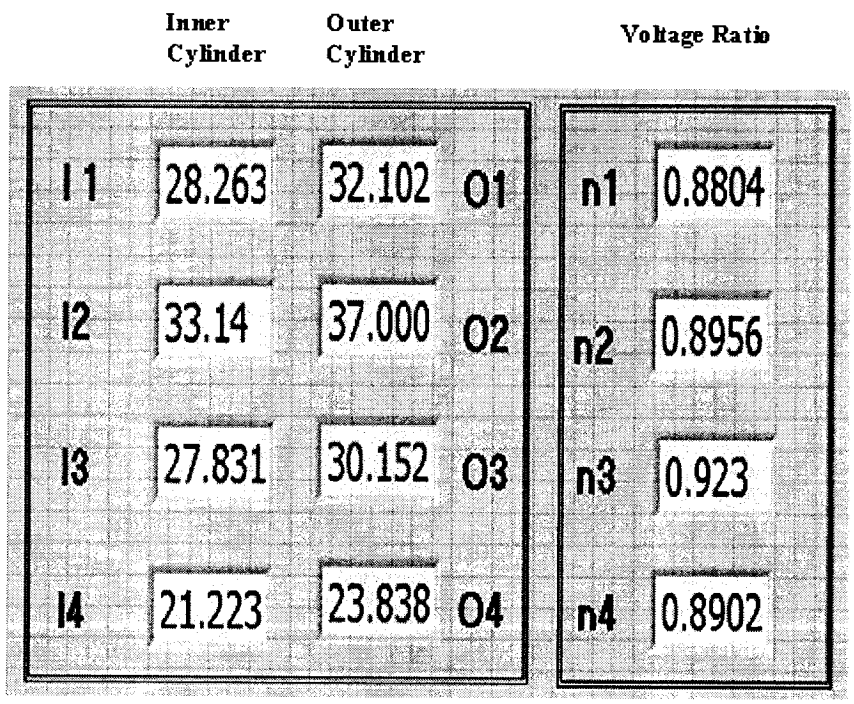


**Figure (5-39).** Four-sensor design voltage output for material#3.

Three samples are tested and their $E$ values are calculated by the force ratio values obtained from the test and then used in equation (5-20) in the analysis section.

The force ratio value is equal to the output voltage ratio values obtained from the experiments. $E$ values obtained from the single sensor design and four sensor designs are compared as shown in table (5-5) , which shows a variation of between 5% and 10% compared to the actual value of elasticity supplied by the manufacturer

**Table (5-5).** Force ratio and Young's modulus value comparison between single, four sensor and finite element results with the actual value.

| Material | Thickness | Single sensor voltage ratio | Four-sensor voltage ratio | FEM force ratio values | Single Sensor (E) | Four-Sensor (E) | Actual value (E) |
|---|---|---|---|---|---|---|---|
| | mm | | | | MPa | MPa | MPa |
| #1 | 3.0 | 4.6 | 4.37 | 4.64 | 183.33 | 173.18 | 170 |
| #2 | 3.0 | 0.91 | 0.96 | 1.016 | 21.77 | 24.13 | 22 |
| #3 | 3.0 | 0.87 | 0.89 | 0.933 | 16.56 | 17.35 | 15 |

### 5.10 Discussion and conclusion

We designed and fabricated an endoscopic grasper integrated with an array of micro fabricated tactile sensors in each jaw of the grasper which enable the surgeons to characterize the properties of any tissue encountered during a surgery in real time. An

analytical expression is also derived, which shows the magnitude of the variation of the elastic and viscoelastic properties of the materials at different loading–unloading times. This expression shows that fast loading and unloading is very important for characterizing the viscoelastic properties. As seen in the graphs, as the time increases the ability to find the viscoelastic properties decrease. In other words, the effect of the viscosity of the material will be apparent at the exact time of loading for a very short period. Therefore by considering these facts, the derived expression in this thesis is employed to characterize the viscoelastic material. One of the major benefits of the designed system is its miniaturized form. As a result, it could be mass-produced at low cost and even be disposable. Another advantage of these films are that various properties of the PVDF (both tactile and non tactile) are quite similar to the human skin and hence the simulation of the human skin behavior is quite realistic. In addition, a comprehensive finite element analysis has been performed to support the closed form analysis. The finite element results are in close agreement with the testing results and closed form results.

# CHAPTER 6

# CONCLUSIONS AND PROPOSED FUTURE WORKS

In this chapter, the summary of the work and conclusions as well as author's contributions to this study and proposed future works are presented.

## 6.1 Summary of Work

A closed form viscoelastic grasping contact analysis between the tissue and two models of wedge and semi-cylindrical teeth shape graspers was carried out. A mathematical expression was derived to express the relation of contact pressure and tissue properties. In addition, a comprehensive finite element analysis of grasper-tissue model was carried out to obtain the stress states and deformation of tissue together with contact pressure over the tissue. A prototype grasper with PVDF sensing areas was designed to validate the analytical and FEM results.

To determine the properties, particularly the compliance of the biological tissues during minimally invasive surgery, a single sensor and an array of sensors was designed and developed using a microfabrication process for fabrication. Two viscoelastic sensor-tissue models were introduced to analyze the sensor-tissue behavior. A mathematical equation was derived showing the relationship between the force ratios and the Young's modulus of the elastic materials. Experimentation was carried out using different loads for single sensor design and four sensor design. The voltage ratio outputs for the single sensor and the four sensor design were obtained experimentally and compared.

Elastic modulus of different test samples were found using experimental measurments along with analytical formulation for single and four-sensor design. The results were compared with the values supplied by the manufacturer. The force ratio obtained for the single sensor design for different materials was compared with corresponding voltage ratio outputs from the experiments using the same material.

### 6.2 Conclusions

In chapter 4, the closed form analysis provided the relationship between total force, contact area, relaxation and creep modulus for linear viscoelastic grasping contact using graspers having a corrugated wedge-like and semi-cylindrical profile. Comparison of the results in finite element with closed form analysis correctly confirms the assumption that the contact stresses are close to the contact area. Therefore, we could use the superposition principle for the closed form grasping analysis. In addition, the finite element analysis was carried out to show the stress status and deformation of the grasped tissue produced results that displayed close corroboration to other analytical studies.

One of the results of this study is the effect of the grasping period on contact pressure. It was shown that in order to prevent tissue damage, the grasping time should be reduced. This means that it is not recommended that the surgeon grasp tissue for any lengthy period since damage could occur due to creep effects.

Another result of this study is that by increasing the number of teeth, the rate of change of contact area reduces. Therefore, in order to prevent any possible damage to the tissue, the number of the teeth must be increased. In addition, the closed form analysis shows that there are no substantial differences between the results obtained from Kelvin and Maxwell models having the same parameters.

An experimental analysis was carried out to validate the closed form and FEA results. The results of this study enable surgeons to be aware of the contact force and pressure that is applied to tissues, thus preventing any damage to tissues during surgery. Finally, a comparison of the results shows that the shape of the grasper tooth is an important factor of the contact pressure value. It was shown that, under the same conditions, the contact pressure reduces with semi-cylinder grasper in comparison with the wedge-like grasper.

In Chapter 5, design and fabrication of a microfabricated endoscopic tactile sensor, which can be integrated with an endoscopic grasper was reported. This sensor enables the surgeons to characterize the properties of any tissue encountered during a MIS surgery in real-time.

An analytical expression is derived which shows the magnitude of the variation of elastic and viscoelastic properties of the materials at different loading and unloading times. This expression shows that fast loading and unloading is very important for characterizing viscoelastic properties. As can be seen in the graphs, as time increases the ability to find viscoelastic properties correspondingly decreases. This shows that the effect of the viscosity of the material will be apparent at the exact time of loading for a very short period. Therefore, by considering these facts, the derived expression in this study is employed to characterize the viscoelastic material. One of the major benefits of the designed system is its miniaturized form. As a result, it could be mass-produced at low cost and even be disposable.

In this particular design, care was taken to eliminate or reduce the effect of pyroelectricity by sandwiching the PVDF films between a substrate and the cylinders. In the design of the sensor, a gap of 1mm was allocated between the rigid and compliant

cylinders. The reason for this gap is to eliminate the friction between the two cylinders and hence to make the sensors operate more smoothly.

In addition, a comprehensive finite element analysis has been performed to support our closed form analysis. The finite element results are in close agreement with the testing results and those from the closed form expression.

Finally, the modulus of elasticity value calculated from the experimental along with analytical formulation obtained from the tactile sensor were compared with the modulus of elasticity of the materials suuplied by the manufacturer and it was found to be within an acceptable percentage difference of between 5% and 20% .

### 6.3 Contributions in the Thesis

This thesis presents studies regarding the grasping contact analysis of tissues for design and development of an endoscopic tactile sensor. In this section, the contribution of the author for this study is presented.

1. A novel analytical method was presented to determine the grasping contact pressure between a corrugated endoscopic grasper and tissue.
2. In order to obtain the contact pressure applied to a tissue encountered in endoscopic surgery, an expression was derived to show the relation between the grasping contact pressure and the properties of tissue and shape and dimension of the grasper.
3. A finite element viscoelastic grasping contact analysis was carried out using Ansys-10 software.
4. A novel prototype grasper-sensor was designed and fabricated to measure the grasping contact pressure.

5. A novel microfabricated tactile sensor was designed to determine the tissue properties and especially compliance of tissue.
6. A novel viscoelastic sensor-tissue model was designed to determine the compliance of tissue analytically.

### 6.4 Proposed Future Works

There are investigations that could not be included in this thesis which, however, would provide better understanding and will be useful.

1- We did not consider the effects of friction in the analysis. For more precise results, this will be taken into account in future works.

2- More work is required on other different viscoelastic models to obtain more accurate results.

3- More work is required on the miniaturization aspect and fabrication methodology. Proper packaging and protection from the environment is also required for more effective functioning of the sensor.

4- Another main aspect of the design of the sensor is to consider the effect of fluids on the sensor because, in reality, the sensors are mounted on endoscopic graspers which interact with fluids inside the body. The leakage of charges from the PVDF and wires will affect the performance of the sensor and hence proper insulation and protection from the fluid should be considered in any further work.

5- More work is also required for better assembly of each sensor and appropriate provisions should be made for cleaning and sterilization. The effect of shear on the sensor could be considered in future analysis in order to determine the roughness and slip of tissues from the endoscopic grasper. The sensor was susceptible to noise

during the experiment. Proper shielding should be installed so that the sensor output does not become affected by noise signals.

# BIBLIOGRAPHY


1. Tendick F., Sastry S. S., Fearing R. S., and Cohn M., "Applications of Micromechatronics in Minimal Invasive Surgery", IEEE Trans. Mechatron., Vol. 3, pp. 34-42, 1998.
2. Cohn M. B., Lam N., and Fearing R. S., "Tactile Feedback for Teleoperation in Telemanipulator Technology", SPIE Proc., Boston, pp. 240–254, 1992.
3. Dario P., "Tactile Sensing–Technology and Applications", J. Sensors and Actuators A—Phys, Vol. 26, pp. 251–256, 1991.
4. Bicchi A., Canepa G., DeRossi D., Iacconi P., and Scilingo E. P., "A Sensorized Minimally Invasive Surgery Tool for Detecting Tissutal Elastic Properties", IEEE Int. Conf. on Robotics and Automation, Minneapolis, MN, pp. 884–888, 1996.
5. Cohn M. B., Crawford L. S. and Wendlandt J. M., "Surgical Application of Milli-Robots", J. Robotics Systems, Vol. 12, no. 6: 401-416, 1995.
6. Fischer H., Heilig R., Trapp R., and Brhel K., "Tactile Optical Sensor for Use in Minimally Invasive Surgery", Langenbecks Archiv Fur Chirurgie, pp. 1290-1310, 1996.
7. Dizaji M., and Dizaji R. M., "Detection of Internal Displacement of Tissues in Ultrasound Images Using Image Registration Technique", IEEE CCECE, Canadian Conference, 2002.
8. Picinbono G., Delingette H., and Ayache N., "Nonlinear and Anisotropic Elastic Soft Tissue Models for Medical Simulation", Proc. ICRA. IEEE, 2001.

9. Gladilin E., Zachow S., Deuflhard P., and Hege H., "A Biomechanical Model for Soft Tissue Simulation in Craniofacial Surgery", International Workshop on Medical Imaging and Augmented Reality, 2001.

10. Tritto G., Pirlo G., and Tritto M. C., "Soft Tissues Expanders: Computer- Assisted Simulation of Elastic Mesh Deformation and Fractal Vascular Geometries in Controlled Skin Expansion", Proc. AIC. IEEE, pp. 1951-1952, 1989.

11. Tabore D., "The Hardness of Metals", Oxford University Press, Oxford University, 1951.

12. Johnson K. L, "The Correlation of Indentation Experiments", J. Mech. Phys., Vol. 18, pp. 115-126, 1970.

13. Doerner M. F., and Nix W. D., "A Method for Interpreting the Data from Depth-Sensing Indentation Instrument", J. Material Research, Vol. 1, pp. 601-609, 1986.

14. Spence, D. A., "The Hertz Contact Problem with Finite Friction", J. Elasticity, Vol. 5, pp. 297-305, 1975.

15. Sackfield A., and Hills D. A., "A Note on Hertz Contact Problem- A Correlation of Standard Formulae", J. Strain Analysis, Vol. 18, pp. 195-206, 1983.

16. Barber J. R., "The Solution of Elasticity Problems for the Half-Space by the Method of Green and Collins", J. Applied Science Res., Vol. 40, pp. 135-147, 1983.

17. Nowell D., Hills D. A., and Sackfield A., "Contact of Dissimilar Elastic Cylinders Under Normal and Tangential Loading", J. Mechanics and Physics, Vol. 36, pp. 59-73, 1988.

18. Hanson M. T., "The Elastic Field for Conical Indentation Including Sliding Friction for Transverse Isotropy", J. Applied Mechanics, Vol. 59, pp. 5123-5139, 1992.

19. Hanson M. T., "The Elastic Fields for a Sliding Conical Punch on an Isotropic Half-Space", J. Applied Mechanics, Vol. 60, pp. 557-576, 1993.

20. Munisamy R. L., Hills D. A., and Nowell D., "Static Axi-Symmetric Contacts Subject to Sharing Forces", J. Applied Mechanics, Vol. 61, pp. 278-298, 1994.

21. Greenwood, J. A., "Adhesion of Elastic Spheres", Proc. Royal Society, Vol. 453, pp. 1277-1297, 1997.

22. Greenwood J. A., "Adhesion at Single Point Contacts", Proc. 25th Leeds-Lyon Symposium Tribology, Lyon, 1998.

23. Johnson K. L., "Continuum Mechanics Modeling of Adhesion and Friction", Langmuir, Vol. 12, pp. 1277-1297, 1997.

24. Johnson K. L., "Adhesion and Friction between a Smooth Elastic Asperity and Plane Surface", Proc. Royal Society, Vol. 453, pp. 163-179, 1997.

25. Johnson K. L., and Greenwood J. A., "An Adhesion Map for the Contact of Elastic Spheres", J. Colloid and Interface Science, Vol. 192, pp. 326-333, 1997.

26. Johnson K. L., Sridhar I., and Fleck N. A., "Adhesion Mechanics of the Surface Force Apparatus", J. Physics, Vol. 30, pp. 1710-1719, 1997.

27. Bhushan B., "Contact Mechanics of Rough Surfaces in Tribology: Multiple Asperity Contacts", Tribology Lett, Vol. 4, pp. 1-35, 1998.

28. Change W. R., "An Elastic-Plastic Contact Model for Rough Surface", Wear, Vol.212, pp. 229-237, 1997.

29. Zhao Y., Maietta D. M., and Change L., "An Asperity Micro Contact Model Incorporating the Transition from Elastic Deformation to Fully Plastic Flow", ASME J. Tribology, Vol. 122, pp. 86-93, 2000.

30. . Komvopoulos K., and Ye N., "Three Dimensional Contact Analysis of Elastoplastic Layered Media with Fractal Surface Topographies", ASME J. Tribology, Vol. 123, pp. 632-640, 2004.

31. Giannakopoulos A. E., "Strength Analysis of Spherical Indentation of Piezoelectric Material", ASME J. Applied Mechanics, Vol. 67, pp. 409-416, 2000.

32. Mesarovic S. D., and Fleck N. K., "Frictionless Indentation of Dissimilar Elastic-Plastic Spheres", J. Solids and Structure, Vol. 37, pp. 7071-7091, 2000.

33. Liu G., Zhu J., Yu L., and Wang Q. J., "Elastoplastic Contact of Rough Surfaces", Tribol. Trans., Vol. 44, pp. 437-443, 2004.

34. Vu-Quoc L., Zhang X., and Lesburge L., "A Normal Force Displacement Model for Contacting Spheres Accounting for Plastic Deformation: Force-Driven Formulation", ASME J. Applied Mechanics, Vol. 67, pp. 363-371, 2004.

35. Liu G., Wang Q. J., and Lin C., "A Survey of Current Models for Simulating the Contact between Rough Surfaces", Tribol. Trans., Vol. 42, pp. 581-591, 1999.

36. Giannakopoulos A. E., Larsson P. L., and Vestergaard R., "Analysis of Vickers Indentation", J. Solids and Structure, Vol. 31, pp. 2679-2709, 1994.

37. Larsson P. L., Soderlund E., and Giannakopoulos A. E., "Analysis of Berkovich Indentation", J. Solids and Structure, Vol. 33, pp. 221-248, 1996.

38. Bhattacharya A. K., and Nix W. D., "Finite Element Simulation of Indention Experiments", J. Solids and Structure, Vol. 24, pp. 881-89, 1988.

39. Bhattacharya A. K., and Nix W. D., "Analysis of Elastic and Plastic Deformation Associated with Indentation Testing of Thin Films on Substrates", J. Solids and Structure, Vol. 24, pp. 1287-1298, 1988.

40. Laursen T. A., and Simo J. C., "A Study of Micro Indentation Using Finite Elements", J. Materials Research, Vol. 7, pp. 618-626, 1992.

41. Truman C. E., A. sackfield, and D. A. Hills, "Contact Mechanics of Wedge and Cone Indenters", J. Mechanical Science, Vol. 37, no. 3, pp. 261-278, 1995.

42. Storakers B, and Larsson P. L., "Similarity Analysis of Inelastic Contact", J. Solids and Structure, Vol. 34, pp. 3061-3083, 1997.

43. Klabring A., "Contact Problems with Friction and Application to Shape Optimization", Proc. SIAM, 1992.

44. Larsson P. L., "Investigation of Sharp Contact Rigid Plastic Conditions", J. Mechanical Science, Vol. 43, pp. 895-920, 2003.

45. Bonakdar Ali, "Inelastic Contact Analysis between a Wedge and Solid with Friction", MSc. Thesis, Sharif University of Technology, Tehran, Iran, 1997.

46. Read W. H, "Stress Analysis for Compressible Viscoelastic Materials", J. Applied Physics, Vol. 21, pp. 671-674, 1950.

47. Lee E. H., 'Stress Analysis in Viscoelastic Bodies", Quarterly J. Applied Mathematics, Vol. 13, pp. 183-190, 1955.

48. Radok J. R. M., "Viscoelastic Stress Analysis", Quarterly J. Applied Mathematics, Vol. 15, pp. 198-202, 1957.

49. Lee E. H., and Radok J. R. M., "The Contact Problem for Viscoelastic Bodies", J. Applied Mechanics, Vol. 27, pp. 438-444, 1960.

50. Hunter S. C., "The Hertz Problem for a Rigid Spherical Indenter and a Viscoelastic Half-Space", J. Mechanics and Physics of Solids, Vol. 8, pp. 219-234, 1960.

51. Graham G. A. C., "The Contact Problem in the Linear Theory of Viscoelasticity", J. Engineering Science, Vol. 3, pp. 27-46, 1965.

52. Graham G. A. C., "The Contact Problem in the Linear Theory of Viscoelasticity when the Time Dependent Contact Area Has any Number of Maxima and Minima", J. Engineering Science, Vol. 5, pp. 495-514, 1967.

53. Ting T. C. T., "The Contact Stresses between a Rigid Indenter and a Viscoelastic Half-Space", J. Applied Mechanics, Vol. 33, pp. 845-854, 1966.

54. Ting T. C. T., "Contact Problems in the Linear Theory of Viscoelasticity", J. Applied Mechanics, Vol. 35, pp. 248-254, 1968.

55. Cheng L., Xia X., Yu W., Scriven L. E., and Gerberich W. W., "Flat Punch Indentation of Viscoelastic Material", J. Polymer Science, Vol. 38, pp. 10-22, 2000.

56. Larrson P. L., and Carlsson S., "On Microindentation of Viscoelastic Polymer", Polymer Testing, Vol. 17, pp. 49-75, 1998.

57. Shimizu S., Yanagimoto Y., and Sakai M., "Pyramidal Indentation Load-Depth Curve of Viscoelastic Material", J. Materials Research, Vol. 14, pp. 4075-4086, 1999.

58. Sakai M., and Shimizu S.," Indentation Rheometry for Glass-Forming Materials", J. Non-Crystalline Solids, Vol. 282, pp. 236-247, 2001.

59. Sakai M., "Time-Dependent Viscoelastic Relation between Load and Penetration for an Axisymmteric Indenter", Philosophical Magazine, Vol. 82, pp. 1841-1849, 2002.

60. Oyen M. L., and Cook R. F., "Load-Displacement Behavior during Sharp Indentation of Viscous-Elastic-Plastic Materials," J. Materials Research, Vol. 18, pp. 139-150, 2003.

61. Oliver W. C., and Pharr G. M., "Improved technique for determining hardness and elastic modulus using load and displacement sensing indentation experiments", J. of Materials Research, Vol. 7, pp 1564-1580,1992.

62. Bonakdar A., Dargahi J., and Bhat R.,"Grasping Contact Analysis of Viscoelastic Materials with Applications in Minimally Invasive Surgery", Proc. of ASME Int. Mech. Eng. Congress and Exposition, Chicago, Illinois, 2006.

63. Bonakdar A., Dargahi J., and Bhat R., "Investigation on the Grasping Contact Analysis of Biological Tissue with Applications in Minimally Invasive Surgery", American J. Applied Sciences, Accepted for publication, 2007.

64. Bonakdar A., Molavi M., Dargahi J., and Bhat R., "Grasping Contact Analysis of Tissues with Semi-Cylindrical Teeth Grasper for Minimally Invasive Surgery Application", ASME Bioengineering Conference, Keystone, Colorado, 2007.

65. Melzer A., Buess G., and Cuschieri A., "Instruments and Allied Technology for Endoscopic surgery", Operative Manual of Endoscopic surgery 2, Springer-Verlag, New York, pp. 1-69, 1994.

66. Dargahi J., and Najarian S., "Analysis of a Membrane Type Polymeric Based Tactile Sensor for Biomedical and Medical Robotic Applications" J. Sensors and Material, Vol. 16, pp. 25-41, 2004.

67. Dargahi J., "An Endoscopic and Robotic Tooth-Like Compliance and Roughness Tactile Sensor", J. Mech. Design, Vol. 124, pp. 576-582, 2002.

68. Dario P., Carrozza M.C., Lencioni L, Maganani B., and D'Attanasio S., "A Micro Robotic System for Colonoscopy", IEEE Int. Conf. on Robotics and Automation, Albuquerque, New Mexico, pp. 1567–1572, 1997.

69. Kontarinis D.A., Son J.S., Peine W., and Howe R.D., "A Tactile Shape Sensing and Display System for Teleoperated Manipulation". IEEE Int. Conf. on Robotics and Automation, Nagoya, Japan, pp. 641–646, 1995.

70. Josivaldo G.S., Carvalho A.A., and Silva D.D.," A Strain Gauge Tactile Sensor for Finger Mounted Applications", IEEE Trans. On Instrumentation and Measurement, Vol. 51, No.1, 2002.

71. Shinoda H., and Andro S., "A Tactile Sensor with 5-d Deformation Sensing Element" IEEE Int. Conf. on Robotics and Automation, Minneapolis, MN, pp. 7–12, 1996.

72. Dargahi J., "A Three Sensing Element Piezoelectric Tactile Sensor for Robotic and Prosthetic Applications", J. Sensors Actuators Phys., Vol. 80, pp. 23-30, 2004.

73. Ohka M., Mitsuya Y., Takeuchi S., Kamaekawa O., and Ishihara H., "A 3-axis Optical Tactile Sensor—(FEM Contact Analysis and Sensing Experiments Using a Large-Sized Tactile Sensor)", IEEE Int. Conf. on Robotics and Automation, Nagoya, Japan, pp. 817–824, 2004.

74. Obana F.Y., Carvalho A.A., gualda and Silva G.J.,"A Semiconductor Strain Gauge Tactile Transducer", IEEE Instrumentation and Measurement Technology Conf, Budapest, Hungary, pp. 429-432, 2001.

75. Howe R. D., "Tactile Sensing and Control of Robotic Manipulation", J. Advanced Robotics Vol. 8, No. 3, pp. 245-261, 1994.

76. Fearing, R. S., "Tactile Sensing Mechanisms", J. Robotics Research, Vol. 9, No. 3, pp. 3-23, 1990.

77. Faraz S., Payandeh and Salvarinov A.," Design of Haptic Interface through Stiffness Modulation for Endosurgery: Theory and Experiments", IEEE International Conf. Robotics and Automation, Leuven, Belgium, 1998.

78. Petter E., Biehl M., and Meyer J., "Vibrotactile Palpation Instrument for Use in Minimal Invasive Surgery", Engineering in Medicine and Biology Society, Bridging Disciplines for Biomedicine. Proc. IEEE, 1996.

79. Ryan A., Beasley T., and Robert D., "Tactile Tracking of Arteries in Robotic Surgery", International Conf. on Robotic & Automation, proc. IEEE, Washington DC, 2002.

80. Youngping, Z., Arthur F., and Mak T., "Effective Elastic Properties for Lower Limb Soft Tissues from Manual Indentation Experiment", IEEE Transactions on Rehabilitation Engineering, Vol. 7, No. 3, 1999.

81. Bonakdar A., Dargahi J., Packirisamy M., and Bhat R.,"Design and Analysis of a Micromachined Piezoelectric Sensor for Measuring Viscoelastic Properties of Tissues in Minimally Invasive Surgery", J. Smart Material and Structures, Vol. 15, pp. 1684-1690, 2006.

82. Bonakdar A., Dargahi J., and Bhat R., "Mircofabricated Smart Endoscopic Device for Detecting Abnormality in Biological Tissues", AI/GI/CRV/IS Joint Conference, Montreal, Quebec, pp. 18-20, 2007.

83. Johnson K. L., "Contact Mechanics", Cambridge University Press, Cambridge, U.K, 1985.

84. Sohngen H., "Zur theorie Der Endlichen Hilbert Transformation", Math. Zeitschrift, Vol. 60, pp. 31-46, 1970.

85. Mase G. T., and Mase G. E., "Continuum Mechanics for Engineers", 2nd ed., CRC Boca Raton, 1999.

86. Fu G., "Theoretical Study of Complete Contact Indentations of Viscoelastic Materials", J. Materials Science, Vol. 38, pp. 2877-2886, 2004.

87. Findley W. N., Lai J. S., and Onaran K., "Creep and Relaxation of Nonlinear Viscoelastic Materials", Dover Mineola, 1989.

88. Fung Y. C., "Biomechanics: Mechanical Properties of Living Tissues", New York, Springer-Verlag, 1981.

# APPENDIX I

**Contact Analysis Between an Elastic Wedge and an Elastic Solid With Friction**

Figure (I-1) shows an elastic wedge indenting to an elastic solid. Boundary conditions for this problem are: ($\mu$ is coefficient of friction between to surfaces)

$$|q(x)| = |\mu p(x)| \tag{I-1}$$

$$u_{z1} + u_{z2} = \delta - (\cot\alpha)|x| \tag{I-2}$$

where, $u_{z1}$ and $u_{z2}$ are the displacements for solid and wedge, respectively.

Considering equation (2-9) for both half space and wedge, we get

$$\int_b^a \frac{p(s)}{x-s}ds = \frac{\pi(1-2\nu_1)}{2(1-\nu_1)}q(x) - \frac{\pi E_1}{2(1-\nu_1^2)}U'_{z1}(x) \quad \text{(For the half space)} \tag{I-3}$$

$$\int_b^a \frac{p(s)}{x-s}ds = \frac{-\pi(1-2\nu_2)}{2(1-\nu_2)}q(x) - \frac{\pi E_2}{2(1-\nu_2^2)}U'_{z2}(x) \quad \text{(For the wedge)} \tag{I-4}$$

By multiplying equations equation (I-3) and equation (I-4) in $(1-\nu_1^2)/E_1$ and $(1-\nu_1^2)/E_2$ and then adding together, we obtain,

$$\left(\frac{1-\nu_1^2}{E_1} + \frac{1-\nu_2^2}{E_2}\right)\int_a^a \frac{p(s)}{x-s}ds = \frac{\pi}{2}q(x)\left[\frac{(1-2\nu_1)(1+\nu_2)}{E_1} - \frac{(1-2\nu_2)(1+\nu_2)}{E_2}\right] - \frac{\pi}{2}(u'_{z1} + u'_{z2}) \tag{I-5}$$

Now we define a new variable $E^*$ as follows:

$$\frac{1}{E^*} = \frac{1-\nu_1^2}{E_1} + \frac{1-\nu_2^2}{E_2} \tag{I-6}$$

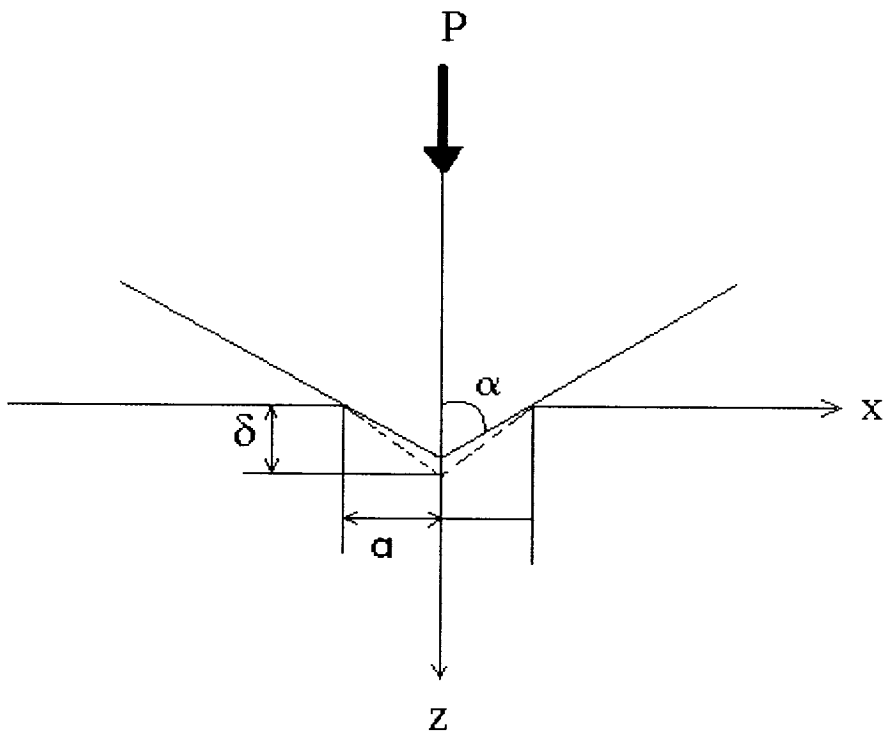


**Figure (AI-1).** An elastic wedge in contact with an elastic solid.

Since $G = E / 2\,(1+\nu)$, equation (I-6) can be rewritten as

$$\frac{1}{E^*} = \frac{1-\nu_1^2}{2G_1(1+\nu_1)} + \frac{1-\nu_2^2}{2G_2(1+\nu_2)}$$

$$\frac{1}{E^*} = \frac{1-\nu_1}{2G_1} + \frac{1-\nu_2}{2G_2}$$

$$E^* = \frac{2G_1G_2}{(1-\nu_1)G_2 + (1-\nu_2)G_1}$$

Multiplying equation (I-5) in $E^*$ gives

$$\int_a^a \frac{p(s)}{x-s}ds = \frac{\pi}{2}q(x)[\frac{1-2\nu_1}{2G_1} - \frac{1-2\nu_2}{2G_2}]\times[\frac{2G_1G_2}{(1-\nu_1)G_2+(1-\nu_2)G_1}] - \frac{\pi}{2}E^*[u'_{z1}+u'_{z2}]$$

Or,

$$\int_a^a \frac{p(s)}{x-s}ds = \pi q(x)[\frac{1}{2}\frac{(1-2\nu_1)/G_1-(1-2\nu_2)/G_2}{(1-\nu_1)/G_1+(1-\nu_2)/G_2}] - \frac{\pi}{2}E^*[u'_{z1}+u'_{z2}] \quad \text{(I-6)}$$

Considering the expression in the bracket as $\beta$:

$$\beta = [\frac{1}{2}\frac{(1-2\nu_1)/G_1-(1-2\nu_2)/G_2}{(1-\nu_1)/G_1+(1-\nu_2)/G_2}] \quad \text{(I-7)}$$

Therefore,

$$\int_a^a \frac{p(s)ds}{x-s} - \pi\beta q(x) = -\frac{\pi}{2}E^*[u'_{z1}+u'_{z2}] \quad \text{(I-8)}$$

Using above-mentioned procedure and applying on the equation (2-8), we can obtain:

$$\int_a^a \frac{q(s)ds}{x-s} + \pi\beta p(x) = -\frac{\pi}{2}E^*[u'_{x1}-u'_{x2}] \quad \text{(I-9)}$$

Now we apply the boundary conditions equations (I-1) and (I-2) in the equation (I-8):

$$\int_a^a \frac{p(s)ds}{x-s} - \pi\mu\beta p(x) = \frac{\pi}{2}E^*(sign(x))\cot\alpha \quad \text{(I-10)}$$

or,

$$p(x)-\frac{1}{\pi\mu\beta}\int_{-a}^{a}\frac{p(s)ds}{x-s}=-\frac{E^*}{2\mu\beta}(sign(x))\cot\alpha \tag{I-11}$$

If we consider $X=x/a$ and $S=s/a$, then equation (I-11) can be written in a general form as follows:

$$F(X)+\frac{\lambda}{\pi}\int_{-1}^{1}\frac{F(S)dS}{X-S}=G(X) \tag{I-12}$$

where $F(X)$ and $G(X)$ are general functions.

Sohngen [84] has presented a solution for this equation. Considering the Sohngen solution, $p(X)$ is obtained as follows

$$\begin{aligned}p(X)=&-\sin^2(\pi\gamma)\frac{E^*(signX)\cot\alpha}{2\mu\beta}-\cos^2(\pi\gamma)\frac{E^*\cot\alpha}{2\pi(1-X^2)^{1/2}}\times\left(\frac{1+X}{1-X}\right)^{\gamma}\times\\&\times\int_{-1}^{1}(1-S^2)^{1/2}\left(\frac{1-S}{1+S}\right)^{\gamma}\frac{signS}{X-S}dS+\frac{P\cos(\pi\gamma)}{\pi a(1-X^2)^{1/2}}\times\left(\frac{1+X}{1-X}\right)^{\gamma}\end{aligned} \tag{I-13}$$

where $P$ is a constant, $\lambda=-1/\mu\beta$ and $\gamma$ is a constant related to $\lambda$ by $\cot g(\pi\gamma)=\lambda$. Figure (I-2) shows $p(X)$ distribution against $X$.

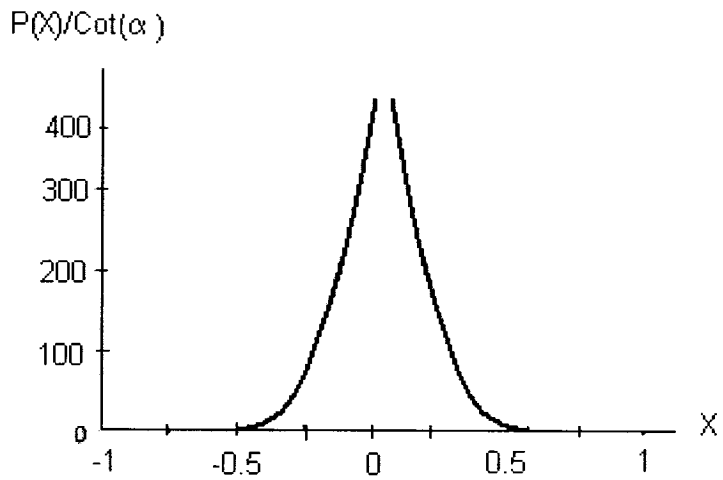


**Figure (AI-2).** Pressure distribution over the solid with friction [45].

# APPENDIX – II

# PIEZOELECTRIC EFFECT

When an external force is applied to a piezoelectric material, charges are generated on its surface, which is proportional to the applied mechanical stress. Conversely, an applied voltage generates deformation in the material. A Ferroelectric type of material is the one, which exhibits a spontaneous polarization in one or more direction of the crystal over a definite temperature range. Piezoelectricity must not be confused with the ferro electricity, which is the property of a spontaneous or induced electric dipole moment. All ferroelectric materials are piezoelectric, but the contrary is not always true. Piezoelectricity relates to the crystalline ionic structure.

A simplified model of piezoelectricity entails the motion of anions (-) and cations (+) moving in opposite directions under the influence of an electric field or mechanical force. The force generated by this motion causes lattice deformation for non-Centre symmetric crystals due to the presence of both high and low stiffness ionic bonds. As a result, all piezoelectric materials are anisotropic, in case of central symmetry; an applied force does not yield an electric polarization. The effect for quartz is shown below in figure (AII-1), positive and negative charges are formed. It is important to remember that the piezoelectricity is a function of the continuously changing mechanical deformation. Therefore, dynamic forces are used in practical situations.

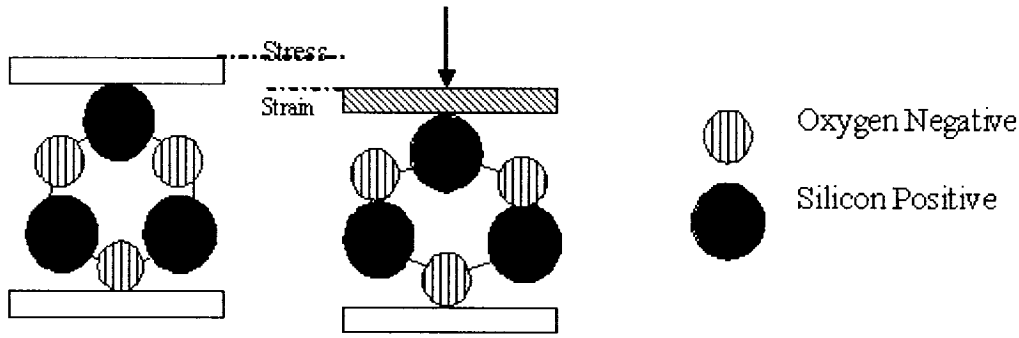


**Figure (AII-1).** Piezoelectric in ionic crystals such as quartz, ion position in quartz lattice with and without applied stress.

## AII.1 Piezoelectric Materials

The most extensively used natural piezoelectric materials are crystals (quartz and tourmaline). In synthetic piezoelectric materials, ceramics formed by many tightly compacted monocrystals (1μ in size) are most popular. These Ceramics, such as Lead Zirconate titanate (PZT), barium titanate are ferroelectrics. To align the dipoles to monocrystals in the same direction, they are subjected to strong electric field during their manufacturing process. The electric field is applied to the crystal above the Curie temperature to align the dipoles. Then the crystal is cooled while maintaining the field. This process makes crystal to be permanent electric polarized. When electric field is removed, the crystals cannot reorder in random form because of the accumulated mechanical stresses, resulting in permanent electric polarization. The problem with these materials are related to their temperature sensitivity and aging when approaching the curie temperature.

Polymers such as polyvinylidene fluoride (PVDF) also display piezoelectric properties and also have pyroelectric affects, i.e. change in temperature results in change in electrical charge. PVDF do not have central symmetry i.e. it displays piezoelectric properties. Compared to quartz and ceramics, piezo-film is more pliant and lighter in weight. In addition to this, it is rugged, inert and is low cost. Secondly urethane and epoxy adhesive are used for gluing PVDF film. The use of epoxy and urethane adhesives depends upon the strength requirement of the structure.

In smart structures, piezo ceramics are typically used as actuators and polymeric piezoelectric materials are typically as tactile sensors, temperature and stain sensors. It is common practice to embed piezoelectric sensors into prototypes because these sensors can be manufactured with strength and dimensional characteristics that do not degrade the structural integrity of the material from which the prototype device is made. Piezoelectric ultrasonic motors and piezoceramic sensors are currently being built into commercial products such as camera lens drives and automotive engine control systems. In many cases, thin layers of piezoceramic composites are bonded to other structural material surfaces. When thermal effects are generated through either friction or direct exposure to significant temperature gradients, the reliability of the electrode layer in these piezoceramics can completely dominate the performance of the device.

Basic constitutive equations are expressed in matrix notation as,

$$\varepsilon_{ij} = S_{ijkl}^{E,T}\,\sigma_{kl} + d_{kij}^{T}\,E_k + \alpha_{ij}^{E}\,\Delta T \qquad \text{(II-1)}$$

$$D_i = d_{ijk}^{T}\,\sigma_{jk} + k_{ij}^{\sigma,T}\,E_j + p_i^{\sigma}\,\Delta T \qquad \text{(II-2)}$$

in which,

$\varepsilon_{ij}$ : Second rank strain tensor

$S_{ijkl}$ : Forth rank elasticity tensor

$\sigma_{ij}$ : Second rank stress tensor

$d_{ijk}$ : Third rank piezoelectric coefficient tensor

$E_k$ : First rank electric field tensor

$a_{ij}$ : Second rank thermal coefficients tensor

$\Delta T$ : Zero rank temperature tensor

$D_i$ : First rank electrical displacement

$k_{ij}$ : Second rank permitivity tensor

$p_i$ : First rank pyroelectric coefficients tensor

Equation (II-1) shows the actuation state of a piezoelectric crystal and converse piezoelectric effect, while equation (II-2) expresses the sensory state of the crystal and direct piezoelectric effect. It is seen from the above equations, that each property being treated in isolation from the others and superposition therefore is applied. Superscripts show the independent variables are kept constants.

The piezoelectric coefficient tensor, which relates the first rank tensor $E_i$ to the second rank tensor $\varepsilon_{ij}$ in converse piezoelectricity or relates the second rank stress tensor $\sigma_{ij}$, to the first rank electrical displacement $D_i$ in direct piezoelectricity, is numerically the same for both equations.

The relation between electric field intensity $E$, the polarization $P$ and the electric displacement $D$ is in the form of: $D_i = \kappa_0 E_i + P_i$. Therefore $dP_i = dD_i - \kappa_0 dE_i$, and when the electric field is held constant, $dP_i = dD_i$.

When dealing with constant temperature environment and negligible electrical field, i.e. $\Delta T \approx 0$ and $E_i \approx 0$ equation (II-1) and (II-2) and be reduced to the following equations:

$$\varepsilon_{ij} = S_{ijkl}^{E,T} \sigma_{kl} \tag{II-3}$$

$$P_i = d_{ijk}^{T} \sigma_{jk} \tag{II-4}$$

Moreover, $d_{ijk}$ and $S_{ijkl}$, which are the third and forth rank tensors, consist of $3^3$ and $3^4$ number of items, respectively. However, due to symmetry property in both tensors, the number of independent items can be reduced significantly.

The second rank stress and strain tensors normally have 9 independent variables, which are reduced to 6 independent variables due to symmetry. Therefore, equation (II-3) and (II-4) can be re-written in the matrix notation as follows:

$$\varepsilon_k = S_{kj} \sigma_j \tag{II-5}$$

$$P_i = d_{ij} \sigma_j \qquad (i = 1,2,3 \ \ and \ \ k, j = 1,2,..,6) \tag{II-6}$$

Equation (II-6) can be expanded in the familiar form of matrix representation:

$$\begin{pmatrix} P_1 \\ P_2 \\ P_3 \end{pmatrix} = \begin{bmatrix} d_{11} & d_{12} & d_{13} & d_{14} & d_{15} & d_{16} \\ d_{21} & d_{22} & d_{23} & d_{24} & d_{25} & d_{26} \\ d_{31} & d_{32} & d_{33} & d_{34} & d_{35} & d_{36} \end{bmatrix} \begin{pmatrix} \sigma_1 \\ \sigma_2 \\ \sigma_3 \\ \sigma_4 \\ \sigma_5 \\ \sigma_6 \end{pmatrix} \tag{II-7}$$

The relations presented here are applicable to any piezoelectric crystals. However equation (II-7) is used when piezoelectric material acts as a sensor. This equation can be more simplified for the piezoelectric films, since the only practical direction to pick up the charge is direction 3, which introduces surface of the film as the electroded area. Piezoelectric coefficient matrix in equation (II-7) takes a number of formats for each

class of piezoelectric crystals based on their symmetry properties. For the PVDF, which is used in this study, only 5 parameters are non-zero.

### AII.2 Piezoelectric Coefficients

Most of piezoelectric coefficients have double subscript that links electrical and mechanical quantities. The first subscript gives the direction of the electrical field associated with voltage applied and second subscript gives the direction of the mechanical stress or strain.

#### AII.2.1 D – Coefficients

The piezoelectric constant related to the mechanical strain produced by an applied electric field are termed the strain constant or *d* coefficients or piezoelectric strain matrix. Conversely, the coefficient may be viewed as relating the charge collected on the electrodes, to the applied mechanical stress. The unit of *d* coefficient is C/N.

$d$ = charge density/applied mechanical stress.

#### AII.2.2 E – Coefficients

The piezoelectric constant related to the electrical field produced by applied mechanical stress at constant strain is known as e coefficient or piezoelectric stress matrix. The unit of e coefficient is $C/m^2$. There is relationship between *[e]* and *[d]* matrix and it is given as,

$$[e] = [d]\,[c] \qquad \text{(II-8)}$$

### AII.2.3 g-Coefficients

The piezoelectric constants relating the electric field produced by a mechanical stress are termed the voltage constants, or the g coefficients. The units are then expressed as volts/meter per Newton/square meter.

$$g = \frac{ElectricField}{Applied\ Mechanical\ Stress} \tag{II-9}$$

High $g_{ij}$ constants favor large voltage output, and are sought after for sensors. The relationship between the *[d]* and *[g]* matrix is given as

$$[d] = [K]^T[g] \tag{II-10}$$

### AII.2.4 Dielectric Constants

The relative dielectric constant is ratio of the permittivity of material, $\varepsilon$, to the permittivity of free space, $\varepsilon_0$, in the unconstrained condition. ($\varepsilon_0$= $8.9 \times 10^{-12}$ farad/meter).

$$K = \frac{Permittivity\ of\ materail}{Permittivity\ of\ free\ space} = \frac{\varepsilon}{\varepsilon_o} \tag{II-11}$$

### AII.2.5 Capacitance

Capacitance is a quantity dependent on the type of materials and its dimensions. Unit of capacitance is Farad. Capacitance is expressed by following formula

$$C = \frac{K\varepsilon_o A}{t} \tag{II-12}$$

where as 'A' area of electrodes, 't' is gap between the electrodes.

### AII.2.6 Young's Modulus

Young's Modulus is ratio of stress (force per unit area) to strain (change in length per unit length). Unit of young Modulus is $N/m^2$. For the PVDF films Young's Modulus varies between 1-3 *Gpa.*

### AII.2.7 Density

The ratio of the mass to volume in the material, expresses in $Kg/m^3$

### AII.2.8 Curie Temperature

The Temperature at which the crystal structure changes from a non-symmetrical (piezoelectric) to a symmetrical (non- Piezoelectric) form, expresses in degrees Celsius.

### AII.2.9 Pryoelectricity

Piezoelectric materials are also pryoelectric. They produce electric charge as they undergo a temperature change. When their temperature is increased, a voltage develops having the same orientation as polarization voltage. The change in electric field due to a temperature change is given as.

$$E_{pyro} = \frac{\alpha \Delta T}{K_3 \varepsilon_o} \qquad \text{(II-13)}$$

where as, E is the induced electrical field (volts/meter), α is the pyroelectric coefficient in Coulomb/$^0Cm^2$, ΔT is temperature difference in $^0C$.

# APPENDIX III

# ANALYSIS IN ANSYS

This section discusses details of modeling and analysis. In order to compare the results obtained above from the analytical symmetrical model, commercially available software can be used, such as, NASTRAN, FEM Lab and ANSYS. The finite element analysis software ANSYS was used in our work with which modal, static and transient analysis can be carried out. With the help of advanced software geometrics, different load sets and materials properties can be analyzed. The ANSYS software used in our research was version 10 and was used to construct a complete geometric model for the compliance and force sensor. This model was used to predict the force ratio, stresses developed at the different location of the sensor for a given load.

## AIII.1 Overview of ANSYS steps

When using ANSYS, all operations are performed using sequential steps. A flow chart, as shown in figure (III-1), is the basic approach to find a solution. We can use ANSYS in two different modes; either the programming mode or graphical mode but the latter is much easier to use.

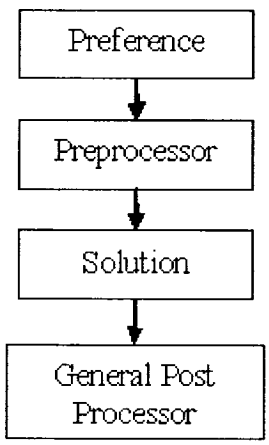


**Figure (AIII-1).** Overview of Ansys steps.

### AIII.2 Preference

The first step in ANSYS is to describe the nature of problem and to decide the method to be used for solving the problem which, in our case, is of a structural nature. Different modules are available for performing the analysis such as h or p methods. We used the h method for solving our problem.

### AIII.3 Preprocessor

This is the main body of modeling the problem and defining the element type, materials properties and real constant. In this section, we first defined the element type and its materials properties since the selection of the element is the main process in modeling. The modeling and meshing were performed in the next step. The main operation performed in the Preprocessor is given in the flowchart shown in figure (III-2).

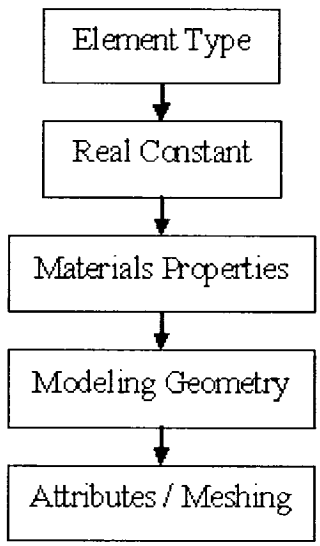


**Figure (AIII-2).** Flow chart of processes in the preprocessor.

### AIII.4 Solution

In this section, the ANSYS solution of modeled problem is carried out by using the flow chart shown in figure (III-3). The first required entry is to define the analysis types such as static, harmonic, dynamic. Apply loads require entry of boundary conditions that apply to our model. The last step is to solve the meshed model.

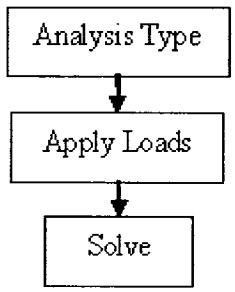


**Figure (AIII-3).** Steps for solving Ansys model.

### AIII.5 General Post Processor

In this section, data obtained as part of the solution section are reviewed using the many options available to see these results. Plot section and list section provide the results in the graphical presentation and numerical values, respectively. Any results such as stresses, strains, reactions at any point can be visualized using graphs.